INFRASOUND SIGNAL LIBRARY

Eric P. Chael[1] and Rodney W. Whitaker[2]

Sandia National Laboratories[1] and Los Alamos National Laboratory[2]

ABSTRACT

The International Monitoring System (IMS) proposed for verifying compliance with the Comprehensive Nuclear-Test-Ban Treaty will include an infrasound network for detecting and identifying explosions in the atmosphere. As is the case with seismic monitoring, data collected from historic events of interest are vital for improving infrasonic monitoring capabilities. Unfortunately, however, infrasonic recordings of such events are rare and thus any additional data sets that might be available should be pursued. Towards that end, we will digitize, as a result of the ROA01-38 award, paper records and extract from 9-track tapes several unique data sets from Sandia National Laboratories and Los Alamos National Laboratory that have not been available to the monitoring community. These data sets include recordings of surface and atmospheric explosions representing different yields, altitudes and weather conditions, as well as bolides and other natural phenomena that may be detected by the international infrasound monitoring network. Once the data are all in digital form, we will convert them to the standard CSS format, including event and station information. The complete set of database tables and binary waveform files will be the ultimate product of our work.

OBJECTIVES

Our objectives are to generate digital versions of relevant waveform data from older infrasound monitoring activities and distribute them to researchers and analysts, and to demonstrate a reasonably efficient digitizing system useful for retrieving additional data of similar type. In this joint Sandia National Laboratories (SNL) and Los Alamos National Laboratory (LANL) effort, we will make available in a common digital format four valuable sets of infrasound event recordings (including explosions and other types of events) which have hitherto been largely unavailable to explosion monitoring researchers. This collection of data can be exploited to address a number of issues for infrasonic monitoring by the IMS. Information on yield scaling, source functions, regional-distance propagation and variability due to weather could all be derived from such a collection.

RESEARCH ACCOMPLISHED

At the time of preparation of this paper for submission to the SRR Proceedings, neither Sandia nor Los Alamos had received any funds for this work. This proposal was accepted in the FY 2002 phase of the ROA01 process. The funding had been transferred to DOE in Albuquerque and was making its way to each lab. Thus we have not yet begun working on this project, and will report here on what we are planning to do. Candidate records for digitizing include those from atmospheric, surface and shallow underground nuclear tests at the Nevada Test Site, along with earthquakes, conventional ammonium nitrate and fuel oil explosions and bolide signals measured by the older operational infrasound network.

During atmospheric testing, Sandia personnel made numerous microbarograph recordings of the acoustic signals from nuclear tests at several stations surrounding the Nevada Test Site at approximately first bounce distances (Reed, 1969). These data exist only as paper strip-chart records and would make up the bulk of the Sandia contribution to the digital library. Other Sandia records include some acoustic data from underground tests (UGTs) and Plowshare events. These latter two sets were also taken with Sandia microbarographs. Sandia has tested a software package for digitizing these paper traces. This software comes from the well logging community and has the potential to handle most of the data in an efficient and accurate manner.

Los Alamos has been operating infrasound arrays in the southwest since 1983 on a continual basis. Acoustic signal data have been collected from UGTs, earthquakes and conventional explosion tests at White Sands Missile Range. Regrettably, most of the original digital data from the Los Alamos arrays were lost. Some tapes exist, and the first part of the Los Alamos work will be to search the tapes for events and send them to Sandia for reading. The second part would be to find paper records of selected events for digitizing with the Sandia software. Los Alamos has numerous paper records of atmospheric tests and bolides, recorded at various infrasound stations around the world from the 1950's to the 1970's.

CONCLUSIONS AND RECOMMENDATIONS

Based on our preliminary examinations of the early infrasound data available in the Sandia and Los Alamos archives, we believe the recordings are of good quality and offer a valuable resource to infrasound researchers. Under this project we will digitize a representative sample of the records, spanning a range of source sizes and altitudes. We will then distribute the resulting data sets within the monitoring community either on CDs or via the Web.

REFERENCE

Reed, J. W., 1969, Climatology of Airblast Propagations from Nevada Test Site Nuclear Airbursts, Sandia Laboratories Report SC-RR-69-572.

APPLICATION OF PHYSICS-BASED UNDERWATER ACOUSTIC SIGNAL AND ARRAY-PROCESSING TECHNIQUES TO INFRASOUND SOURCE LOCALIZATION

Gerald D'Spain, Michael Hedlin, John Orcutt, Bill Kuperman,
Catherine deGroot-Hedlin, Lewis Berger, and Galina Rovner

Scripps Institution of Oceanography, University of California, San Diego

ABSTRACT

The purpose of this project is to apply physics-based signal and array-processing techniques, recently developed in the area of underwater acoustics, to atmospheric infrasound data and co-located seismic field data. The infrasound data are collected by the eight microbarometers comprising the International Monitoring System (IMS) infrasound station at Pinon Flat (PFO) plus an additional five microbarometer/space filter sensor systems installed for a 6-week period at five Anza seismic station sites located within 40-km range of PFO. The co-located Anza seismic sensors as well as the Incorporated Research Institutes for Seismology (IRIS) seismic station at PFO provide the data needed to perform a comparison between infrasound and seismic recordings of atmospheric events across a very wide horizontal aperture. During the 6-week period, four rocket launches occurred at Vandenberg Air Force Base: an Atlas 2AS, a Taurus, a Titan 4B, and a Delta II. The arriving signals from three of these four launches were recorded with high signal-to-noise ratio. High-quality ground truth information on rocket trajectories and other quantities measured during two of the launches have been acquired from the Vandenberg and Los Angeles Air Force Bases.

OBJECTIVE

The purpose of this project is to apply physics-based signal and array processing techniques, recently developed in the area of underwater acoustics, to atmospheric infrasound data and co-located seismic station field data. The hypothesis to be tested is that advanced underwater acoustic signal and array-processing techniques, with some modifications, can provide more accurate source locations and source signature estimates of low-level events of interest in nuclear explosion and treaty monitoring than conventional methods. In addition, the joint use of infrasonic and seismic data from co-located sensor systems has the potential to significantly increase phase identification and source localization capability, and reduce unwanted background noise.

Basic research questions we are addressing in this project include:

- What are the effects of range-dependent, heterogeneous, and time-variable media on infrasound propagation and source localization?

- How can the location of caustics in infrasound be exploited for source localization? Can the location of these caustics be predicted accurately with available environmental data?

- Can waveguide invariant techniques, which have proven to provide robust and simple approaches to analyses of underwater waveguide propagation, be used effectively with infrasound data?

- What are the important sources of infrasonic noise and signals in the southern California environment? How will these measurements be translated into other areas of the world?

- What acoustic propagation codes (e.g., ones based on a parabolic equation (PE) solution to the acoustic wave equation which includes the effect of winds) incorporate the important propagation physics and so can be used for effective forward modeling in the inverse problems of localizing sources and inferring atmospheric properties?

- A question related to the inverse problem is how effective are sources of opportunity, e.g., mining and quarry blasts, bolides and rocket launches, in calibrating the atmospheric propagation characteristics?

- What are the spatial correlation lengths of various infrasound signals and noise at frequencies of interest scientifically and operationally? How do these correlation lengths vary with topography, weather, humidity, background noise, and other environmental variables?

- How can seismic and acoustic data be used in parallel to understand infrasonic wave excitation and propagation and to localize the source? In particular, how do seismic and acoustic waves couple at the interface between the earth and atmosphere and can this coupling be used to both identify the many wave types observed and infer source location?

The primary goal of this paper is to use high-fidelity numerical modeling methods along with the launch trajectory information and environmental data collected at the time of the launches to determine the predictability of the arrival structure of the signals across the PFO/ANZA array from these 400-km-distant rocket launches. The predictions take into account the signal-distorting effects caused by phase delays across the spatial aperture of the space filters (i.e., each microbarometer/space filter system is not omni-directional over the frequency band of interest). A second goal is to search for any possible phase coherence between the output of a microbarometer and a co-located sonic anemometer.

RESEARCH ACCOMPLISHED

Focused Experiment

A focused infrasound experiment was conducted over the 6-week period from 7 September to 18 October 2001. The 8-element International Monitoring System (IMS) infrasound station (I57US) at the Pinon Flat Observatory (PFO), in the high desert 125 km northeast of San Diego, was the source of much of the data. In addition, data were collected from the co-located, three-component, broadband IRIS (Integrated Research Institutions for Seismology)

seismic station at PFO (an IMS auxiliary seismic station) to permit studies of the relationship between the atmospheric infrasound and seismic wave fields. Fig. 1 shows a map of the 8 I57US microbarometer sensors (H1 thru H4 and L1 thru L4), and the IRIS station, along with a line indicating the back azimuth to Vandenberg Air Force Base. The H-type microbarometers, spaced 100 to 200 m apart, had 18-m rosette space filters attached and the L-type sensors, forming a centered triangle with nominal 1.4-km-long sides, had 70-m diameter space filters. The space filters cause each of the infrasound sensors to become a directional receiver with frequency-dependent characteristics; this issue will be discussed further below.

As part of the focused experiment, a microbarometer/space filter sensor system was installed at each of five Anza seismic station sites located within 40-km range of PFO. The space filters at these stations were composed of 4 porous tubes of 15-m length each, arranged in a "plus" (+) pattern as symmetrically as the layout of each site allowed. Fig. 2 is a map of the topography along with the locations of the 5 Anza stations (RDM, KNW, CRY, WMC, and SND) and PFO. A line indicating the back azimuth to Vandenberg Air Force Base again is included in the figure.

Data from the Titan 4B Launch

During the 6-week focused experiment, four rocket launches were conducted at Vandenberg Air Force Base, 400 km to the west-northwest of PFO. The rockets were an Atlas 2AS, a Taurus, a Titan 4B, and a Delta II. Fig. 3 shows a 10-min time series of the arrivals from the Titan 4B as recorded by all 13 infrasound sensors. The data were band-filtered between 1 and 3 Hz. Time 0 on the plot corresponds to 21:40:00 GMT, 5 October, 2001 (JD 278), which is 19 min after the announced launch time. Assuming that the first arrival was created when the rocket first reached supersonic speed, then it has a group velocity of approximately 300 m/s. The waveforms at each of the stations are dominated by three major arrivals, occurring at 22.5 min, 24 min, and 25.4 min after launch in the uppermost traces. Numerical modeling results discussed below indicate that the first arrival is the stratospheric refracted arrival, the first part of the second arrival is also the stratospheric refracted arrival when the rocket reaches the upper regions of the stratosphere whereas the second part is the refracted arrival from the lower part of the thermosphere, and the third arrival initially reflects from the ground and then refracts from higher altitudes in the thermosphere. Therefore, the spread in arrival structure is associated both with the motion of the rocket through the atmosphere and the propagation characteristics through the stratospheric waveguide.

Variations in arrival structure across the 40-km aperture of the array are clearly visible. In addition, the arrival structure recorded by the sensors with 18-m space filters (the uppermost 4 "I57H" traces) is different than that recorded by the sensors with 70-m filters (the "I57L" traces). The corresponding spectrogram of the time series recorded by the temporary infrasound station at Anza station Red Mountain (IRDM) is presented in Fig. 4. The arrivals from the rocket launch have energy that extends up to 5 Hz. However, this higher frequency energy is strongly attenuated by the 70-m space filters, as discussed below.

White-noise-constrained adaptive plane-wave beam forming (Gramann, 1992; Cox, Zeskind, and Owen, 1987) has been applied to the Titan 4B arrivals. Fig. 5 shows the results of the processing on the second part of the second, main arrival (just after the 5-min mark in the upper traces in Fig. 4) using just the data collected by the 8 I57US sensors. The analysis was done only up to 2.5 Hz to avoid the higher frequencies where the 18-m and 70-m space filters have significantly different response characteristics. The white-noise-constraint value used for the results in the figure is 2.5 dB down from 10*log(N) where N is the number of array elements. (Using a constraint value of 10*log(N) is equivalent to conventional array processing). The two-dimensional (2-)D array frequency/wave number processing output is a function of frequency, time, wave number (or slowness), and azimuth. Fig. 5 presents a plot of frequency vs. wave number at a fixed azimuth of 285 deg, the back azimuth having greatest energy for the second arrival. The slope of the dark ridge of energy in the plot passing through the origin equates to a phase velocity of around 359 m/s. A similar plot for the first arrival indicates a phase velocity of 350 m/s. Both estimates are accurate to within about 5 m/s, so the difference in the two results appears to be significant. This phase velocity difference is consistent with the numerical modeling results where the stratospheric refracted arrival has an apparent phase velocity of around 345 m/s (it depends somewhat upon the altitude of the rocket) and the lower thermospheric refracted signal arrives with nearly a 355 m/s phase velocity.

In addition to searching for differences in the arriving phase velocities of the major arrivals in the time series in Fig. 3, several additional adaptive beam forming calculations were done to look for possible differences in azimuth of arrival. The trajectory of the rocket took it to the southwest from the launch site, so that an evolution in azimuth

might be evident in the data. The results showed that all arrivals had back azimuths within 1 or 2 deg of 285 deg. The second part of the second arrival in Fig. 3, i.e., the energy just after the 5-min mark in the upper traces, may have arrived a degree or two from a more southerly direction than the first part just prior to the 5-min mark, but this difference probably is within the beam former resolution.

Numerical Modeling using CASS/GRAB

The Comprehensive Acoustic System Simulation (CASS) program (Weinberg *et al*, 2001; Weinberg and Keenan, 1996) is being used to perform the numerical modeling. The CASS program, developed at the Naval Undersea Warfare Center, Division Newport, is a US Navy-standard code that has been approved by the Navy's Oceanographic and Atmospheric Master Library (OAML). To obtain OAML accreditation, the code underwent extensive testing and has been thoroughly documented. CASS actually is a modular collection of codes that allow all aspects of sonar system performance to be modeled. One of the acoustic propagation models in CASS is the Gaussian Ray Bundle (GRAB) model (Weinberg and Keenan, 1996), which was used in this work. Gaussian ray bundles and Gaussian beam tracing represent recent advances in ray theoretically based modeling, which provides more accurate wave field amplitude results (Jensen *et al*, 1994; see also Cerveny *et al*, 1982). GRAB allows for range dependence of the sound speed profiles and range dependence in the bottom interface (which is either the ocean bottom in hydroacoustic modeling or the Earth topography in atmospheric infrasound), so that propagation in a 3-D varying medium is done using an N X 2-D approximation.

In addition to its more advanced amplitude modeling capability and extensive testing and documentation, the advantages of using CASS/GRAB are that it includes several options for modeling a variety of physical phenomena, the source code is included with the distribution, and it can easily be run in batch mode. Although CASS/GRAB was developed for the underwater sonar problem, the only significant adaptation required for modeling infrasound propagation in the atmosphere was to place an artificial, flat, pressure release upper boundary at 150-km altitude (i.e., zero "depth"). The program is run to search for eigenrays in the ± 60 deg about horizontal launch angle interval, but no rays are allowed in the solution that interact with the artificial interface at 150 km.

Information on the position of the rocket as a function of time at 1-sec intervals after launch was provided by the personnel at Los Angeles Air Force Base, with valuable assistance from individuals at Vandenberg Air Force Base. According to the trajectory information, the rocket became supersonic 8 sec after launch at an altitude of about 300 m. The numerical modeling starts at this position (see McLaughlin *et al*, 2000) and continues for the 242 sec it takes for the rocket to exceed 150 km in altitude. The results presented here are limited to the 8- to 200-sec interval after launch.

The sound speed profile information used as input to the propagation modeling was derived from data from two sources. First, Douglas Drob at the Naval Research Laboratory provided us with profiles of temperature and the meridional and zonal wind profiles at 1-km increments up to 170-km altitude and at approximately 10-km-spaced points along two great circle paths, from PFO to the rocket launch point and from PFO to the splash down point of one of the jettisoned components. Profiles were provided for two different time periods, 1800 GMT and 2400 GMT, 5 Oct, which bracket the launch time. The modeling presented here uses only the profiles along the great circle path from PFO to the launch position, and only from the 2400 GMT, 5 Oct time period. The second source of sound speed information came from the empirical atmospheric models (the Horizontal Wind Model and the Extended Mass Spectrometer - Incoherent Scatter Radar temperature model) contained in the Infrasonic Modeling of Atmospheric Propagation (InfraMAP) tool kit (Norris *et al*, 1999).

Range-dependent modeling, both range dependence of the sound speed profiles and of the topography over land, has been performed. However, only the range dependence of the topography has been incorporated in the modeling results presented here. Effective range-independent sound speed profiles were obtained by first averaging the temperature, meridional, and zonal wind profiles along the great circle path separately. Then, an effective profile was derived by adding the projection of the horizontal wind vectors along the great circle path to the sound speed profile based on the temperature data alone. The left panel in Fig. 6 shows a comparison of the effective range-averaged sound speed profiles from the Drob data (solid curve) and from InfraMAP (dashed curve). The Drob-derived profile has more structure in the stratospheric waveguide (0-50 km altitude), almost forming two ducts, than the InfraMAP profile. This structure has a strong effect on the predicted signal arrival structure, as discussed below. The right hand panel shows the attenuation profile for a frequency of 1 Hz used in the modeling. This profile was extracted from the InfraMAP output (0 - 120 km) and then extrapolated to 150 km.

A fundamental property of propagation in a waveguide is its dispersive characteristics. By providing a measure of the relationship between the group and phase velocities of the various multi-path components in a wavefield, the waveguide invariant quantifies in a single scalar parameter these dispersive characteristics (e.g., D'Spain *et al*, 2000; D'Spain and Kuperman, 1999). Plots of the invariant ("inverse beta") for the two range-averaged sound speed profiles in Fig. 6 are presented in Fig. 7. Again, the solid curve pertains to the profile obtained from the Doug Drob data and the dotted curve is for the InfraMAP-derived profile. The horizontal line at the invariant value of zero indicates where no dispersion occurs (i.e., a broadband pulse remains a pulse) whereas increasingly larger positive and negative values signify increasing amounts of dispersive spreading (and pulse distortion). Two transitions appear in the curves: between 5.5 and 6 deg and between 13.0 and 13.5 deg in the solid curve. The first transition occurs when the ray angles become sufficiently steep that the lower boundary of the waveguide no longer is created by refraction, but by reflection from the ground. (The receiver altitude is taken to be the 1280-m altitude of PFO). The second transition between 13.0 and 13.5 deg is more relevant to the rocket launch data and occurs when the ray angles become sufficiently great that the energy is no longer trapped in the stratospheric waveguide. The important difference between the solid and dotted curves occurs just prior to this transition. That is, the solid curve shows an asymptotic approach to the horizontal line at zero, whereas the InfraMAP curve crosses over it. The implication of this asymptotic approach is that the dispersion is very small over a fairly wide interval of ray angles, so that focusing of broadband pulse energy will occur (Kuperman *et al*, 2001).

The CASS/GRAB 1-Hz modeling results of the eigenray amplitudes as a function of time after rocket launch for the two sound speed profiles in Fig. 6 are shown in Figs. 8 and 9. The predicted arrival structure for the two cases is remarkably different. Whereas the InfraMAP profile (Fig. 9) yields only two major arrivals with the first arrival being the largest in amplitude and having a duration longer than 2 min, the Drob-derived profile (Fig. 8) predicts a small amplitude first arrival followed by a 1-min gap and then a large-amplitude second arrival. This large-amplitude arrival is the result of the broadband focusing evident from the waveguide invariant plots in Fig. 7(as discussed in the previous paragraph). Both sound speed profiles indicate a short duration arrival at the 25-min mark surrounded by low-level "coda". They also both predict that a gap occurs around the 24 min mark, although it is significantly shorter for the Drob-derived profile than for the InfraMAP profile. A comparison with Fig. 3 shows that the Drob-derived profile results provide a much better match to the main features in the actual measurements. That is, they reproduce the relative amplitudes of the first and second arrivals, the 1-min gap between the first and second arrivals, the short duration nature of the gap at the 24-min mark, and the fact that three or four arrivals are present.

To better identify the components of the arrival structure in the Drob-derived predictions, and in the actual data, the eigenray arrivals are plotted as a function of both time after launch and rocket altitude. (Note that the time scale is from 20 to 34 min after launch rather than 19 to 29 min as in Figs. 8, 9, and 3). This plot represents a rocket trajectory travel-time curve. Two different sizes of dots are used to provide an indication of eigenray amplitude. (Fig. 8 is the result of integrating along each vertical line in Fig. 10). Three different branches are evident in the figure. The first, starting at the 21-min mark, is the stratospheric refracted path, the second is the lower thermospheric refracted arrival, and the third, which bifurcates from the second as the rocket altitude increases, is the path that reflects first from the ground and then refracts from higher altitudes in the thermosphere.

Therefore, the first arrival in Figs. 3 and 8 is the stratospheric refracted path that exists when the rocket is at low altitudes. This path disappears as the rocket passes through the upper troposphere and lower stratosphere because of the small medium sound speeds at these altitudes, leading to the 1-min gap between first and second arrivals. The first part of the second arrival actually is the reappearance of this path as the rocket ascends into the upper stratosphere where medium sound speeds are greater. The received amplitudes at PFO are largest from this portion of the rocket trajectory. The short gap around the 24-min mark is the time separation between the latest arriving stratospheric refracted path energy and the lower thermospheric refracted energy. That is, the arrivals just on either side of the 5-min mark in Fig. 3 represent these two different phases. The trailing energy arriving last has reflected from the ground before refracting in the thermosphere.

Plane Wave Response of Space Filters

Each inlet port of the space filters acts as an omni-directional point receiver. The outputs from each of these receivers are summed together at the microbarometer without any relative phase delay since the distance from each port to the microbarometer is the same. This summation is equivalent to forming a broadband beam in the vertical

direction whose character is determined by the 2D spatial distribution of the ports. (In some deployments, the 3D distribution should be taken into account). The plane wave response of the directional receiver characteristics of a 70-m space filter as a function of frequency and elevation angle are shown in Fig. 11. The incoming plane wave is assumed to have unity amplitude so that its mean squared amplitude is 0.5 (-3 dB). Because of the relative phase delays due to propagation across the horizontal aperture of the space filter, the signal amplitude becomes increasingly attenuated with increasing frequency above 1 Hz at the smaller elevation angles. Complete destructive interference occurs along an arc in the frequency/elevation angle plane starting at 5 Hz and 0 deg elevation angle (horizontal). Similar plots show little variation as a function of azimuth so that the response is effectively isotropic in the horizontal plane. Also, no shift in signal phase occurs due to the space filter response so that only its effects on amplitude need to be taken into account. All of the various issues associated with the distorting effects of the rosette space filters are discussed in Hedlin *et al*, 2002.

(No) Phase Coherence Between Wind Velocity and Infrasonic Wind Noise

A focused experiment was conducted at PFO to examine the coherence between the time series from an MB 2000 microbarometer without a space filter and the three components of wind velocity as measured by a co-located sonic anemometer. The goal was to investigate the possibility of using adaptive noise cancellation processing (Widrow, 1976) to remove wind noise contamination in the microbarometer time series. These types of processing schemes allow the phase correlated component (as measured by coherence) between two time series to be separated from the uncorrelated component. Therefore, if sufficient coherence exists between the anemometer and microbarometer time series, then an anemometer could replace a space filter, thus minimizing land use and saving deployment costs.

A total of 166 hours (nearly 7 days) of continuous data were recorded from 4-11 Mar (JD 063-070) 2002. An MB 2000 was placed at a height of 2 m above ground and adjacent to a sonic anemometer at the same height. All six channels of data - two from the microbarometer and four from the sonic anemometer - were digitized at a 20 samples/sec rate and recorded on the same data acquisition system. Fig. 12 shows a plot of 20 min of time series from the two output channels from the MB 2000 (lower-most two panels with the second-from-bottom trace being the output high-pass filtered above 0.05 Hz) and the four channels of output from the sonic anemometer (upper four panels). Although some similar features can be seen in the time series for the three components of wind velocity (upper-most three traces) and the microbarometer infrasound output (second-from-bottom trace), no statistically significant coherence between the infrasound time series and any wind velocity component time series was found at any frequency at any time over the full 166 hours of the experiment.

CONCLUSIONS AND RECOMMENDATIONS

Infrasound signals with large signal-to-noise ratio were recorded by 13 sensors, including the 8 I57US elements at PFO, during a Titan 4B rocket launch at Vandenberg Air Force Base, 400 km distant. Numerical modeling was performed with the CASS/GRAB program, a US Navy standard Gaussian ray bundle-based code, with rocket trajectory information from Los Angeles Air Force Base. The results using profiles of temperature and horizontal winds provided by Douglas Drob at the Naval Research Laboratory show good agreement with the main features of the measured arrival structure. The first arrival is a stratospheric refracted return when the rocket is at low altitudes, followed by a 1-min gap as the rocket passes through the upper troposphere and lower stratosphere where the medium sound speeds are too small to support this path. However, once the rocket ascends into the upper stratosphere where the sound speeds are greater, this path reappears. Its reappearance is marked by large received amplitudes due to broadband focusing, as predicted by waveguide invariant techniques. A short gap in time follows, terminated by the arrival of lower thermospheric-refracted energy. These arrivals have detectable amplitudes also because of broadband focusing. The signals arriving last traveled paths that reflected from the ground before refracting in the thermosphere at higher altitudes. All these components of the arrival structure are clearly illustrated by a rocket trajectory travel-time curve. White-noise-constrained adaptive beam forming on the first arrival and on the thermospheric-refracted arrival yield phase velocity estimates that differ by 10 m/s, consistent with the difference expected from the numerical modeling results.

The 2-D spatial distribution of the individual ports of the space filters acts like a beam former to point a beam in the vertical direction. Therefore, each microbarometer is converted into a directional receiver. The signal-attenuating effects of this vertical beam must be taken into account at frequencies above 1 Hz for the 70-m filters.

Finally, no statistically significant coherence was found between the infrasound time series from an MB 2000 microbarometer and the three wind velocity components as measured by a co-located sonic anemometer.

REFERENCES

Cerveny, V., M. M. Popov, and I. Psencik (1982), Computation of Wave Fields in Inhomogeneous Media - Gaussian Beam Approach, Geophys. *J. R. Astr. Soc.*, **70**, 109-128.

Cox, H., R. M. Zeskind, and M. M. Owen (1987), Robust Adaptive Beamforming, IEEE Transactions of Acoustics, Speech and Signal Processing ASSP-35 (10).

D'Spain, G. L., W. A. Kuperman, J. A. Orcutt, and M. A. H. Hedlin (2000), Long-Range Localization of Impulsive Sources in the Atmosphere and Ocean from Focus Regions in Single Element Spectrograms, Proc. of 22nd Annual Seismic Research Symposium: Technol. for Monitoring the Comprehensive Nuclear-Test-Ban Treaty, 8 pgs.

D'Spain, G. L. and W. A. Kuperman (1999), Application of Waveguide Invariants to Analysis of Spectrograms from Shallow Water Environments that Vary in Range and Azimuth*, J. Acoust. Soc. Am.*, **106** (5), 2454-2468.

Gramann, R. A. (1992), ABF Algorithms Implemented at ARL-UT, ARL Tech. Letter ARL-TL-EV-92-31, Applied Research Laboratories, The University of Texas at Austin, Austin, TX.

Hedlin, M. A. H., B. Alcovarro, and G. L. D'Spain (2002), Evaluation of Rosette Infrasonic Noise-Reducing Spatial Filters, submitted to *J. Acoust. Soc. Am.*, 28 pgs.

Jensen, F. B., W. A. Kuperman, M. B. Porter, and H. Schmidt (1994), *Computational Ocean Acoustics*. American Inst. Physics, New York, 168-170.

Kuperman, W. A., G. L. D'Spain, and K. D. Heaney (2001), Long Range Source Localization from Single Hydrophone Spectrograms, *J. Acoust. Soc. Am.*,**109** (5) pt. 1, 1935-1943.

McLaughlin, K. L., A. Gault, and D. J. Brown (2000), Infrasound Detection of Rocket Launches, Proc. of 22nd Annual Seismic Research Symposium: Technol. for Monitoring the Comprehensive Nuclear-Test-Ban Treaty, 219-230.

Norris, D., R. Nadel, and R. Gibson (1999), User's Guide for InfraMAP, v. 1.4, BBN Tech. Memo. W1353a, BBN Technologies, Arlington, VA.

Weinberg, H., R. L. Deavenport, E. H. McCarthy, and C. M. Anderson (2001), Comprehensive Acoustic System Simulator (CASS) Reference Guide, NUWC-NPT TM 01-016, Naval Undersea Warfare Center Division Newport, RI.

Weinberg, H. and R. E. Keenan (1996), Gaussian Ray Bundles for Modeling High-Frequency Propagation Loss under Shallow-Water Conditions, *J. Acoust. Soc. Am.*, **100** (3), 1421-1431.

Widrow, B., J. M. McCool, M. G. Larimore, and C. R. Johnson (1976), Stationary and Nonstationary Learning Characteristics of the LMS Adaptive Filter, *Proc. IEEE*, **64** (8), 1151-1162.
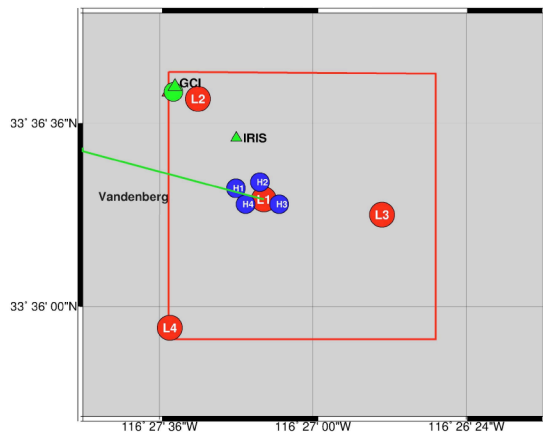
Figure 1. Map of the I57US infrasound station at Pinon Flat Observatory (PFO).
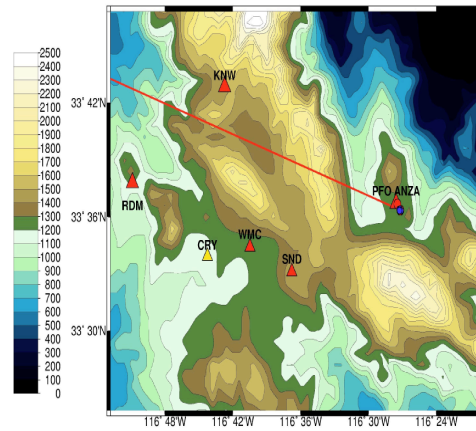

Figure 2. Map of PFO and the five ANZA stations where infrasound sensors were temporary installed for the focused experiment, along with the surrounding topography
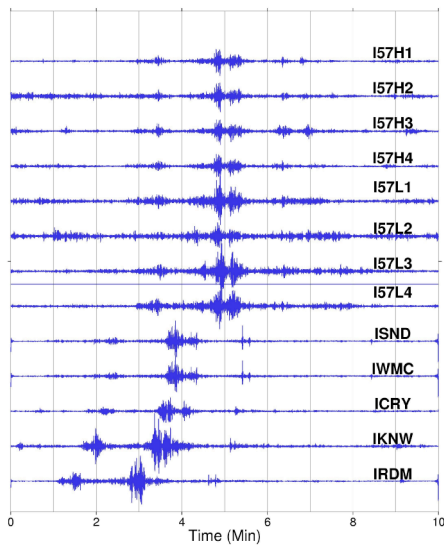

Figure 3. Time series of arrivals from the Titan 4B launch recorded by all 13 infrasound sensors, band-pass filtered from 1 to 3 Hz.
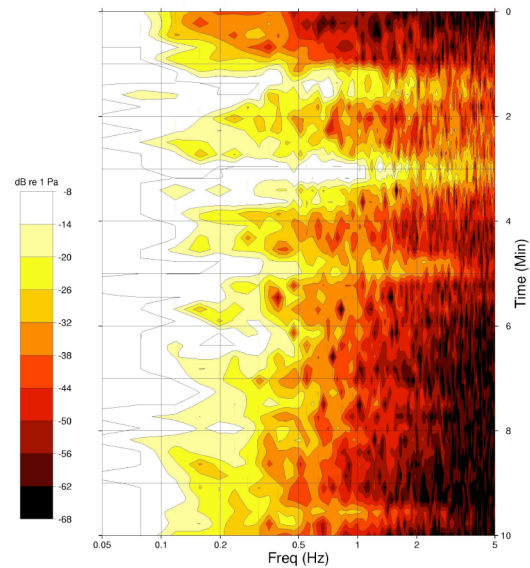

Figure 4. Spectrogram of data recorded by station IRDM over the same 10-min period as Fig. 3 (lower-most trace).
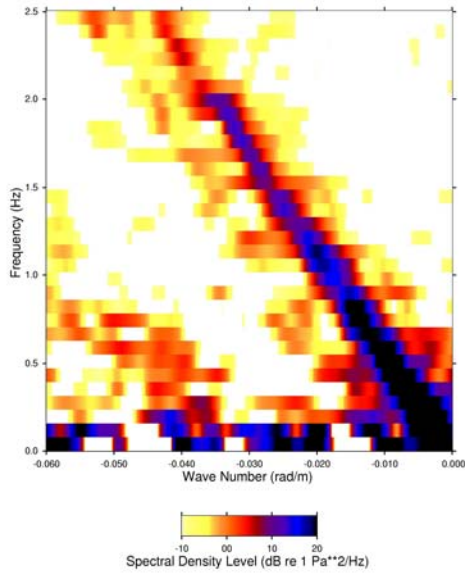
Figure 5. White-noise-constrained adaptive beam forming on the 2nd part of the 2nd (main) arrival from the Titan 4B launch at 285 deg back azimuth.
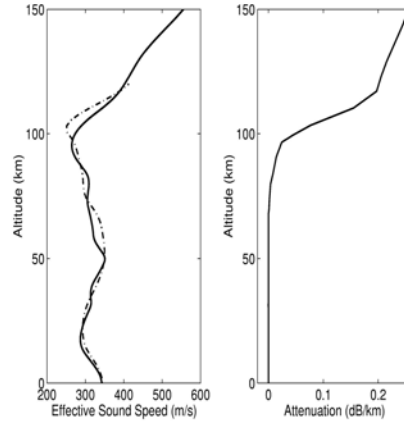

Figure 6. Effective range-averaged sound speed profiles (left panel) derived from NRL data (solid curve) and from InfraMAP databases (dashed curve), and the attenuation profile at 1 Hz (right panel) used in the modeling.
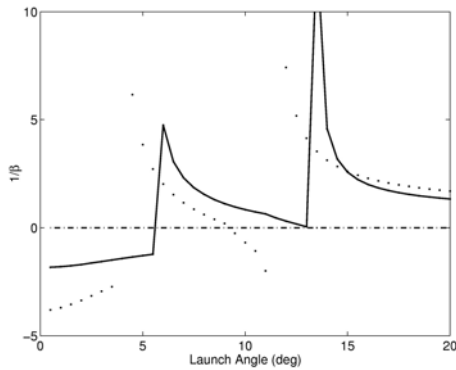

Figure 7. The waveguide invariant as a function of arrival angle for the two sound speed profiles in Fig. 6 and for an altitude corresponding to I57US.
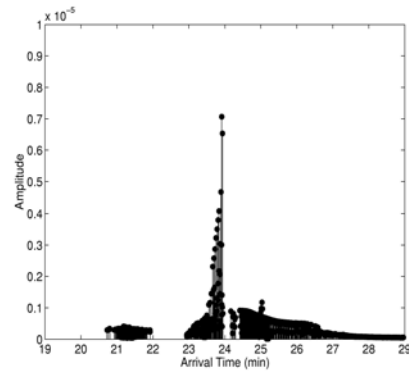

Figure 8. The amplitude vs. arrival time at PFO of the CASS/GRAB eigenrays created in the 8- to 200-sec time interval by the Titan 4B rocket modeled as a moving point source for the NRL-data-derived sound speed profile (solid curve in Fig. 6).
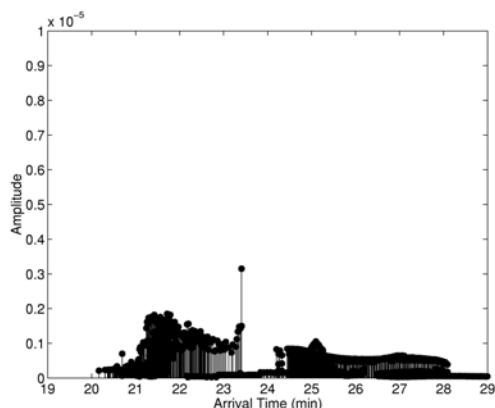
Figure 9. CASS/GRAB-modeled eigenray amplitude vs. arrival time at PFO for the InfraMAP-derived sound speed profile (dashed curve in Fig. 6).
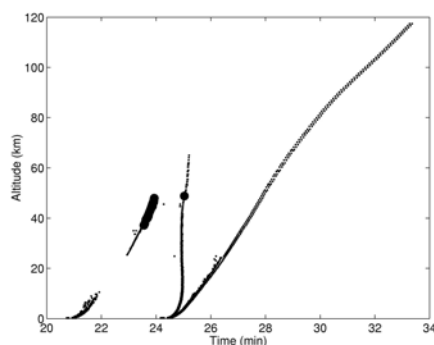

Figure 10. The CASS/GRAB-modeled eigenray arrival times at PFO as a function of rocket altitude. The large and small circles signify eigenray amplitudes greater or less than 1.0 x 10-6, respectively.
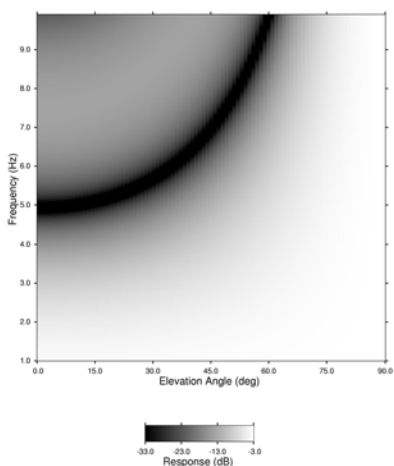

Figure 11. Plane wave response of the 70-m rosette space filters as a function of frequency and elevation angle of arrival.
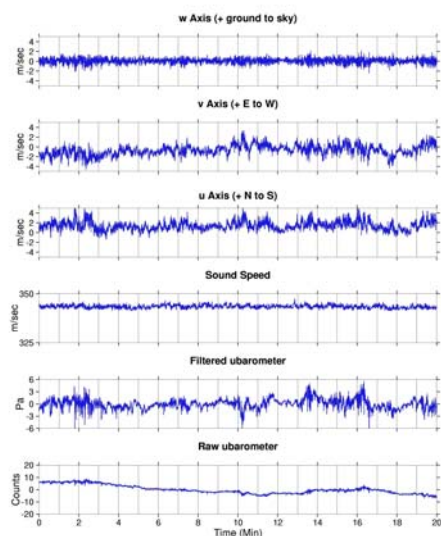

Figure 12. 20-min time series of the 4 output channels of a sonic anemometer (3 components of wind velocity, and sound speed, respectively) and the 2 channels of a co-located microbarometer.

EVALUATION OF INFRASONIC DETECTION ALGORITHMS

Milton A. Garcés and Claus H. Hetzer

University of Hawaii, Manoa

<u>ABSTRACT</u>

Infrasound array IS59, Hawaii, also known as the KONA array, started operations on May 25, 2000, and was certified into the International Monitoring System in December of 2001. In order to interpret the KONA data, various analysis tools have been acquired, developed, and evaluated at the Infrasound Laboratory (ISLA) of the University of Hawaii. These include modified versions of Sandia National Laboratories' MatSeis, Los Alamos National Laboratory's InfraTool, STA/LTA-based automatic detectors, and the Progressive Multi-Channel Correlation (PMCC) method. Evaluation of various detection algorithms during routine analysis of the KONA array data demonstrated that PMCC was not as vulnerable to spatial aliasing as frequency-domain detection methods, and it allowed detection of signals below the noise level, which is not possible with a STA/LTA detector. PMCC is presently used to produce automatic bulletins of signals detected by KONA. Phase names based on source identification have been devised to aid in classification. Detector results are subjected to a minimum-correlation/minimum-family-size filter, and both filtered and unfiltered bulletins are produced. The bulletins, which are not subjected to analyst review, provide Phase, Date and Time UT, Azimuth, Slowness, Correlation, Median Frequency of Detection, RMS Amplitude, and Family Size. Filtered detector results are written to CSS .arrival tables, which are subject to analyst review. Future work should concentrate on the development of an automatic, intelligent event identification algorithm that can screen the large amount of events picked by automatic detectors.

OBJECTIVE

The aim of this paper is to discuss the infrasonic signal detection algorithms that have been tested at the Infrasound Laboratory (ISLA), which operates the KONA array. The detection parameters for the signals that are routinely recorded will also be discussed.

RESEARCH ACCOMPLISHED

Summary of Analysis Techniques

In the first two years of the project, a suite of array-processing algorithms was evaluated. Initially, a combination of STA/LTA, F-K, and correlation analyses was used to obtain the arrival azimuth and trace velocity of high-frequency signals. Long-duration, emergent arrivals were detected using the Los Alamos National Laboratory's (LANL) InfraTool. Automatic detections were performed with these algorithms, and the methods and types of signals observed by the KONA array were presented in Garcés and Hetzer (2001). In December 2001, evaluation of the Progressive Multi-Channel Correlation (PMCC) detector (Cansi, 1995) was initiated. The PMCC detector has been automated and is the primary detection system presently implemented at the ISLA.

Description of the PMCC detector

PMCC is a time-domain detector that uses the correlation between various groupings of three sensors, i,j,k, to obtain an estimate of the consistency of the closure relation

$$r_{ijk} = \Delta t_{ij} + \Delta t_{jk} + \Delta t_{ki} , \qquad (1)$$

where Δt_{ij} is the time delay between the arrival of a signal at sensors i and j (Cansi and Klinger, 1997). If the consistency is below a certain threshold, a detection is registered. This detector has performed well in KONA for signal-to-noise ratios (S/N) that are close to unity and for all signal frequencies.

The PMCC algorithm is based on analysis of overlapping windows of data. The cross-correlation function of the data from two stations determines a time delay Δt_{ij}; and the mean quadratic residual of the closure relations (Eq. 1) of the sub array triplets yields the consistency of the signal. A subset or all of the array elements can be used for an initial time-delay calculation, which yields an initial value of arrival azimuth and slowness. Using these values, the consistency for additional elements can be progressively calculated. These additional array elements are directed into the calculation by examining a shorter section of the time window determined by a specified bearing and slowness range. If the point of maximum correlation requires a significant variance in azimuth, velocity, or time, the arrival is discarded. This optimizes computation time over a large array, and also allows initial false alarms caused by the presence of correlated noise in the first array subset to be eliminated when not present in further subsets (Cansi, 1995).

During the PMCC calculation, each time window is filtered into a number of frequency segments using a specified suite of filters, and the results are analyzed individually for similarity in azimuth, slowness, and consistency. A detection must satisfy specified trace velocity limits, arrival azimuth variation limits and duration limits, and must appear on a specified minimum number of stations. Each frequency band within each time window represents a "pixel" of data (Figure 1a) and each pixel is analyzed independently. Pixels adjacent in time and/or frequency are compared, and nearest-neighbor groups of pixels with similar characteristics are classified as "families" (Figure 1b). Families that conform to a specified range of sizes are placed in a table of detections.

In order to run the algorithm in near real time, a simple script must be used to generate an initialization file that contains all of the parameters necessary to determine the detection thresholds, as well as the names of and paths to the data files. This initialization file can then be passed to the PMCC executable file, which processes the waveform data and generates a file containing the aforementioned table of families. Each variation in the detection parameters requires a separate run of the detector with a unique initialization file.

For the KONA array, ISLA runs PMCC on all four elements using two sets of detection parameters ("high-frequency" and "microbarom" sets) for routine event processing, with two additional sets ("high-speed" and "very-low-frequency") in development (Table 1a). Each set uses a suite of second-order Chebyshev filters, with passbands shown in Table 1a. Detection parameters include analysis-window length and overlap, maximum consistency, minimum and maximum frequency and trace velocity, and maximum azimuthal variation permissible for inclusion in a family. Other parameters are dependent on these. The PMCC parameters act as logical "and" constraints, where all conditions must be satisfied for the detection to be registered. The resulting table of detection families is sorted and recorded in the "unfiltered" PMCC bulletin, then analyzed and filtered using various parameter thresholds (Table 1b), which act as logical "or" constraints, where satisfaction of any is sufficient for acceptance. A "filtered" bulletin and a Center for Seismic Studies (CSS) arrival table containing arrival time, azimuth, slowness, amplitude, and phase are created using the detections that are within the thresholds. The waveform data in the local CSS database is stored in 4-hour segments, and the PMCC detector processes an entire segment at once, two hours after its normal ending time (to ensure maximum data inclusion). The four iterations through the waveform data currently require about 20-30 minutes of computation time per 4-hour segment on a dual-processor 900-MHz SunBlade 2000 running Solaris 8. Both filtered and unfiltered bulletins of detections are produced weekly (Table 2).

Event Detection Parameters

The *high-frequency* parameter set uses a passband of 0.5-4 Hz, which effectively screens out the dominant low-frequency energy and allows comparatively low-amplitude events to be detected. Before being written to the arrival database, the arrivals are classified by phase. Currently ISLA personnel use a simple azimuth-based classification scheme derived from past observations of similar high-frequency events (Garces and Hetzer, 2001). Azimuthal ranges that include a known or hypothesized source are given a phase identification based on that source. Current phase classifications include surf noise, signals from the Pohakuloa Training Area, and possible volcanic signals; other signals are given a phase identification that signifies "origin unknown". Events that are believed to be local to the Big Island and its shoreline tend to show higher median frequencies than events that are not associated with specific regions (Figure 2). This is to be expected due to the higher attenuation of high-frequency energy with increasing range.

Surf Arrivals

Detections from azimuths of 234±10° and 320±10° are classified as surf events, with assigned phase names of "ik" and "iws" respectively. The signals generally occur as sets of impulsive, evenly spaced arrivals (Figure 3) with relatively high (> 2 Hz) frequency content (Figure 2). These arrivals are believed to be produced by ocean waves trapped within specific bays along the coast of the Big Island, and have an average root-mean-square (RMS) amplitude of 2.99 mPa. During periods of high activity, groups of surf signals will often be sufficiently closely spaced in time such that the PMCC detector will treat them as a single, long-duration event. Other azimuths may also contribute surf signals, but not with the consistency of the two areas specified above.

Pohakuloa Training Area Arrivals

Detections from 65±30° are identified as coming from the Pohakuloa Training Area and are assigned to the "ip" phase. Pohakuloa events generally occur as clusters of one or more irregularly spaced impulsive arrivals (Figure 4), and tend to have fairly high (> 2 Hz) frequency content (Figure 2). They have an average RMS amplitude of 4.99 mPa. Other signals from this azimuth may be more emergent with poor S/N.

Volcanic Arrivals

Detections from 110±10° are identified as coming from the general direction of Pu'u O'o, the active vent of Kilauea Volcano. These signals are tentatively assigned to the "iv" phase and have a RMS amplitude of 7.13 mPa.. To date the majority of these events have featured a S/N of approximately unity. Despite their relatively high amplitude, the events tend to occur at lower frequencies (mean frequency of detection is 0.9 Hz), where the noise floor is higher. This precludes visual analysis of the arrivals. Some tentative correlations have been found between infrasonic events and peaks of thermal activity in the Pu'u 'O'o crater.

<u>**Microbarom Arrivals**</u>

Detections in the 0.1- to 0.5-Hz frequency band are assigned the "im" phase and are believed to be generated by ocean wave interactions caused by severe weather, often at distances of several thousand kilometers. The arrivals have an average RMS amplitude of 12.57 mPa. Correlation has been drawn between the arrival azimuth of microbarom events (Figure 5) and areas of increased surface wave height. Microbarom energy has been shown to have promise in the field of storm tracking; for a more detailed treatment of this topic see Garcés *et al*. (2002).

<u>**Other Detection Parameters**</u>

The bands that are currently under development will contain events of a less general nature. For example, the "high-speed" band should be mostly useful for events propagating oblique to the ground, such as bolides or aircraft passing overhead, and for events that exhibit seismic phase velocities, such as earthquakes that disturb the microphone. The "very-low-frequency" band will be used for detecting mountain-associated waves that may be generated by Hawaii's and Maui's massive volcanic peaks. Currently the events in these bands are not recorded in the arrival tables or the filtered bulletins, but are present in the unfiltered bulletins (Figure 6).

<u>**CONCLUSIONS AND RECOMMENDATIONS**</u>

The detections of infrasonic signals in Hawaii have been improved through the evaluation of various array-processing algorithms. The effectiveness of the PMCC event detection algorithm at KONA has been demonstrated. Further research on this topic should include the development of real-time event detection and identification algorithms. Real-time detection could include implementation of the Antelope system, which can be run concurrently with the PMCC software for comparative evaluation. Event identification procedures could incorporate neural network techniques, and may permit the construction of a more concise automatic bulleting.

<u>**REFERENCES**</u>

Cansi, Y. (1995). An automatic seismic event processing for detection and location: The P.M.C.C. method. *Geophysical Research Letters*, **22**, 1021-1024.

Cansi, Y., and Y. Klinger (1997). An automated data processing method for mini-arrays. Newsletter of the European-Mediterranean Seismological Center, **11**, 2-4.

Garces, M, and C. Hetzer (2001). Infrasonic signals detected by the Kona array, Hawaii. *23nd Annual DTRA/NNSA Seismic Research Review*, Jackson Hole, 1-5 October 2001.

Garces, M., C. Hetzer, S. Businger and M. Willis (2002). Modeling of microbarom signals in the Pacific. *This volume*.

Garces, M., C. Hetzer, K. Lindquist, and D. Drob (2002). Source location algorithm for infrasonic monitoring. *This volume.*

Table 1. a) Parameters for the two active and two developing sets of detection constraints. b) The secondary constraints used to filter detections into confirmed arrivals. Columns for "High-Frequency" and "Microbarom" sets are currently active and in use at IS59; columns for "High-Speed" and "Very-Low-Frequency" sets are in development.

PMCC Parameter	High-Frequency	Microbarom	High-Speed	Very-Low-Frequency
Window Length	30 sec	90 sec	30 sec	300 sec
Window Overlap	5 sec	20 sec	5 sec	50 sec
Max Consistency	0.2 sec	0.5 sec	0.2 sec	5 sec
Passband	0.5-4.0 Hz	0.1-0.5 Hz	0.5-4.0 Hz	0.033-0.1 Hz
Trace Velocity	0.3-0.45 km/s	0.3-0.45 km/s	0.5-0.8 km/s	0.25-0.45 sec
Min # of Sensors	3	3	3	3
Max Interpixel Time Variation	2 x Window Overlap	2 x Window Overlap	2 x Window Overlap	2 x Window Overlap
Max Interpixel Frequency Variation	0.8 Hz	0.1 Hz	0.8 Hz	0.02
Max Interpixel Azimuth Variation	10°	10°	10°	10°
Max Interpixel Velocity Variation	10%	10%	10%	10%

ISLA Parameter				
Correlation	0.6	0.7	N/A	N/A
Family Size	14	N/A	N/A	N/A

Table 2. Sample filtered bulletin from the high-frequency parameter set showing information typically stored for each arrival. These arrivals satisfy one or both of the ISLA parameters shown in Table 1b.

| Date	Time	Azimuth	Slowness (s/deg)	Correlation	Median Frequency	RMS Amplitude (mPa)	Family Size	Phase
9-Jul-02	00:02:15	323.2	311.65	0.32	2.96	0.8	37	iws
9-Jul-02	00:04:25	323	313.44	0.44	3.15	0.8	53	iws
9-Jul-02	00:06:45	322.7	312.54	0.45	3.07	0.9	46	iws
9-Jul-02	00:08:25	322.7	314.34	0.33	3.31	0.6	15	iws
9-Jul-02	00:09:15	323	314.34	0.45	3.35	0.7	27	iws
9-Jul-02	00:14:15	322.5	314.34	0.36	3.05	0.7	25	iws
9-Jul-02	00:22:25	316.6	312.54	0.66	2.45	2.1	24	iws
9-Jul-02	00:32:40	40.3	305.54	0.46	3.3	0.8	18	ip
9-Jul-02	00:59:45	48.5	297.21	0.48	2.52	1.5	38	ip
9-Jul-02	01:25:35	49.6	300.49	0.78	0.88	8.4	7	ip
9-Jul-02	01:34:20	57.6	314.34	0.31	2.31	1.2	18	ip
9-Jul-02	01:35:30	59	313.44	0.33	2.45	1.2	42	ip
9-Jul-02	01:37:55	57.3	312.54	0.28	2.39	1.2	19	ip
9-Jul-02	01:39:10	58.9	312.54	0.23	2.47	0.9	15	ip
9-Jul-02	02:15:20	308.1	317.09	0.47	2.3	2	43	iu
9-Jul-02	02:35:20	232.5	326.58	0.52	3.51	0.4	21	ik
9-Jul-02	02:38:15	232.4	324.63	0.44	3.55	0.4	20	ik
9-Jul-02	02:46:55	232.3	325.6	0.41	3.46	0.4	26	ik
9-Jul-02	02:59:15	231.8	322.71	0.32	3.54	0.3	21	ik
9-Jul-02	03:02:30	114.4	303.84	0.65	0.73	7.8	6	iv
9-Jul-02	03:53:45	232.4	324.63	0.44	3.3	0.5	24	ik
9-Jul-02	04:03:20	234.4	327.56	0.4	3.61	0.3	23	ik
9-Jul-02	04:08:15	232	323.67	0.36	3.5	0.3	16	ik
9-Jul-02	04:12:05	234.6	329.54	0.4	3.66	0.3	15	ik
9-Jul-02	04:13:25	232.6	325.6	0.46	3.46	0.9	59	ik
9-Jul-02	04:30:30	232.4	325.6	0.41	3.5	0.4	37	ik
9-Jul-02	04:40:55	75.3	281.85	0.5	3.31	0.5	23	ip
9-Jul-02	04:45:25	232.6	325.6	0.47	3.54	0.5	29	ik
9-Jul-02	04:53:00	232.4	327.56	0.48	3.37	0.5	24	ik
9-Jul-02	05:01:05	233.2	325.6	0.4	3.5	0.4	39	ik
9-Jul-02	05:02:30	232.4	323.67	0.38	3.57	0.4	26	ik
9-Jul-02	05:06:00	233	326.58	0.47	3.45	0.5	16	ik
9-Jul-02	05:08:35	232.7	329.54	0.44	3.55	0.5	19	ik
9-Jul-02	05:29:45	232.8	324.63	0.39	3.52	0.4	29	ik
9-Jul-02	05:41:45	232.5	326.58	0.38	3.55	0.4	14	ik
9-Jul-02	05:53:45	232.6	326.58	0.44	3.28	0.6	191	ik
9-Jul-02	06:01:35	232.2	320.82	0.41	3.6	0.5	34	ik
9-Jul-02	06:05:30	115	309.88	0.61	0.73	9.8	6	iv
9-Jul-02	06:12:25	232.6	325.6	0.42	3.59	0.5	36	ik
9-Jul-02	06:21:55	233.1	327.56	0.46	3.5	0.5	14	ik
9-Jul-02	06:43:20	234	327.56	0.39	3.58	0.5	17	ik
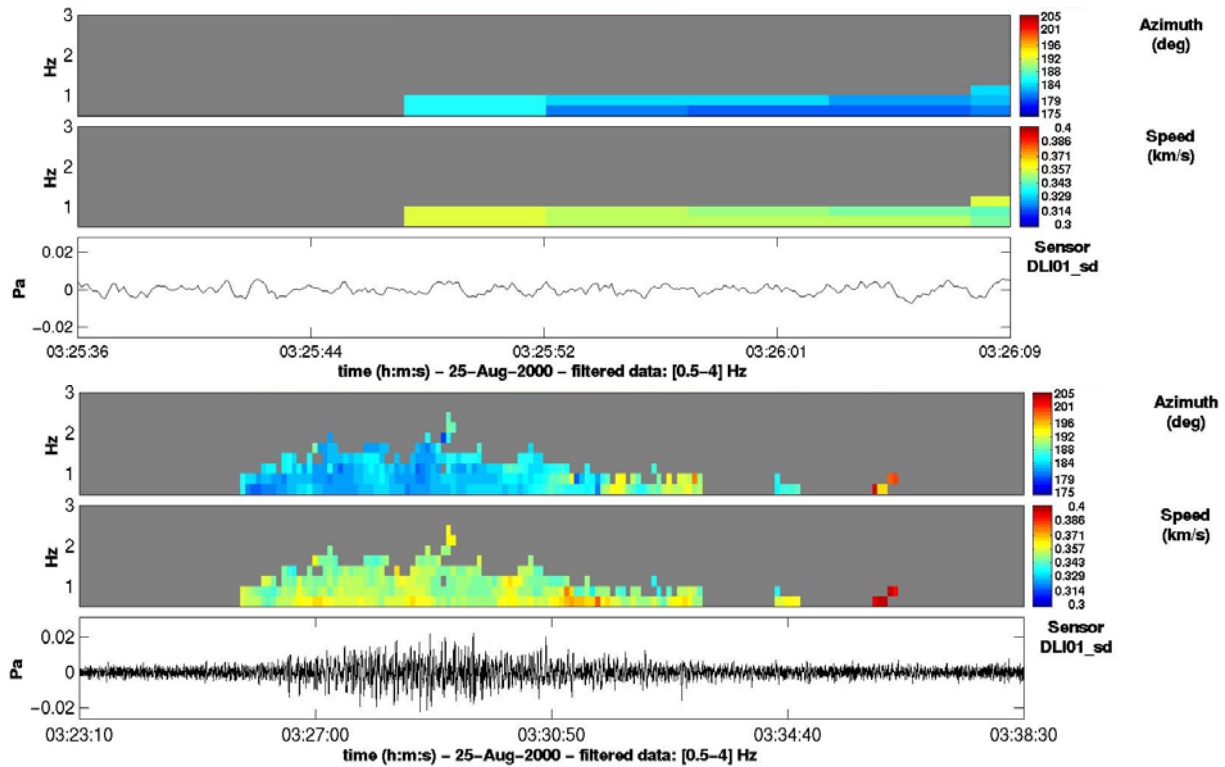
Figure 1. Graphical PMCC windows showing a) the pixel-like nature of an event family (above) and b) a large event family (below). Images are from the bolide event of August 25, 2000 (Garces *et al*., 2002).
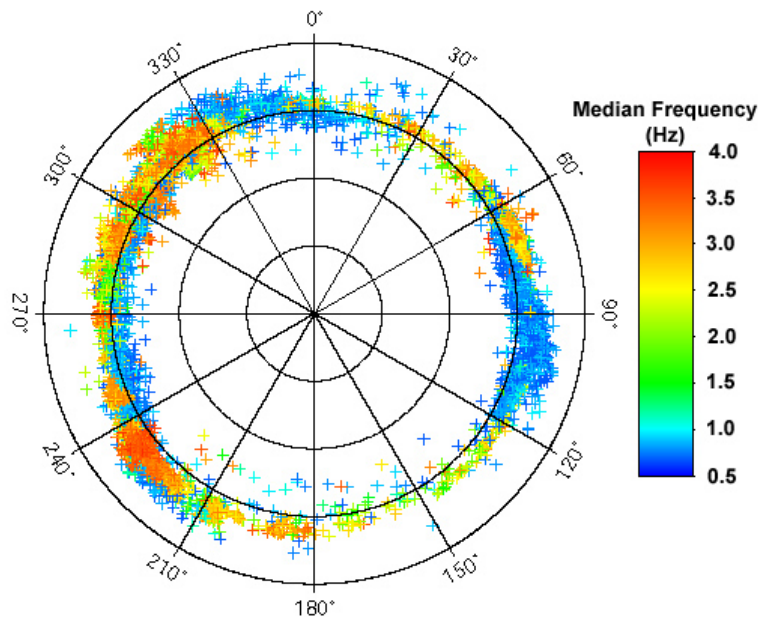

Figure 2. Polar diagram showing azimuth, slowness, and median frequency for arrivals in the "high-frequency" passband detected from January 1-June 30, 2002. Groups of arrivals at 75° (ip phase), 235° (ik phase), and 320° (iws phase) are believed to originate within 50 km of the array. Radial units are seconds/degree, increments of 100.
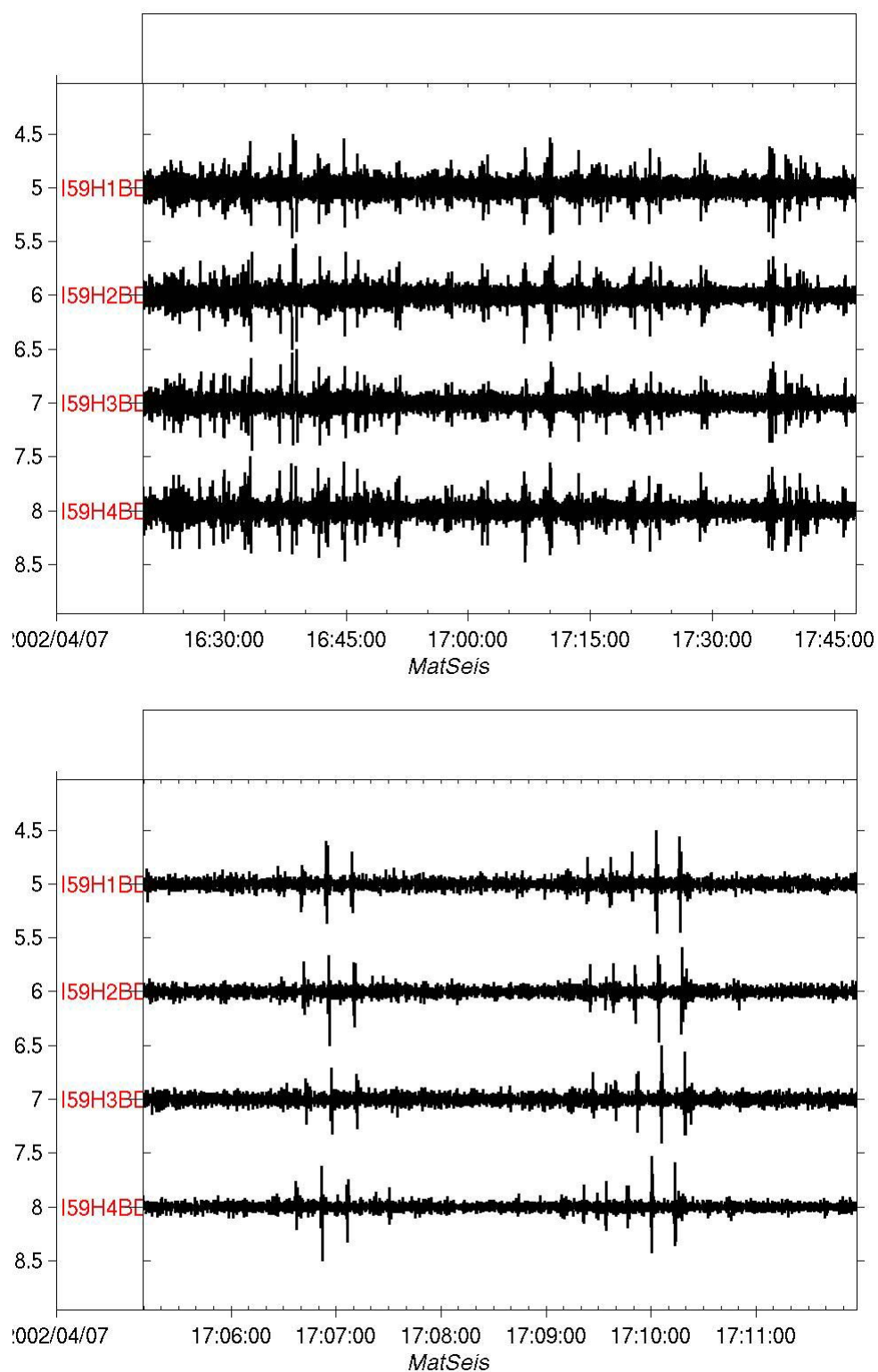
Figure 3. Bandpass-filtered waveform of typical "ik" surf arrival showing regular spacing in time both of groups of arrivals (above) and of individual arrivals (below).
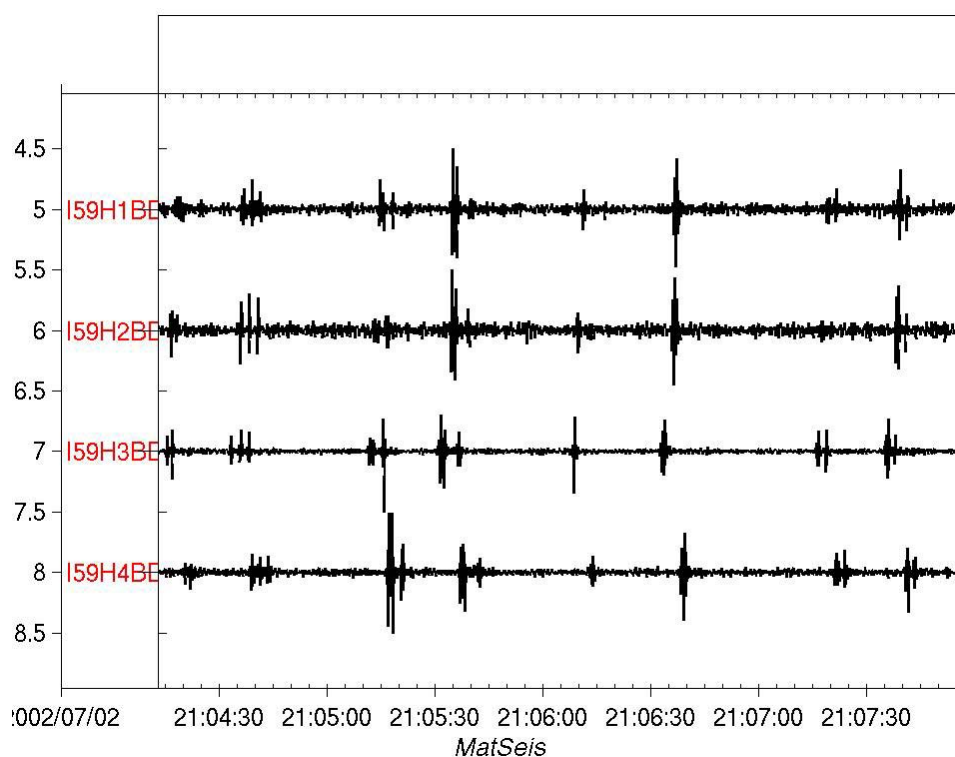
Figure 4. Bandpass-filtered waveform of typical "ip" events showing impulsive quality and irregularity in time.
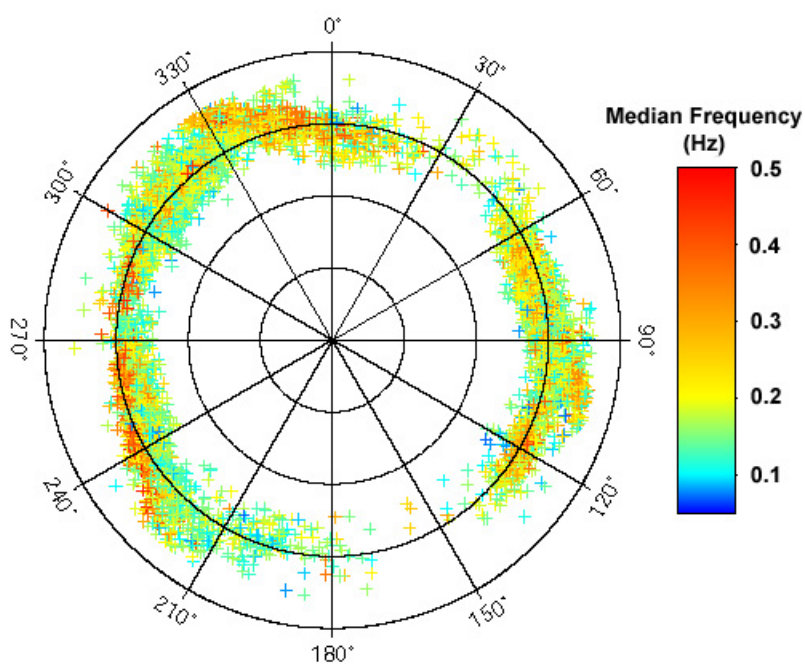

Figure 5. Polar diagram showing arrival azimuth, trace slowness, and median frequency of microbarom events detected from January 1-June 30 2002. Radial units are seconds per degree, increments of 100.
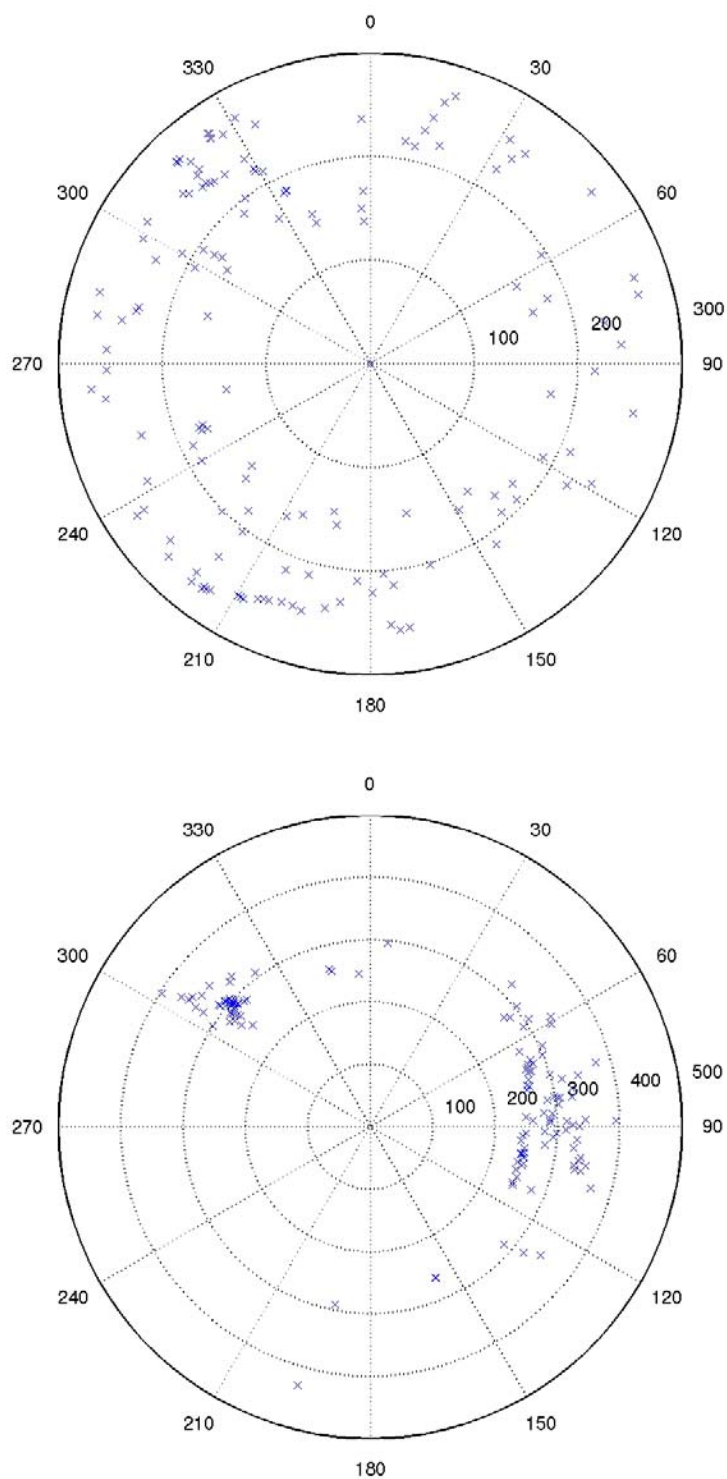
Figure 6. Polar diagrams showing arrival azimuth and trace slowness for detections made by high-speed (above) and very-low-frequency (below) detection parameter sets. Radial units are seconds per degree.

SOURCE LOCATION ALGORITHM FOR INFRASONIC MONITORING

Milton Garces,[1] Claus Hetzer,[1] Kent Lindquist,[2] and Douglas Drob[3]

University of Hawaii Manoa,[1] Lindquist Consulting,[2] and Naval Research Laboratory[3]

ABSTRACT

Two large bolides have been recorded by International Monitoring System (IMS) infrasound stations in Hawaii and Alaska. On 25 August 2000 at 01:12:25 UTC, Department of Defense and Department of Energy satellites observed an object at 14.45 North and 106.13 West, with a total visible estimated energy of 1.4×10^{12} joules. This object, known as the Acapulco bolide, was observed by IMS stations in Hawaii, Alaska, Bolivia, Canada, and French Guiana, as well as by DLIAR in New Mexico. On 23 April 2001, at 06:12:35 UTC, satellites observed an object at an altitude of 28.5 km at 27.9 North and 133.89 West, with a total visible energy estimate of 4.6×10^{12} joules. This bolide explosion was observed by IMS stations in Hawaii, Alaska, California, Canada, and Germany. We use these two events to study the capabilities and limitations of source location procedures based on travel times and azimuth deviations that are derived from ray tracing formulations. A software algorithm has been developed to ingest accurate atmospheric profiles, which may be provided in near-real-time, use the tau-p method to compute the effective speed, or celerity, of specified infrasonic phases, and export these model results into any standard location algorithm, such as the Generic Locator (genloc) module within the Antelope software platform. This implementation is flexible as well as computationally efficient, and allows the exploitation of Center for Seismic Studies (CSS) (now Center for Monitoring Research) database structures and analysis tools.

OBJECTIVE
The aim of this work is to describe a ray-tracing algorithm for locating infrasonic sources, and to apply this algorithm to the determination of the position and origin time of two bolides detected by infrasound arrays in Hawaii and Alaska.

RESEARCH ACCOMPLISHED

Introduction
The tau-p method of Garcés *et al*. (1998, 2001, 2002) has been refined to clearly identify propagating infrasonic phases. Broadband infrasonic array measurements can be used to extract the amplitude, arrival time, apparent horizontal phase velocity, and azimuth of an arrival. All parameters can be estimated as a function of frequency using the PMCC method (Garcés and Hetzer, 2002). These detection parameters can be used to identify a phase, which is a prerequisite for estimating a source location. Given an atmospheric model, travel-time curves and azimuth deviations can be computed for each phase at any specified arrival azimuth. The apparent speed, or celerity, of a guided arrival is defined as the ratio of the range to the travel time for one or more multi-path bounces. Infrasonic phases identified to date are defined in Table 1, and are compatible with Brown's (1999) nomenclature and the IAVCEI list of propagating seismic phases.

Initial studies concentrated on an exact specification of the propagation path (Le Pichon *et al*., 2002a,b; Liszka and Garcés, 2002), and these works were successful in cases when the range from the source to the receiver was not too large or along the dominant stratospheric wind direction. However, the detection of signals with high celerity propagating against the dominant stratospheric wind direction and the observation of apparent horizontal phase velocities lower than the speed of sound at the ground suggest that the interaction of infrasonic waves with atmospheric or topographical structures may scatter and diffract energy from elevated wave guides into the ground. We illustrate the critical issue of phase identification and the application of the location algorithm by using the bolide explosions of April 23, 2001, and August 25, 2000, as case studies. Because of its greater simplicity, we begin with an analysis of the 2001 bolide.

Event Selection and Array Detections of the April 23, 2001, Bolide
Infrared sensors aboard US Department of Defense (DOD) satellites detected the impact of a bolide on 23 April 2001 at 06:12:35 UTC (988006355 Epoch time). The bolide appeared to explode at an altitude of 28.5 km above the coordinates of 27.9 North and 133.89 West. The impact was simultaneously detected by space-based visible wavelength sensors operated by the US Department of Energy (DOE). The total energy in the visible band was 4.6 X 10^{12} joules. The location for the April 23 event determined by the optical systems is referred to as LO1. Since bolides often propagate at speeds of a few tens of kilometers per second, and there is no guarantee that the infrared detection coincided with the infrasonic signal generation, we postulate that the time of the LOI is more precise than the location of the detection.

The locations of the three nearest IMS arrays that detected the April 23 event are given in Table 2.1, and are shown in the upper panel of Figure 1. The upper panels of Figures 2-5 shows the PMCC (Garcés and Hetzer, 2002) detections for all three arrays. Comparison with the InfraTool detections for IS59 (Garcés *et al*., 2001) shows that the first arrivals for PMCC are 226 seconds (4.4 minutes) earlier than the InfraTool first arrivals. This is an important result, as the first arrival time and the phase identification of that first arrival are essential to the location of infrasonic sources. Table 2.2 shows the maximum celerity values for select propagating phases. The list of Table 1 outlines all candidate phases, but for propagating ranges greater than a few thousand kilometers, it is difficult to sustain the *iw* phases and the *Iw*, *Is*, and *It* phases are not applicable. For long ranges, *is* phases are also found to be unstable, as the stratospheric winds can vary significantly along a meridian. However, the *it*, *itd*, and *isd* phases are found to exist for almost all azimuths and geographic locations. Only when an *is* phase exists does the *itd* phase disappear. For long ranges, the time contribution from the source height to the ground or the source height to the upper waveguide boundary is negligible, multiple bounces produce overlapping travel-time curves that begin to appear as a continuous curve, and shadow zones disappear. The *itd* and *isd* phases (Table 1) correspond to leaky wave guides that are suspended above the ground, but either scatter or diffract acoustic energy to the ground. Sources that explode at heights of ~30 km, such as the April 23 bolide, place acoustic energy in the middle of the low-velocity zone of the stratosphere, and thus efficiently trap energy in the stratospheric duct. This waveguide would be able to duct energy with minimal attenuation, and most first arrivals with high celerity may be attributed to *isd* phases. Due to the continuous appearance of travel-time curves and the further degradation of shadow zones by

scattering and diffraction, we opt to use the celerity as the key propagation model output for the source location iteration.

Infrasonic Location Procedure for April 23 Event

From intersecting back azimuths, it is possible to produce a seed location for the source inversion procedure. However, as can be seen in Figure 1, the back azimuth location may be expected to be in error. An initial origin time can be obtained from the seed location by assuming a constant celerity of 0.3 km/s and computing the great circle paths to the source. Alternatively, if ground truth is known on an event, such as the epicentral location issued by the DoD release, the range of each station to the source and the expected azimuth of the incoming signal can be readily computed. Once an initial azimuth from source to receiver is determined, the tau-p method of Garcés *et al*. (1998, 2002) can be used to compute the celerity of each propagating phase. The lower panels of Figures 2-4 show the celerity computed at each array for the April 23 bolide using the Naval Research Laboratory's (NRL) SAGE atmospheric profiles that include accurate specifications of the troposphere and stratosphere (Garcés *et al*., 2001). The estimated times of arrival of the first or second arrival at the station were used to compute the residuals from a grid search around the seed source location and origin time. Various locations were made assuming different phase identifications for both first and second arrivals (when present), but only two solutions (with the minimal residuals) are shown in Table 2.3. The first solution, LA_S1, assumes all first arrivals correspond to *isd* phases, and produced a very good match to the origin time provided by the satellite observation (LO1). Although in seismic location an 8-s time differential is unacceptable, when scaled to the total travel time of the signal, the percent error is small and comparable to the best seismic location accuracies (Table 2.4). The difference in the source location between LO1 and LA_S1 may be attributed to the high speed of the bolide and could correspond to a difference in where the peak sound and infrared energy are radiated. This result suggests that *isd* phases can be used to explain the arrival of signals in the upstream stratospheric direction, and the relatively higher frequency of the first arrivals observed in Figure 2 and 3 suggest that scattering is an important factor. A second solution, LA_S2, assumed that the first arrival at IS53 was an *isd* phase, the second arrival at IS57 was an *itd* phase, and the second arrival at IS59 was an *isd* phase. These phases were selected in an attempt to match the source location at the expense of the origin time. However, we favor the first solution because we believe the uncertainty in time (~10 s) may be less than the uncertainty in position for the satellite location LO1.

Infrasonic Location Procedure for the August 25, 2000, Event

The August 25, 2000, bolide, known as the Acapulco bolide, is more difficult to unravel. Table 3.1 shows the infrasonic observations for the Acapulco bolide. The arrival information for the stations in South America was derived from PMCC results (Le Pichon, personal communication, 2000). The lower panel of Figure 1 shows the station locations and back azimuths, again showing a poor azimuth fit of some of the stations to the actual source location. In general, it appears that the worst azimuth deviations occur in stations with extreme topography along the propagation path, specifically IS53 (Alaska) and IS08 (Bolivia). From the seed locations, azimuths from the stations to the source were estimated and the celerity computed at each station. Table 3.2 shows the maximum celerity for each phase. Figure 6 shows the PMCC detection at DLIAR, the closest station, and the change in detection azimuth with time. Following the same procedure as for the April 23 event, we computed locations for various permutations of phase identifications for the first and second arrival times. An attempt was also made to separate the detections into two events, one recorded by the US stations and another by the South American stations. However, two-station locations are inherently unstable, and even the solution using the three US stations was unstable because of the near parallel alignment of the DLIAR and IS53 propagation paths from the source. Three solutions are shown in Table 3.3. The first solution, LA_DL1, assumes all first arrivals are *isd* phases, and yielded a large error on the origin time estimate as well as in the time differentials for some of the stations (Table 3.4). The second solution, LA_DL2, assumed a combination of *it*, *itd* and *isd* phases (Table 3.5) and yielded a good fit to the origin time, although the time differentials per station are not as good as the April 23 solution. A source location west of the LO1 location is consistent with the DLIAR observations. Further work is needed to determine whether this event consists of a single bolide or more than one bolide arriving at different times, as suggested by the infrasound detections from IS25.

CONCLUSIONS AND RECOMMENDATIONS

Infrasonic estimates of the origin time and location of the April 23 event were performed using realistic atmospheric profiles and the tau-p method to estimate the celerity of propagating phases in the atmosphere. Arrivals corresponding to phases propagating in leaky stratospheric ducts produced the best fit to the origin time obtained from the satellite infrared detection. This existence of these leaky stratospheric ducts may explain how stratospheric

phases can be observed along both the upstream and downstream dominant stratospheric wind directions. Further work is needed on how topography and perturbations in the atmosphere can scatter and diffract infrasonic energy into and out of elevated wave guides. The next generation of the tau-p software will address propagation in range-dependent environments.

REFERENCES

Brown, D.J. (1999). Summary of infrasound source location meeting: San Diego, November 9-10, 1998, *Center for Monitoring Research*, Arlington, VA.

Garcés, M, and C. Hetzer (2002). Evaluation of infrasonic detection algorithms. *This volume.*

Garcés, M., D. Drob, and M. Picone (2002). A theoretical study of the effect of geomagnetic fluctuations and solar tides on the propagation of infrasonic waves in the atmosphere. *Geophys. J. International*, **148**, 77-87.

Garcés, M, C. Hetzer, K. Lindquist, and R. Hansen, J. Olson, C. Wilson, D. Drob, M. Picone, (2001). Infrasonic location of the April 23, 2001, Bolide event. *23nd Annual DTRA/NNSA Seismic Research Review*, Jackson Hole, 1-5 October 2001.

Garcés, M, D. Drob, M. Picone, K. Lindquist, and R. Hansen (2000). Characterization Of Infrasonic Waves Observed In Hawaii During Summer, *22nd Seismic Research Symposium: Planning for Verification of and Compliance with The Comprehensive Nuclear-Test-Ban Treaty*, New Orleans.

Garcés, M. A., R. A. Hansen, and K. Lindquist (1998). Travel times for infrasonic waves propagating in a stratified atmosphere, *Geophys. J. International*, **135**, 255-263.

Le Pichon, A. M. Garcés, E. Blanc, M. Barthélémy, D. Drob (2002). Acoustic propagation and atmosphere characteristics derived from infrasonic waves generated by the Concorde. *J. Acoust. Soc. Am.*, **111**, 629-641.

Le Pichon, A., J. Guilbert, A. Vega, and M. Garcés (2002), Ground-coupled air-waves and diffracted infrasound from the Arequipa earthquake of June 23, 2001, *Geophysical Research Letters* (in press).

Liszka, L., and M. Garcés (2002), Infrasonic Observations of the Hekla Eruption of February 26, 2000. *Journal of Low Frequency Sound* (in press).

Kulichkov, S. N. (1998). On problems of infrasonic monitoring of small energy explosions, *Proceedings of the Informal Workshop on Infrasound,* Bruyers-Le-Chatel, France.

Table 1. Preliminary phase identification nomenclature for long-range infrasonic propagation

Phase ID	Description	Typical celerity of first arrival, m/s
iw	Guided wave propagating between the tropopause and the ground.	330-340
is	Guided wave propagating between the stratopause and the ground.	310-330
isd	Guided wave propagating in elevated waveguide between stratopause and the troposphere, and diffracted or scattered to the ground. May have higher frequency.	310-330
it	Guided wave propagating between the lower thermosphere and the ground.	280-300
itd	Guided wave propagating in elevated waveguide between the lower thermosphere and the troposphere, and diffracted or scattered to the ground.	280-300
It, Is, Iw	Direct arrival from the source to the receiver. May have high apparent phase velocity	N/A

Table 2.1. First arrival observations of April 23, 2001, bolide by three nearest IMS infrasound stations

Station	Lat (N)	Lon (E)	Speed (m/s)	Azimuth	ETA (epoch)
IS53	64.87	-147.84	322	150.6	988020690
IS57	33.6	-116.5	349	256.1	988012060
IS59	19.59	-155.9	348	63.6	988013790

Table 2.2. Predicted first arrival celerity (km/s) for select phases: April 23, 2001

	it	itd	isd
IS53	0.268	0.284	0.292
IS57	0.278	0.292	0.328
IS59	0.284	0.3	0.311

Table 2.3. Source location and errors relative to satellite location (LO1): April 23, 2001

Source	Lat (N)	Lon (E)	Origin Time (Epoch)	Lat error (deg)	Lon error (deg)	Time error (s)
LO1	27.9	-133.89	988006355	0	0	0
LA_S1	28.07	-135.09	988006347	0.17	-1.2	-8
LA_S2	27.79	-133.42	988006145	-0.11	0.47	-210

Table 2.4. Phase selection and time error for LA_S1 solution: April 23, 2001
PA = predicted arrival; ETA = first arrival time; OT = origin time

Station	Selected Phase	Range to LA_S1	X/T (km/s)	Predicted arrival	Time Error /Travel Time	PA-ETA	PA-OT	Ratio (%)
IS53	isd	4191	0.292	988020700	-0.06%	10	14353	0.07
IS57	isd	1877	0.328	988012070	-0.14%	10	5723	0.17
IS59	isd	2313	0.311	988013784	-0.11%	-6	7437	0.08

Table 3.1. First arrival observations of August 25, 2000, bolide by infrasound stations.

Station	Lat (N)	Lon (E)	Speed (m/s)	Azimuth	ETA (epoch)
IS08	-16.3	-68.1	340	298	967184490
IS25	5.2	-52.7	344	283	967187730
IS53	64.87	-147.84	355	144	967187230
IS59	19.59	-155.9	346	88	967182900
DLIAR	35.87	-106.33	360	180	967173900

Table 3.2. Predicted first arrival celerity (km/s) for select phases: August 25, 2000

	it	itd	isd
IS08	0.289		0.298
IS25	0.263	0.285	0.29
IS53	0.292	0.303	0.31
IS59	0.281	0.297	0.308
DLIAR	0.278		0.309

Table 3.3. Source location and errors relative to satellite location (LO1): August 25, 2000

Source	Lat (N)	Lon (E)	Origin Time (Epoch)	Lat error (deg)	Lon error (deg)	Time error (s)
LO1	14.45	-106.13	967165945	0	0	0
LA_DL1	13.68	-108.21	967166247	-0.77	-2.08	302
LA_DL2	13.37	-107.74	967165950	-1.08	-1.61	5

Table 3.4. First arrival phase selection and time error for LA_DL1 solution: August 25, 2000

Station	Selected Phase	Range to LA_DL1	X/T (km/s)	Predicted Arrival	Time Error / Travel Time	PA-ETA	PA-OT	Ratio (%)
IS08	isd	5513	0.298	967184747	1.63%	257	18500	1.39
IS25	isd	6149	0.290	967187450	1.39%	-280	21203	-1.32
IS53	isd	6432	0.310	967186995	1.42%	-235	20748	-1.13
IS59	isd	5110	0.308	967182838	1.78%	-62	16591	-0.37
DLIAR	isd	2464	0.309	967174221	3.80%	321	7974	4.03

Table 3.5. First arrival phase selection and time error for LA_DL2 solution: August 25, 2000

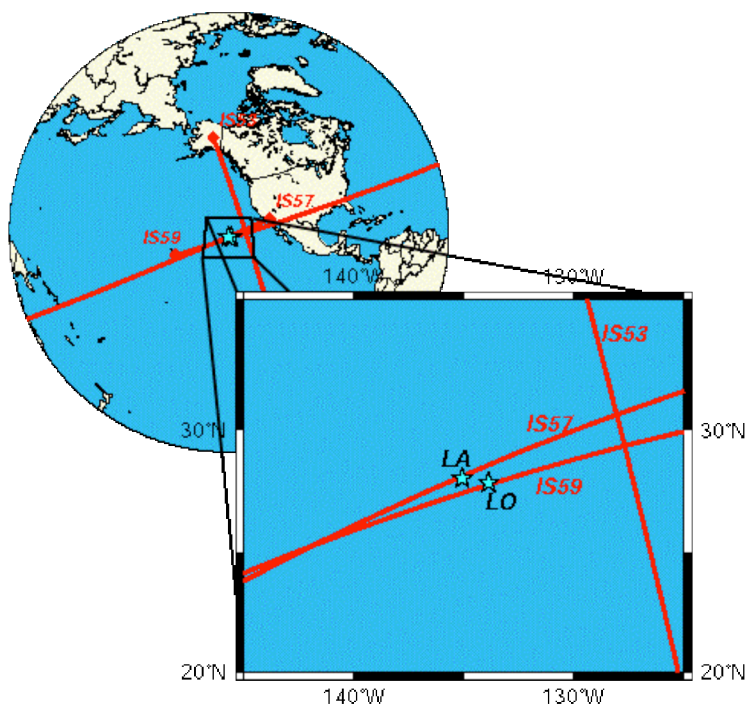| Station	Selected Phase	Range to LA_DL2	X/T (km/s)	Predicted Arrival (PA)	Time error / Travel time	PA-ETA	PA-OT	Ratio (%)
IS08	it	5452	0.289	967184815	0.03%	325	18865	1.72
IS25	itd	6096	0.285	967187339	0.02%	-391	21389	-1.83
IS53	itd	6481	0.303	967187339	0.02%	109	21389	0.51
IS59	isd	5168	0.308	967182729	0.03%	-171	16779	-1.02
DLIAR	isd	2495	0.309	967174024	0.06%	124	8074	1.54

Figure 1. Satellite (LO) and infrasonic (LA_S1) location for the April 23, 2001, bolide. The observed arrival azimuths at infrasound arrays IS53, IS57, and IS59 are shown as red lines.

Figure 2. Satellite (LO) and infrasonic (LA_DL2) location for the Acapulco bolide. The observed arrival azimuths at infrasound arrays IS08. IS25, IS53, DLIAR, and IS59 are shown as red lines.
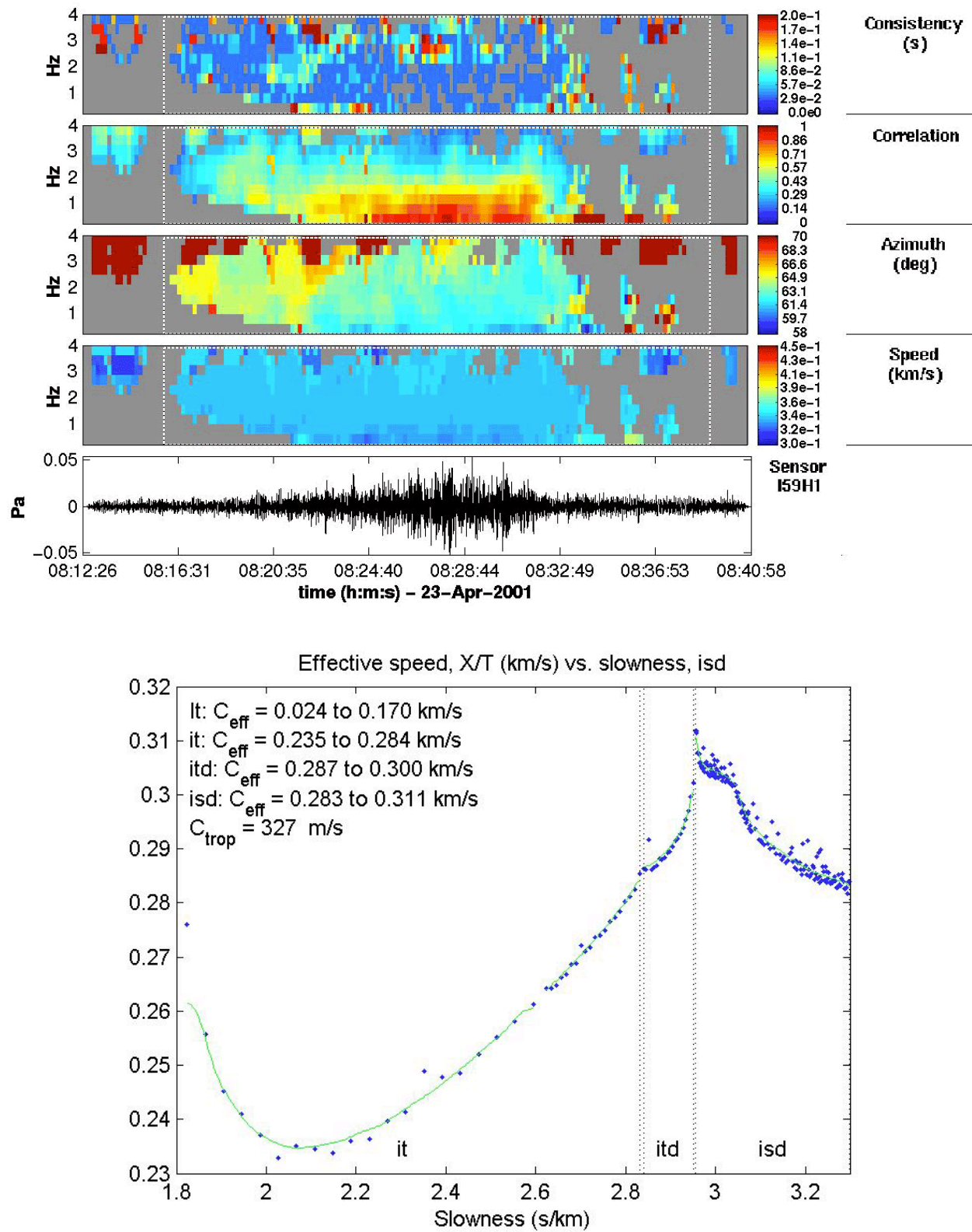
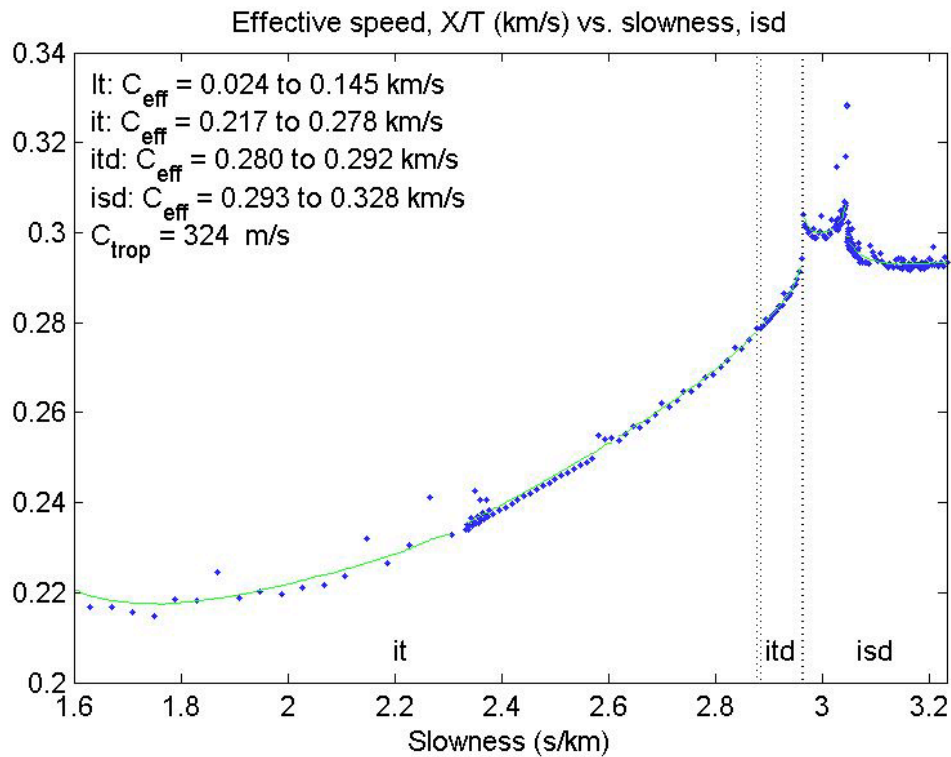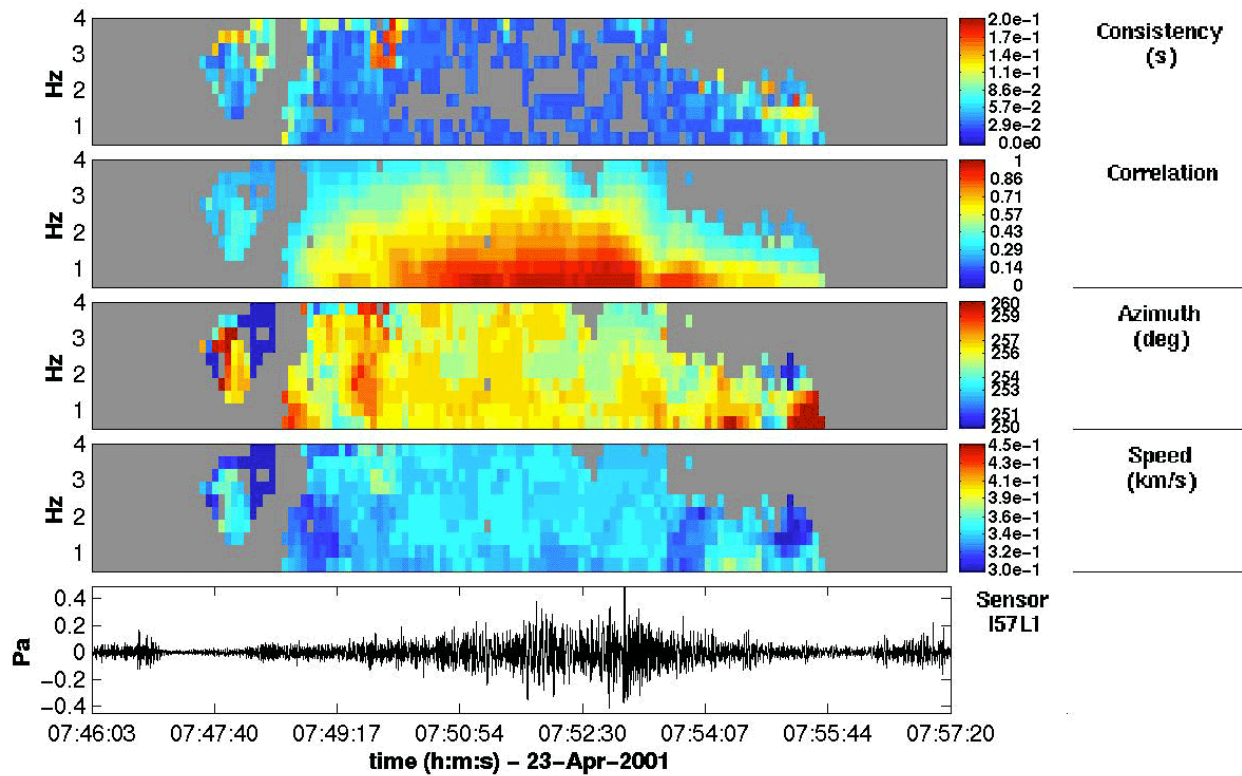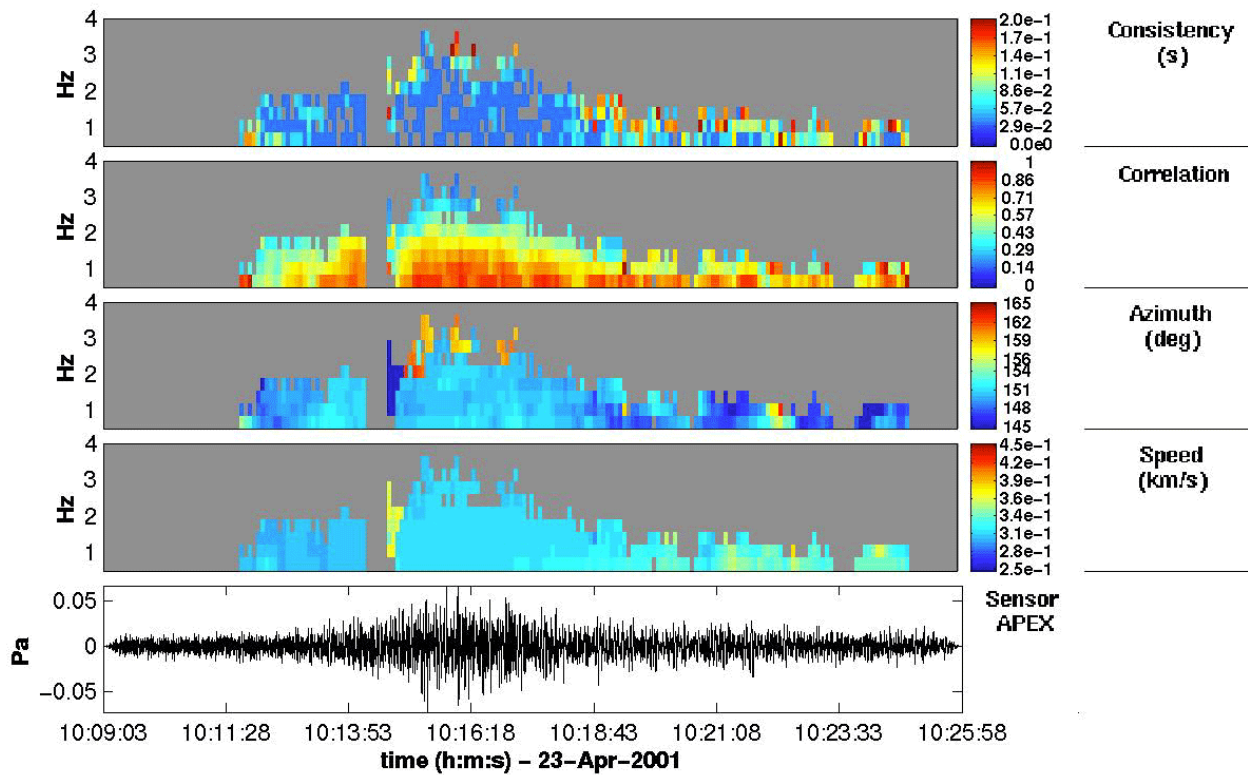**Figure 3. Detection and predicted celerity at IS59, Hawaii, for April 23, 2001, bolide.**

Figure 4. Detection and predicted celerity at IS57, Piñon Flats, for April 23, 2001, bolide.
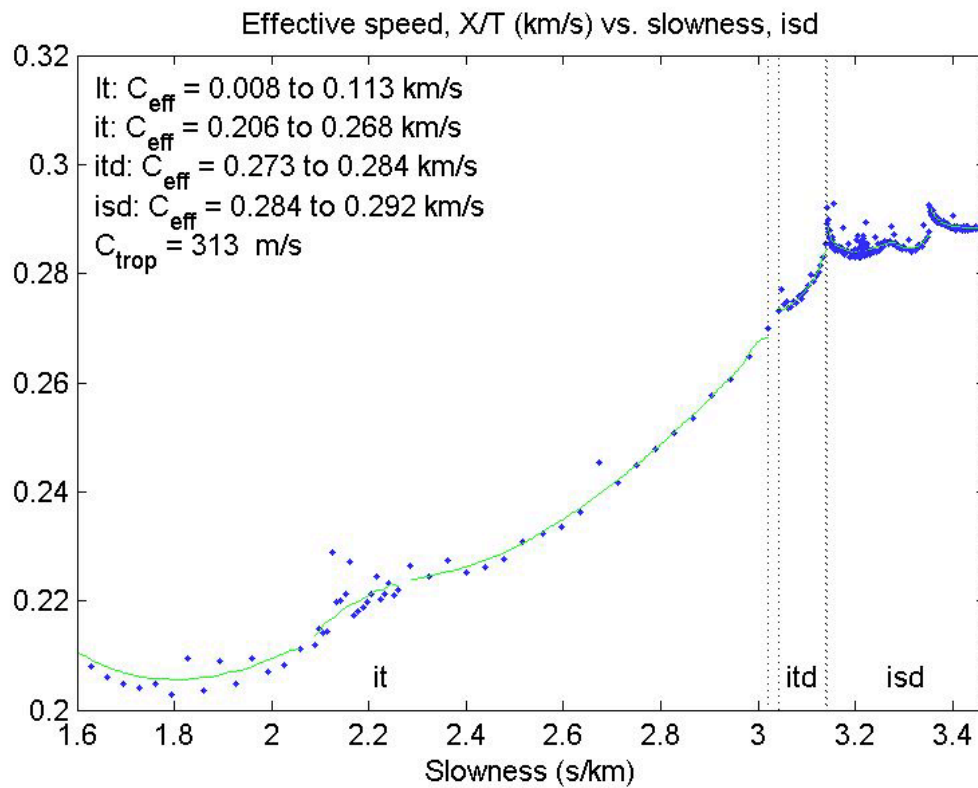
Figure 5. Detection and predicted celerity at IS53, Fairbanks, Alaska, for April 23, 2001, bolide.
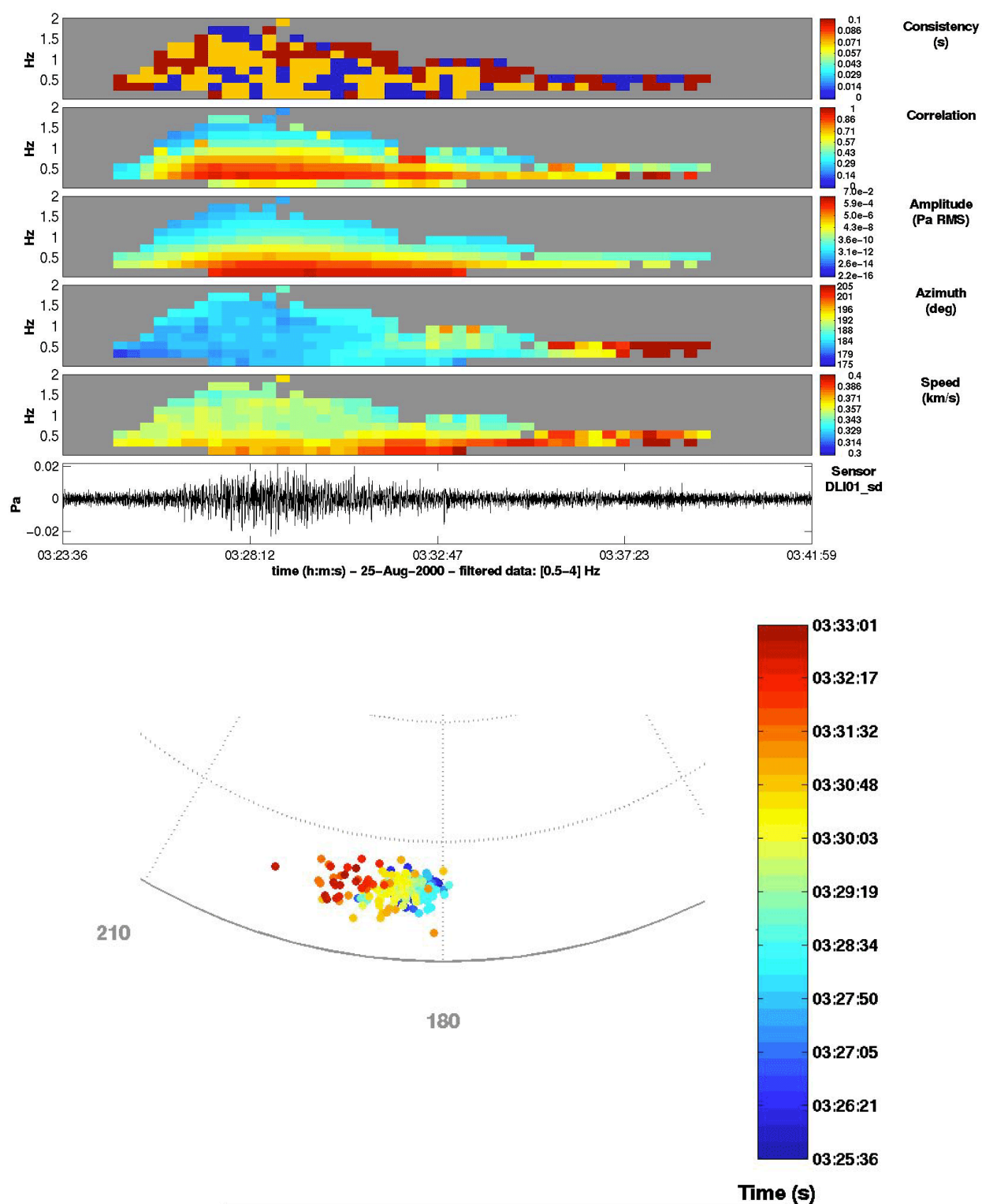
Figure 6. Detections and azimuth changes as a function of time observed at DLIAR, New Mexico, for the Acapulco bolide.

MODELING OF MICROBAROM SIGNALS IN THE PACIFIC

Milton Garcés, Claus Hetzer, Steven Businger, and Mark Willis

University of Hawaii, Manoa

ABSTRACT

Severe weather in the ocean generates infrasonic signals in the 0.1- to 0.5-Hz frequency band that can propagate for thousands of kilometers. The source generation mechanism for microbaroms is believed to be the same as for microseisms, and is attributed to the nonlinear interaction of surface ocean waves. We compare theoretical predictions with infrasonic observations of Hurricane Daniel in July of 2000. The nonlinear interaction of the ocean wave field is predicted to radiate sound waves only if the ocean waves are almost opposite in direction and of a near identical frequency. However, perfectly opposing wave trains of the same frequency radiate vertically, and this acoustic energy never returns back to the earth. Only opposing wave trains that are slightly off line or with slightly different frequencies will result in isotropic acoustic radiation, even for highly directional ocean wave fields. The slowness of the infrasonic waves observed by International Monitoring System (IMS) array IS59, or KONA, suggests that these waves were propagating close to the horizontal. The observed azimuth of the incident sound waves corresponds to the most energetic stage of Daniel's lifespan, and suggests that the acoustic signals were radiated during the interaction of surface gravity waves in the open ocean. Using the known dispersion relation for deep water waves, the median detection frequency corresponds to ocean wave speeds that are slower than the known hurricane track speed of Daniel, a condition that would encourage the nonlinear interaction.

OBJECTIVE

The aim of this work is to characterize microbarom signals observed in the Pacific and model the source processes that generate these signals, with the aim of determining infrasonic detection thresholds in the microbarom frequency range.

RESEARCH ACCOMPLISHED

1. Introduction

Infrasonic signals known as microbaroms consist of pressure oscillations with dominant periods of 4-7 s, and they can appear as energy bursts or as a continuous oscillation that can last for hours or days. In the frequency domain, microbaroms appear as a broad frequency peak centered around 0.2-0.3 Hz (Figure 1). Like microseisms in seismology (Kibblewhite and Wu, 1996), microbaroms are thought to be generated by the nonlinear interaction of ocean surface waves. For infrasonic stations near the ocean, microbaroms determine the noise floor in the 0.1-0.5 Hz frequency band, and thus determines the detection thresholds in that band. In Hawaii, microbarom signals are determined from all azimuths (Garces and Hetzer, 2002), and the dominant signal is usually corresponds to either the closest storm to the recording station or the largest wave heights associated with severe weather in the Pacific.

2. Theoretical background

Our starting assumption is that the source generation mechanisms for microbaroms is similar to that of microseisms. However, microseisms and microbaroms will have very different propagation paths. Energy launched near a vertical angle to the ocean surface and towards the ocean floor couples well with the bedrock, and energy launched just below the ocean surface may not reach the ground. In contrast, energy launched near a vertical angle into the atmosphere never returns back to the Earth, and most of the infrasonic signals recorded by ground stations correspond to energy launched near the horizontal angle at the source. The radiation pattern of microbarom sources is discussed below.

For a specified ocean surface wave velocity u_z, the far-field acoustic pressure, p, in a homogeneous atmosphere can be expressed as (Arendt and Fritz, 2000),

$$p\left(x,y,z,t-\frac{R}{c}\right) = -\frac{\rho_0}{8\pi c}\frac{\partial}{\partial t}\int \frac{z}{R^2}u_z^2 dx'dy'$$

$$R^2 = (x-x')^2 + (y-y')^2 + z^2$$

where x, y, and z are the spatial coordinates in a Cartesian reference frame, x' and y' are the Cartesian coordinates of integration over the ocean surface, ρ_o is the atmospheric density, and c is the atmospheric sound speed. Note that the acoustic pressure is proportional to the integral of the square of the ocean surface velocity. After expressing the ocean surface velocity as sinusoidal terms corresponding to propagating surface wave trains, we find propagating acoustic solutions only exist for surface waves that interact with each other at near the same frequency and nearly anti-parallel directions. All other solutions are non-propagating.

The period and amplitude of an ocean wave depend on the wind speed and fetch of a severe weather disturbance. Although high wind speeds are possible in a hurricane, such winds are usually highly localized, have a relatively small fetch, and thus do not efficiently generate large ocean waves. Ocean surface waves that propagate for long ranges usually have periods of 8-12 seconds. Due to the nonlinear interaction introduced by the square of the velocity, the acoustic solution will have approximately twice the ocean wave frequency (frequency doubling). This can be understood as an acoustic coupling, as for sound to be efficiently radiated in the atmosphere it is necessary for the horizontal wavelength of the ocean wave field to match the acoustic wavelength. Due to the slow propagation speed of deep water waves, their wavelength tends to be too small for acoustic coupling unless two surface wave trains are propagating nearly opposite to each other, in which case one of the nonlinear terms allows the existence of a large horizontal wavelength (small horizontal wave number) that encourages efficient coupling to the atmosphere. This nonlinear term corresponds to an acoustic frequency that is the sum of the frequencies of the interacting surface wave trains, or approximately twice the dominant frequency of the ocean wave. Figure 2 shows the real part of the vertical component of the acoustic wave number as a function of ocean surface wave number (upper panel) and acoustic wave number (lower panel).

The wave number solution space for the surface wave velocity corresponds to two waves propagating in almost parallel but opposite directions. However, the acoustic solution space is isotropic, which implies that even a very directional surface wave field can generate infrasonic waves along all azimuths. This isotropic acoustic radiation pattern helps explain the pervasiveness of the microbarom signals. When ocean waves propagate exactly against each other at the same frequency, the nonlinear interaction produces a piston-like displacement of the ocean surface, and launches sound straight up to the atmosphere. Maximum acoustic energy is radiated in the vertical direction, and although it may contribute to the atmosphere's heating (Rind, 1977), this energy is lost to space and cannot be recorded by ground-based stations. Infrasound arrays would only record microbarom signals that are launched close to the horizontal, corresponding to ocean waves interacting at slightly dissimilar frequencies and slightly off the anti-parallel directions. Thus, only a small fraction of the total acoustic energy launched into the atmosphere by microbarom sources reaches the ground.

3. Case study: Hurricane Daniel

Approximately two months after the initiation of operations of IMS array I59US in Hawaii, Hurricane Daniel formed in the eastern Pacific and steadily moved towards Hawaii. Figure 3 shows the track history of Daniel, and the arrival azimuth of infrasonic signals detected by I59US, also referred to as KONA. All microbarom detections were computed using the PMCC method described in Garces and Hetzer (2002). We see that infrasonic detection of Daniel started before it was designated a hurricane (Figure 3, red), and the detected azimuth matches the actual azimuth of Daniel up to August 1, when Daniel began to dissipate. Figure 4 shows the frequency content of the microbarom signals recorded by KONA. Most of the energy is in the 0.1-0.4 Hz band, and there is a bifurcation in the microbarom band from late July 30 to early August 1. The track speed and maximum wind speed of Daniel is shown in Figure 5. The frequency of the optimal detection at KONA and the range of Daniel from KONA is plotted in the upper panel of Figure 6. Using the dispersion relation for deep water ocean waves, the propagation group velocity for surface waves at the frequency of optimal detection is shown in the lower panel of Figure 6, superposed with the track velocity of Daniel. For a 10 s ocean wave period, the acoustic period will be 5 s, corresponding to a frequency of 0.2 Hz. The group velocity for a 10 s ocean wave is ~ 8m/s. As mentioned in the previous section, a prerequisite for acoustic radiation is the presence of surface waves interacting nearly anti-parallel to each other. Two scenarios in which this condition may be maintained involve (1) a storm system that is propagating faster than the group velocity of surface waves, and (2) surface waves reflected from continents or island. The lower panel of Figure 6 suggest that the initial source of microbarom generation involved the first mechanism, but the later detections involved both mechanisms. Reflections of the storm-generated ocean waves from the islands may also explain the frequency bifurcation in the spectral content of the signals, which correspond to the close proximity of Daniel after July 30.

CONCLUSIONS AND RECOMMENDATIONS

Initial work has been performed in the evaluation of the infrasonic field predicted from storm activity in the Pacific. The theoretical results are consistent with infrasonic observations of Hurricane Daniel as it approached Hawaii. Infrasound from Daniel appears to be initially generated by the interaction of ocean waves generated behind and ahead of the hurricane core as it moved faster than the propagation speed of the ocean waves. As Daniel approached Hawaii, some higher frequency infrasound may have been generated by the interaction of the direct ocean waves with reflections from the island chain. Further work is needed on quantifying the relationships between hurricane dynamics, surface ocean wave generation, and infrasound generation.

REFERENCES

Arendt, S., and D. Fritts (2000). Acoustic radiation by ocean surface waves. *J. Fluid Mech*, **415**, 1-21.

Garces, M., and C. Hetzer (2002). Evaluation of infrasonic detection algorithms. This volume.

Kibblewhite, A., and Cheng Y. Wu (1996). Wave interactions as a seismo-acoustic source. Lecture Notes in Earth Sciences, Springer-Verlag, Berlin.

Rind, D. (1977). Heating of the lower thermosphere by the dissipation of acoustic waves. *J. Atmospheric and Terrestrial Physics*, **39**, 445-456.
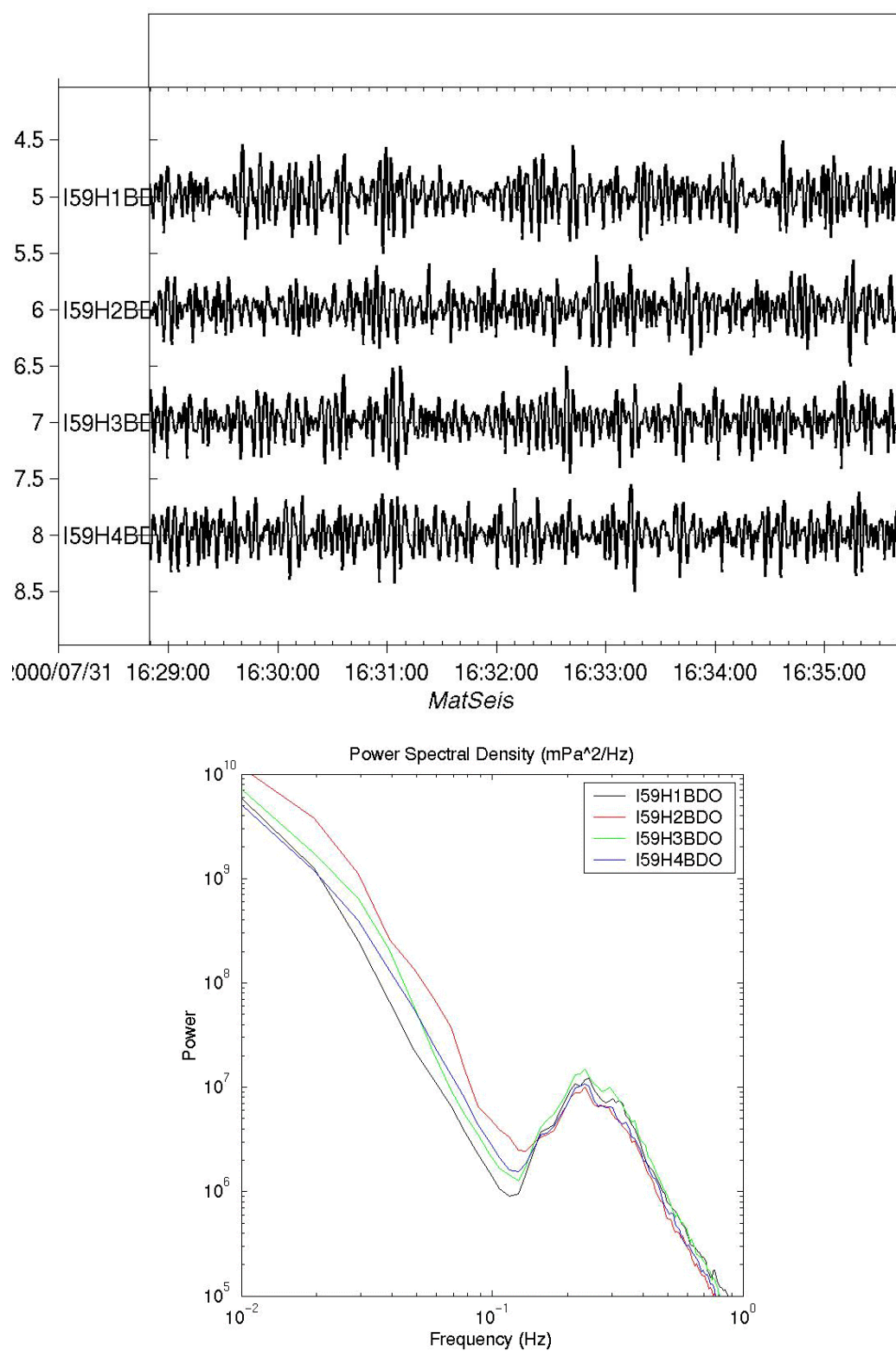
Figure 1. Example of microbarom signals recorded in Hawaii on July 31, 2000, and power spectral density for the same time period.
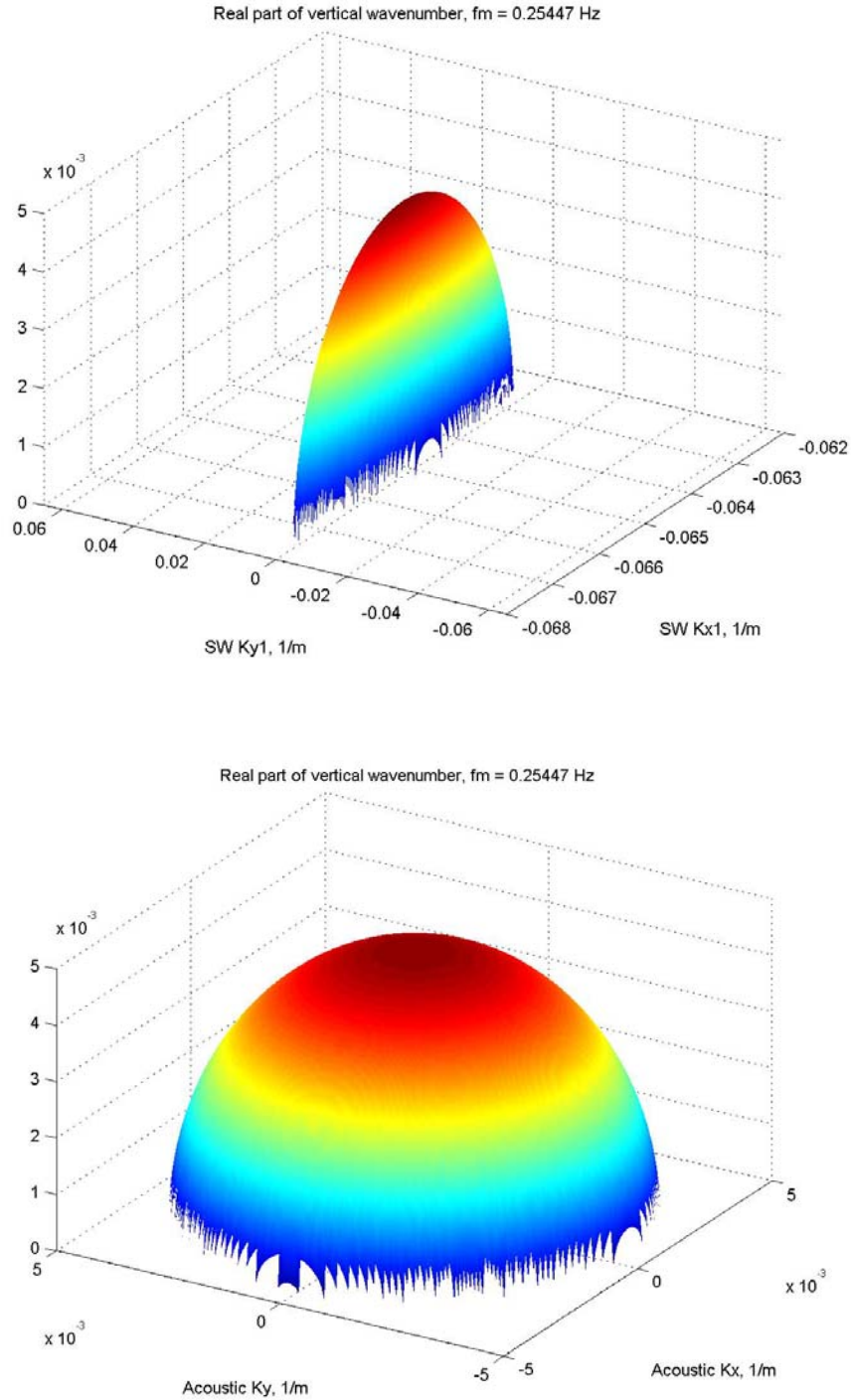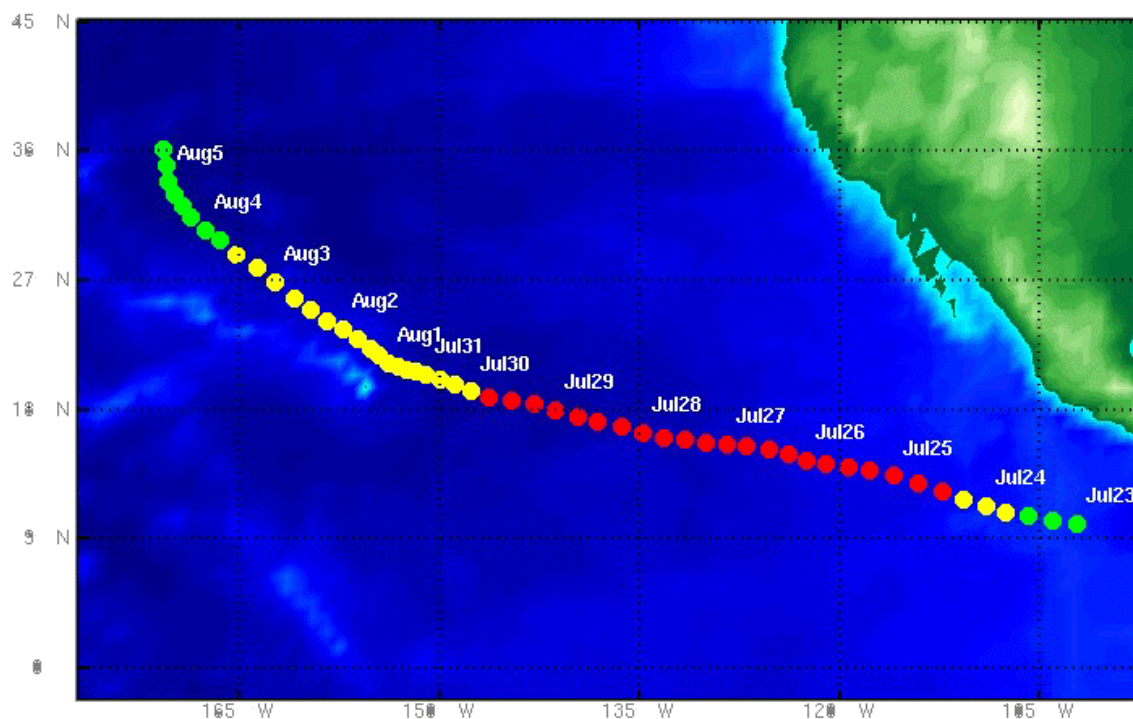
Figure 2. Real part of the vertical wave number of the acoustic solution of Arendt and Fritz (2000) for a surface wave period of ~8 s propagating along the horizontal direction (ky = 0, kx>0) and interacting with a second ocean wave of arbitrary direction. The upper panel shows the acoustic solution only exists for a small range of ocean wave numbers corresponding to the second surface wave propagating nearly anti-parallel (ky << kx, kx <0) to the first wave. The lower panel shows the real part of the acoustic vertical wave number as a function of the horizontal wave number, illustrating the isotropic nature of the acoustic radiation pattern.

Figure 3. Track of Daniel (upper panel) and observed infrasonic arrival azimuth (lower panel), measured clockwise from N, for microbarom signals observed in KONA for the same period. The red line in the lower panel marks the azimuth from Hawaii to Daniel's core.
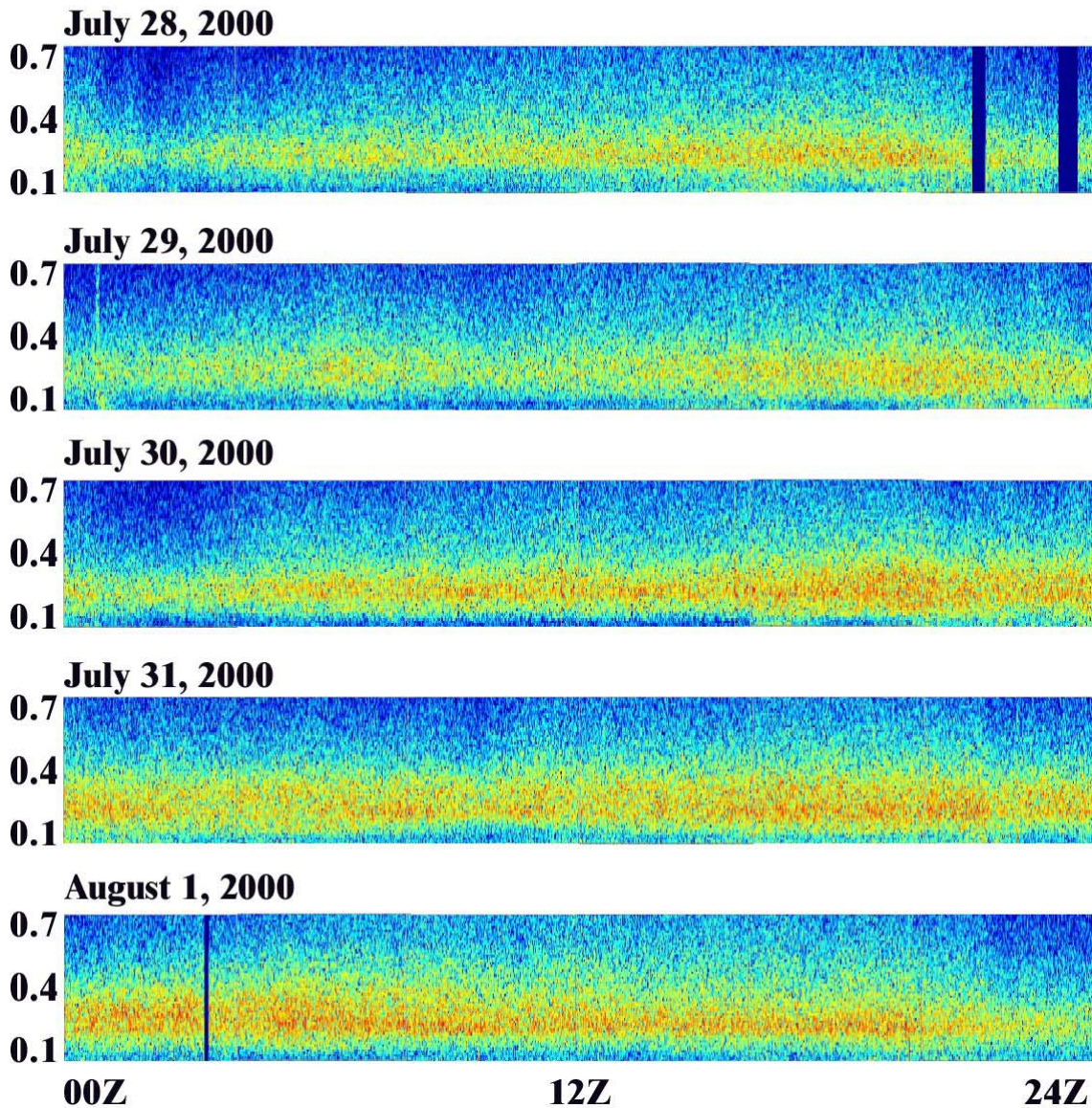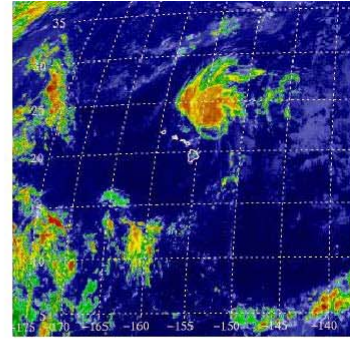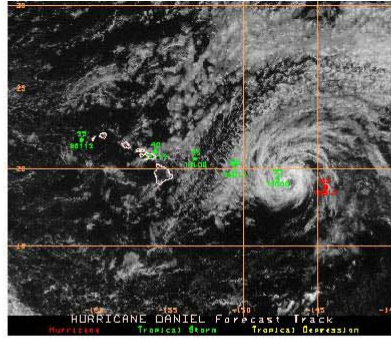
Figure 4. Spectrograms in the microbarom range for Daniel, showing initial diurnal fluctuations in the microbarom levels, which disappear as Daniel approached Hawaii. Note the frequency bifurcation starting after 12Z on July 30 and ending around 12Z on August 1.
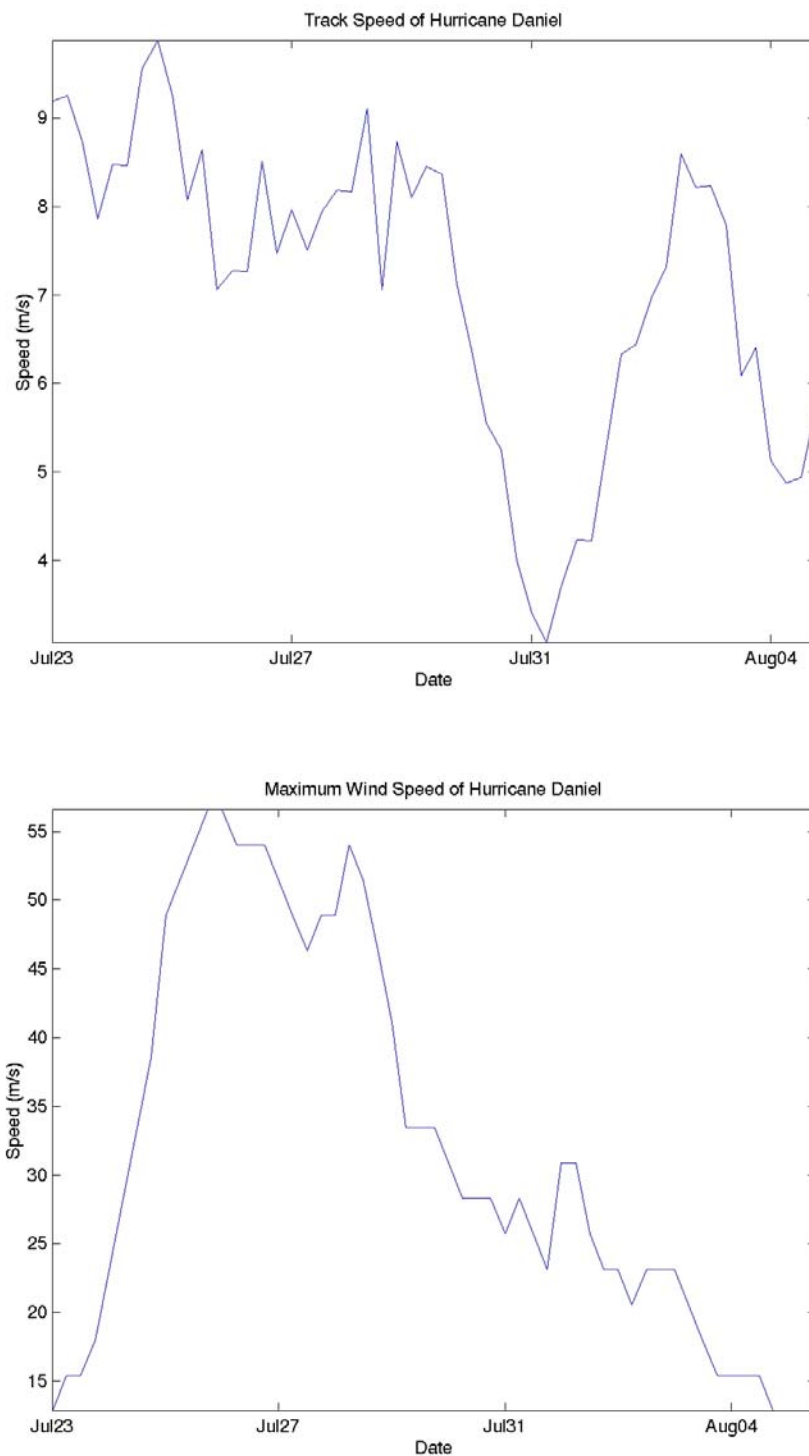
Figure 5. Track speed and maximum wind speed for Daniel.

Median Frequency of Signals from Hurricane Daniel

Track Speed and Group Velocity of Surface Waves from Hurricane Daniel
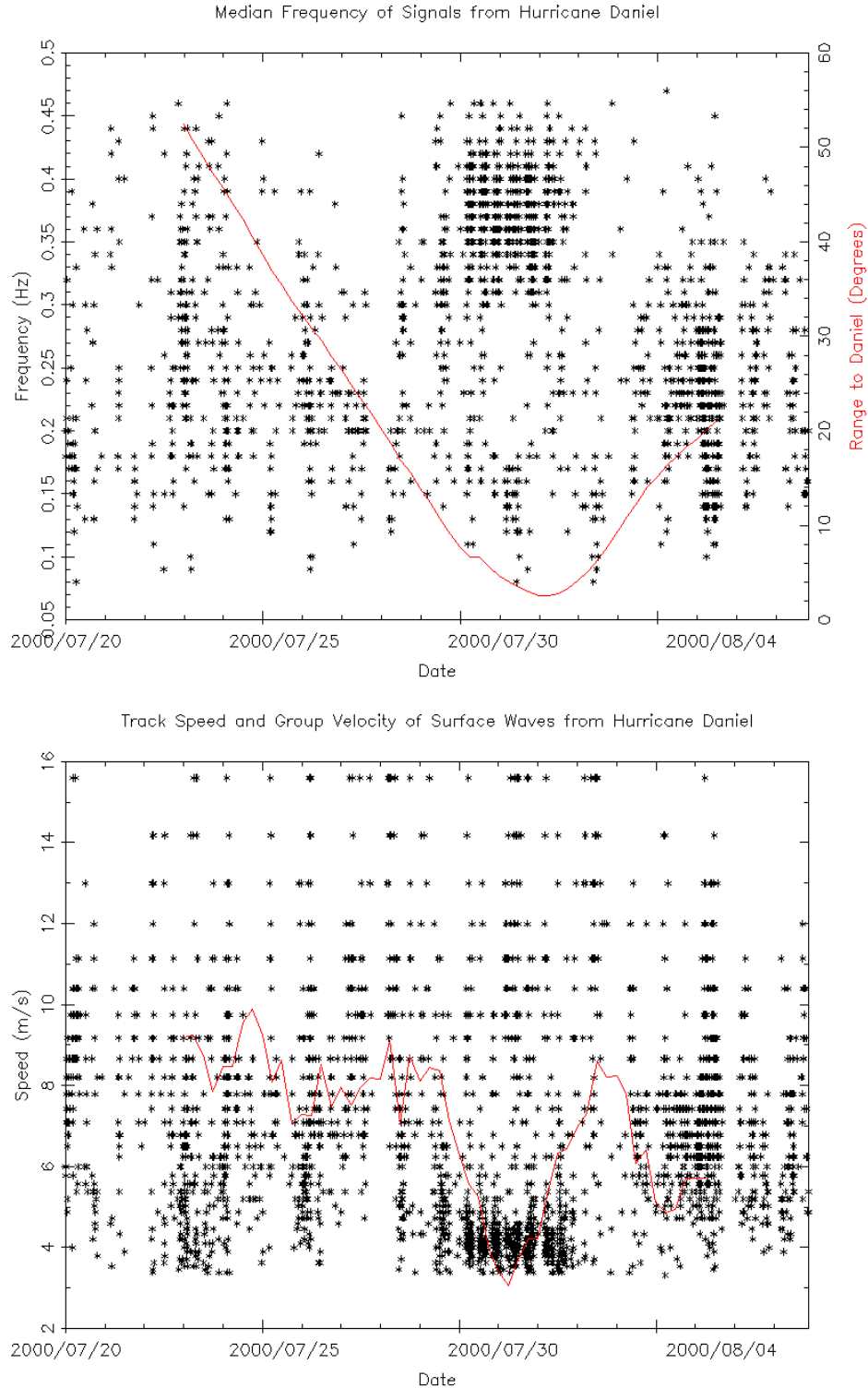
Figure 6. The upper panel shows the median frequency of peak detection and the range from KONA to the core of Daniel, and the lower panel shows Daniel's track speed (as in Figure 4) and the group velocity of surface waves corresponding to the acoustic median frequency. The track speed of Daniel exceeded the mean group velocity of the ocean waves up to the end of July 30, when Daniel is sufficiently close to Hawaii. From July 31-August 2, higher-frequency energy dominates, possibly due to the closer proximity of Daniel and the reflection of ocean waves from the island chain.

INTEGRATION OF NEAR-REAL-TIME ATMOSPHERIC MODELS WITH INFRAMAP AND APPLICATIONS TO MODELING INFRASOUND FROM ROCKETS

Robert G. Gibson and David E. Norris

BBN Technologies

ABSTRACT

The accuracy of infrasound propagation modeling depends on the fidelity of the environmental characterization. The analysis tool kit InfraMAP (*Infra*sound *M*odeling of *A*tmospheric *P*ropagation) utilizes the empirical environmental models MSISE and HWM to model temperature and wind, respectively. Opportunities for improved specification of the propagation environment are discussed. Of particular interest is the incorporation of near-real-time atmospheric updates, such as numerical weather prediction models or *in situ* radiosonde measurements, to supplement climatological characterization of the environment.

Approaches to integrating the output of meteorological synoptic models with infrasound propagation modeling codes are under development. Prognostic models such as the Navy Operational Global Atmospheric Prediction System (NOGAPS) provide near-real-time, global grids of temperature and wind over three spatial dimensions. To propagate three-dimensional rays through gridded data, wind and temperature values and their spatial derivatives must be estimated at each point along a ray path. Because ray models are highly sensitive to sharp changes in sound speed, the estimation approach must avoid introducing gradient variability that is not inherent in the original data grid. A natural cubic spline algorithm is being developed to interpolate data for use with ray modeling.

Validation efforts are essential to build confidence in the modeling procedures and are used to assess the value of potential improvements to the atmospheric specification. Observed infrasound events with known ground truth represent valuable sources of opportunity for use in validating propagation modeling techniques. Infrasound signals have been observed at several infrasound arrays in North America following launches of the space shuttle and of other large rockets. InfraMAP has been used to model propagation of infrasound originating from shuttle launches. The moving vehicle is modeled as a series of discrete infrasound sources separated in space and time. Launch ascent trajectory models are used to estimate source locations of the orbiter and solid rocket boosters during flight. Predictions of infrasound arrival times and azimuths resulting from three-dimensional ray tracing through empirical environmental characterizations are compared with observed data.

OBJECTIVES

The primary objective of this research effort is development of an enhanced InfraMAP software tool kit that enables higher fidelity infrasound propagation modeling by making use of linkages to near-real-time atmospheric characterizations. This effort is intended to support improved event localization and phase identification. An extensive validation effort is also being undertaken, using a diverse set of observations and ground truth, in order to improve confidence in the modeling techniques and provide calibration in support of operational needs. Anticipated uses of the software include: in-depth analysis of events and scenarios of particular monitoring interest; sensitivity analyses; and detailed infrasound localization and detection studies.

RESEARCH ACCOMPLISHED

Near-real-time environmental updates to InfraMAP

The InfraMAP software tool kit is composed of research-grade propagation models (3-D ray tracing, normal modes and parabolic equation) and upper-atmospheric characterizations, integrated to allow for user-friendly model execution and data visualization. InfraMAP can be applied to predict travel times, bearings, and amplitudes from potential event locations worldwide. Such predictions can be used to identify infrasound phases and to define travel-time and bearing corrections, which can improve localization performance (Gibson and Norris, 1999).

Temporal and spatial variability of the atmosphere is addressed by modeling range-dependent temperature and winds and incorporating them into the propagation models. The baseline atmospheric characterizations in InfraMAP are two empirical models: the horizontal wind model, HWM-93 (Hedin *et al.*, 1996), and the extended mass spectrometer-incoherent scatter radar temperature model, MSISE-90 (Picone *et al.*, 1997). Wind, temperature, and densities are modeled from the surface into the thermosphere and include spatial, diurnal, and seasonal effects. The models are climatological in that they predict the mean environmental profiles based on assimilation of multiple years of data. The HWM and MSISE models were chosen for use in InfraMAP due to their high fidelity over a wide range of altitudes and temporal scales, their global domain, and the relative ease of software integration. Validation studies conducted to date using InfraMAP with the HWM-93 and MSISE-90 characterizations indicate generally good agreement between modeled propagation paths and infrasound measurements. However, there exist cases in which measured infrasound phases are not adequately predicted using the baseline InfraMAP.

Global climatological models such as HWM and MSISE that are based solely on historical data do not capture local temporal and spatial atmospheric structure. The ability to add near-real-time sources of information will significantly improve the estimate of the infrasound propagation environment. Classes of near-real-time atmospheric updates include:
o   *in situ* observations, such as measured profiles from radiosondes, and
o   physics-based synoptic models that assimilate observations from a number of sources.

Models generally produce gridded output, whereas observed profiles (e.g., radiosondes) are not gridded; i.e., the observations are not uniformly sampled geographically or in altitude. However, none of the updated sources of data provide the complete set of temperature and wind speed profile information needed for infrasound modeling. In particular, most available data pertain to altitudes less than approximately 35 km, whereas propagation modeling requires information well into the thermosphere (approx. 120 km).

Therefore, empirical atmospheric models remain an essential tool for estimating the environment, particularly at high altitudes. Supplementing the climatological models with available near-real-time updates is likely to yield improved infrasound predictions, particularly for propagation paths that dwell primarily in the lower and middle atmosphere, where updated data are more readily available. The incorporation of updated atmospheric information, in the form of synoptic models or *in situ* measurements, will allow estimates of the propagation environment to be improved over the baseline climatology. Furthermore, it is desired to increase the capability of the InfraMAP software by offering greater flexibility in the range of data sources that can be accommodated.

Investigations have begun into the improvements attainable in propagation modeling by incorporating near-real-time atmospheric updates. The first steps are to develop links to near-real-time atmospheric observations or grids and to import the files for use in InfraMAP in conjunction with the HWM and MSISE empirical characterizations.

Based on the early success of empirical models at defining the propagation environment in the baseline InfraMAP software, automated integration of *in situ* data sources with propagation models has so far been determined not to be a high priority. However, the software provides a capability to incorporate updated atmospheric profiles, for purposes of evaluating potential improvements in propagation modeling. InfraMAP currently provides an option for user-defined atmospheric profiles for range-independent propagation modeling. Thus, updated wind and temperature data, such as from radiosonde observations, can be incorporated with the propagation models. Radiosonde observations are currently available twice a day from over a thousand weather stations worldwide. However, many regions of the world, particularly in the southern hemisphere, do not have dense radiosonde coverage. Available measurements consist of temperature, wind speed and direction from the ground up to approximately 35-km altitude (10-mb atmospheric pressure). Examples of observed temperatures from several radiosondes in the southwestern US on 23 April 2001, corresponding to observation of the Pacific bolide, are presented along with corresponding MSISE-90 characterizations in Figure 1. Observed zonal and meridional winds for the same radiosondes are shown along with corresponding HWM-93 characterizations in Figure 2.
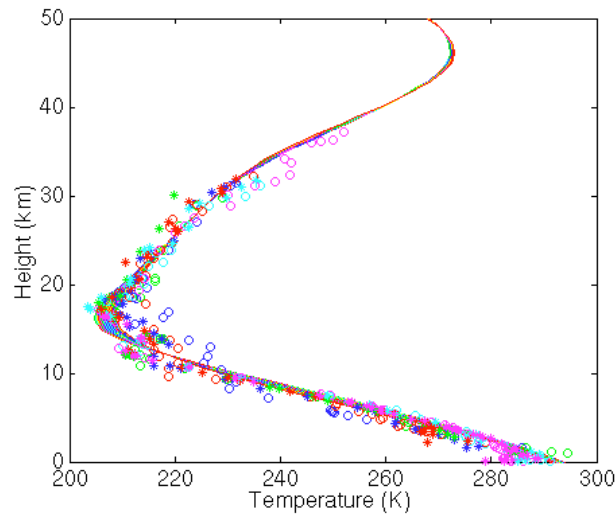
Figure 1. Radiosonde observations of temperature in the southwestern US on 23 April 2001 (shown as symbols) and corresponding MSISE-90 characterizations (shown as lines).
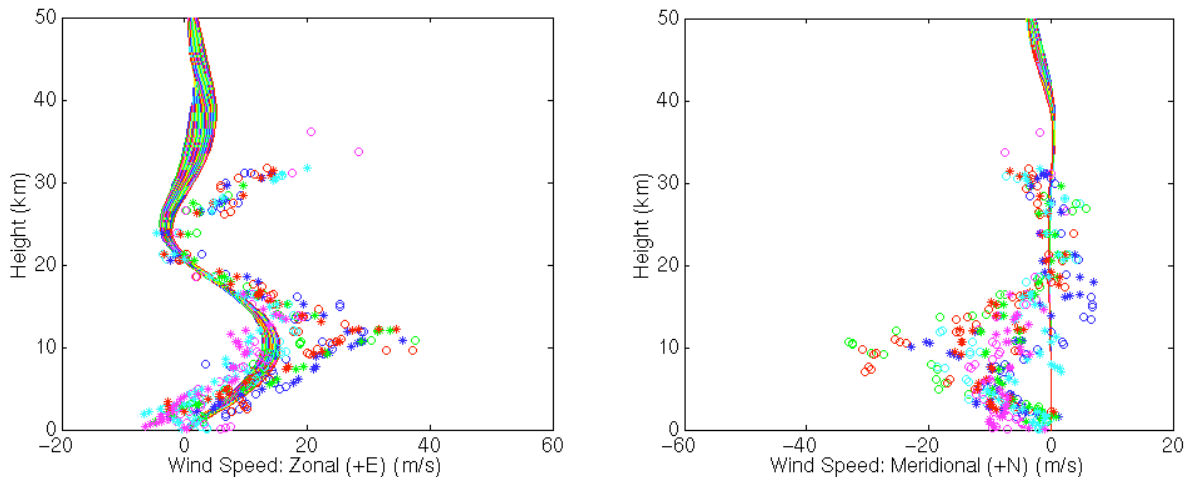

Figure 2. Radiosonde observations of zonal wind (left) and meridional wind (right) in the southwestern US on 23 April 2001 (shown as symbols) and corresponding HWM-93 characterizations (shown as lines).

In this instance, observed temperatures are well represented by the climatological model. The model of mean wind does not capture all of the features of the radiosonde wind observations, particularly the magnitude of the jet stream at approximately 10 km.

Prognostic models such as the Navy Operational Global Atmospheric Prediction System (NOGAPS) provide near-real-time, global grids of temperature and wind over three spatial dimensions. NOGAPS, originated by the Navy's Fleet Numerical Meteorology and Oceanography Center (FNMOC), is a numerical weather prediction model that utilizes not only profiles measured by radiosondes, but also an extensive data set of ship-based, land-based and satellite measurements to provide gridded temperature and wind speed at a range of altitudes. NOGAPS is a promising environmental model for use with infrasound propagation models due to its global domain and relatively high altitude coverage. The NOGAPS integration domain is from the ground to the 1-mb pressure surface (approximately 50 km), and output data are readily available up to the 10-mb pressure surface (approx. 30-35 km). Output products from NOGAPS have been obtained and decoded for purposes of integration and testing.

An example of a subset of gridded zonal wind profiles from NOGAPS is shown in Figure 3. The profiles are for a fixed time and date at the grid points defined in a 7.7 degree by 6.5 degree region over the southwestern US. These are compared to HWM-93 model output, over the same region, date and time. Mean zonal winds in the region are well predicted by the climatological model, but greater variability is shown in the NOGAPS model output.
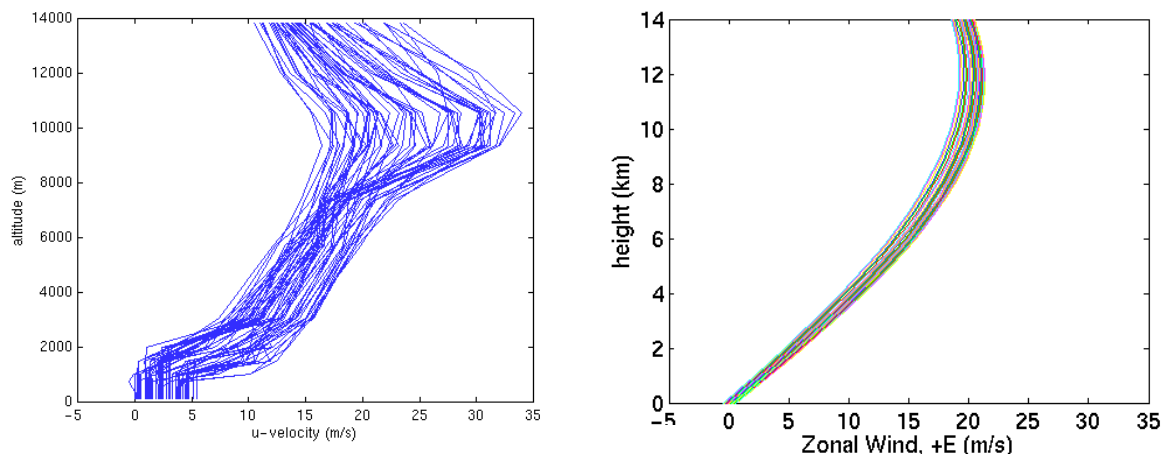

Figure 3. Predictions of zonal wind over a region in the southwestern US using NOGAPS (left) and HWM-93 (right).

Propagation models in InfraMAP interface with environmental characterizations in three ways:
o   Range dependent, using the empirical atmospheric model functions to determine the environment at each step;
o   Range independent, using average profiles determined from the empirical models evaluated along the propagation path;
o   Range independent, using user-defined profiles.

In order to accommodate an environment defined by a gridded database such as NOGAPS, modifications must be made to InfraMAP's interface between propagation and environmental software modules, particularly in order to allow range dependence. There are a number of technical issues to be addressed, including: interpolation and extrapolation techniques; formation of consistent, repeatable representations; and evaluation of prediction sensitivity to interpolation methods. To propagate three-dimensional rays through gridded data, wind and temperature values and their spatial derivatives must be estimated at each point along a ray path. Because ray models are highly sensitive to sharp changes in sound speed, the estimation approach must avoid introducing gradient variability that is not inherent in the original data grid. A natural cubic spline algorithm is being developed to interpolate data for use with ray modeling. Cubic spline interpolation provides a smooth first derivative and continuous second derivative, ensuring compatibility with the ray model. Algorithms are currently being tested for integration into InfraMAP.

The enhanced InfraMAP capabilities that are being developed in this effort are shown schematically in Figure 4. The baseline InfraMAP functionality is shown in light gray, the capabilities that are currently being developed in a

separate effort (Norris and Gibson, 2002) are shown in dark gray, and the new components under development in this effort are shown in blue.
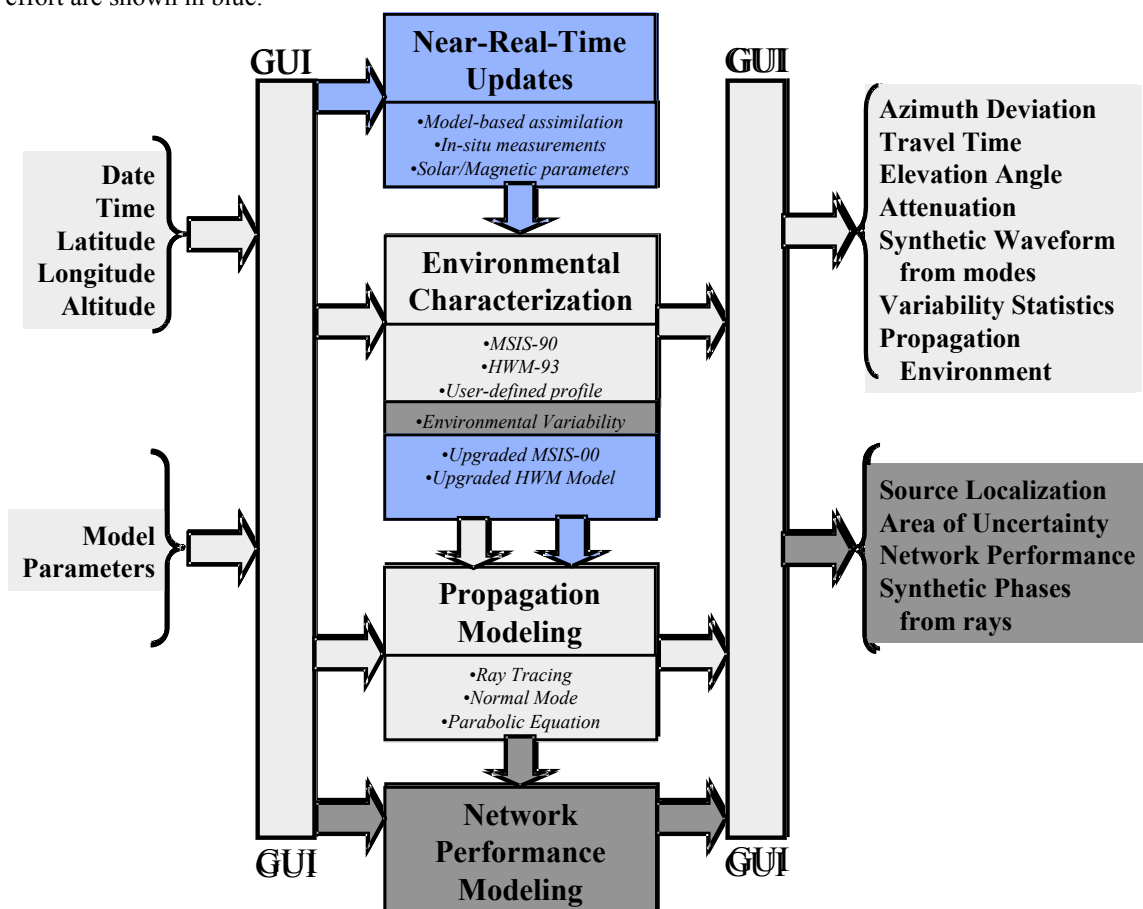

Figure 4. Schematic representation of InfraMAP functionality, with capabilities being developed in this effort shown in blue.

Model validation using infrasound from rocket launches

Validation efforts are essential to build confidence in the modeling procedures and to identify areas where further refinements are required. Where ground truth is available, validation results support event localization, phase identification and calibration efforts.

Rocket launches may serve as useful ground truth data for infrasound (McLaughlin *et al.*, 2000) and also represent an excellent source of opportunity for model validation. Space shuttle launches from Cape Kennedy, Florida, have recently been observed at infrasound arrays at Los Alamos, New Mexico, (DLIAR prototype array) and at Lac du Bonnet, Canada (IS10 array). Rocket and missile launches from the eastern US were observed extensively in the 1960's and 1970's by infrasound arrays at Palisades, New York, and elsewhere, and Balachandran and Donn (1971) and other scientists at Lamont-Doherty Geological Observatory and the US Army Electronics Command issued a series of reports. A number of important findings resulted from this early work, including identification of two distinct source regions, one near the launch site and one near the re-entry location of the first stage.

Trajectories for specific shuttle missions have been modeled using actual launch parameters. Trajectories for the shuttle's solid rocket boosters, which are released from the orbiter approximately two minutes into the ascent, have also been estimated. Modeled trajectories for two observed shuttle missions, STS-96 (27 May 1999) and STS-93 (23 July 1999) are shown in Figure 5. Launch ascent trajectories for a typical mission of shuttle orbiter and solid rocket boosters (SRB) are shown in Figure 6.
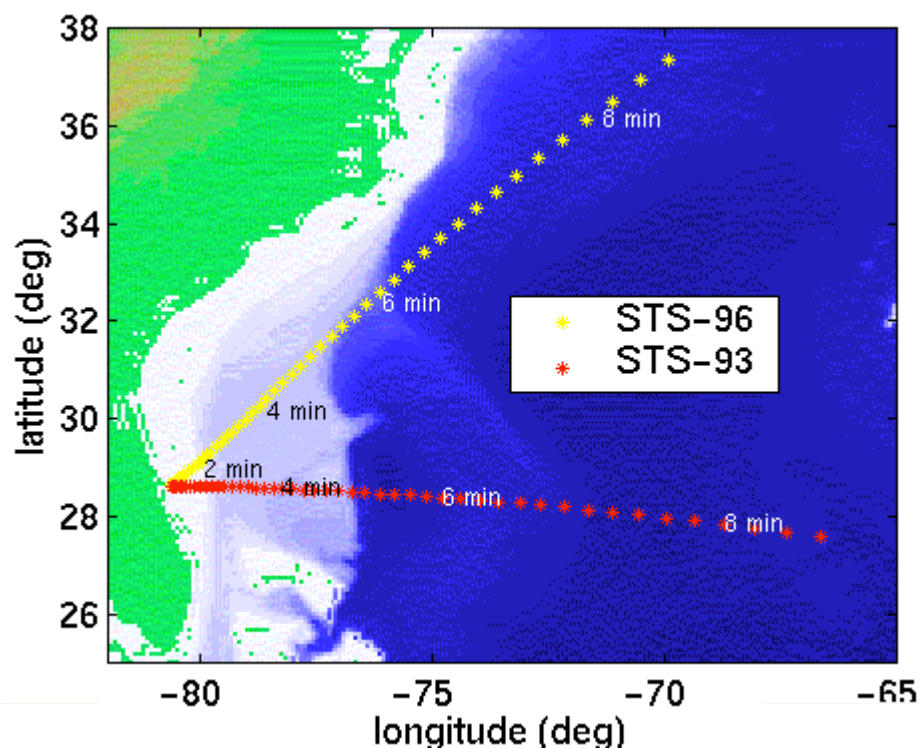
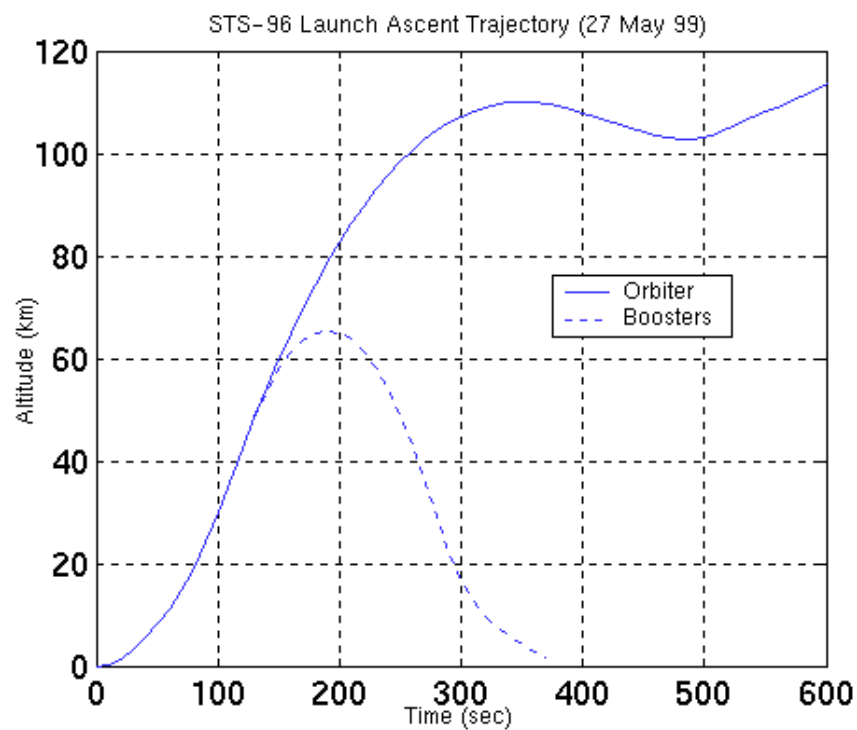**Figure 5: Space shuttle trajectories for two missions.**

Figure 6: Space shuttle orbiter and solid rocket booster trajectories.

InfraMAP was used to determine eigenrays to DLIAR from points along the STS-96 trajectory, with HWM-93 and MSISE-90 used for environmental characterization. The continuously moving source was modeled as a series of discrete sources separated in space and time. A source was modeled every 10 seconds from the launch time out to 5 minutes after launch for the orbiter and from 200 seconds out to 6 minutes after launch for the solid rocket boosters. For each eigenray, an arrival azimuth and an arrival time (referenced to the launch time) were determined. Results are shown in Figure 7. Stratospheric rays and thermospheric rays are depicted separately for both the orbiter and the SRB. Also shown in the figure (as red asterisks) are results from the observation at DLIAR, determined by analysis using the InfraTool component of the MatSeis software package (Harris and Young, 1996).
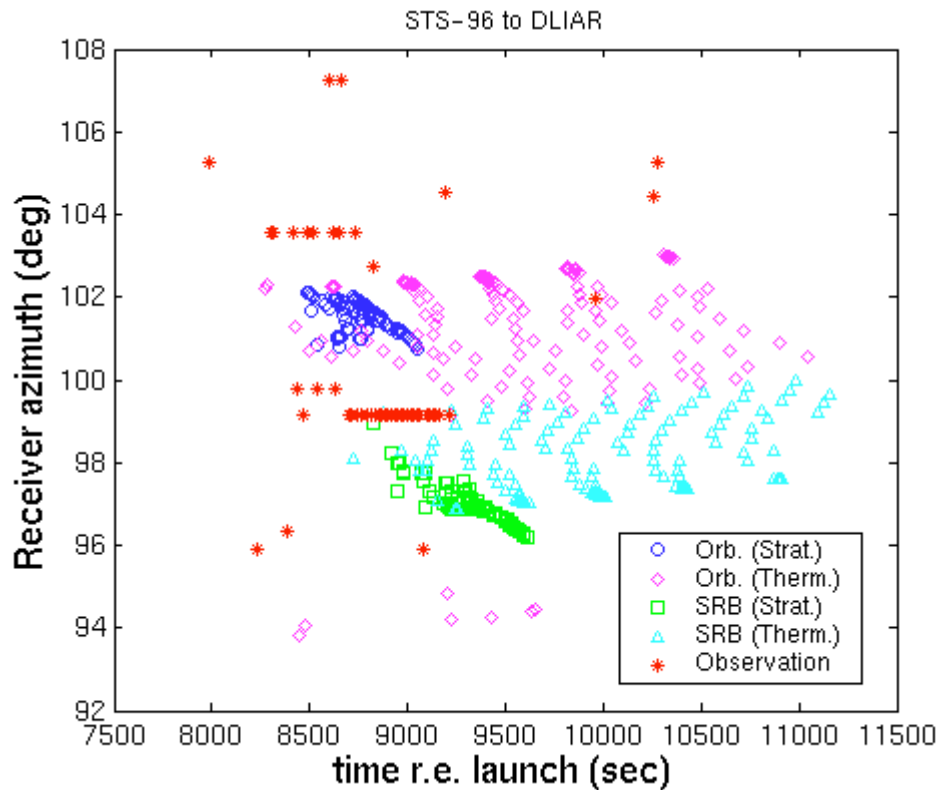
Figure 7: Predicted and observed infrasound arrivals from STS-96 to DLIAR.

The two primary observed arrivals (at approximately 103.5 and 99 degrees) are reasonably well modeled by the stratospheric rays from the orbiter (blue circles) and boosters (green squares), respectively. However, a bias in azimuth of approximately 2 degrees can be seen for both primary arrivals. Further modeling of the launch event using an updated atmospheric characterization, in order to see if travel-time and azimuth predictions could be improved, is of interest in this case.

Further investigation into this and other rocket launches, such as those of the Titan IVB, is underway. Data have been collected and trajectories modeled for several missions from 1998 to the present. Trends of observability, arrival time, and azimuth are being analyzed. Propagation model results are compared with observations and biases quantified. Several technical issues are of interest during this study, including:

o   The modeling improvements achievable with near-real-time updates as compared to HWM and MSISE;
o   Further understanding of the infrasound source mechanism in order to identify the regions of the trajectory (altitude, velocity, etc.) that contribute most strongly to observed signals;
o   Quantifying attenuation along the ray paths to support identification of observed phases;
o   The use of propagation modeling to predict observability of events.

The results of the analyses will serve to validate the environmental and propagation modeling techniques.

CONCLUSIONS AND RECOMMENDATIONS

The InfraMAP tool kit is used to predict the critical propagation characteristics that affect infrasound localization and detection. Adequate atmospheric characterization is necessary to correct for biases in travel time and azimuth that result from the propagation environment in order to avoid large location errors. *In situ* observations of winds and temperature can be used in InfraMAP for range-independent propagation modeling. Techniques are being developed to integrate output from the NOGAPS numerical weather prediction model with range-dependent propagation models. InfraMAP's integrated set of models will allow for higher fidelity propagation modeling than has previously been available to the infrasound monitoring community. As new high-fidelity environmental characterizations become available, they should be considered for integration into an enhanced version of the InfraMAP software.

Rocket launches generate infrasound signals for use in model validation studies. Infrasound is generated by both rocket ascent and booster descent. Launch trajectory models provide useful approximations of ground truth for use in conjunction with propagation modeling. Comparisons of measured and modeled arrival times and azimuths suggest that baseline infrasound modeling techniques are good but that higher fidelity would likely be obtained with the use of near-real-time wind and temperature characterizations. Further modeling of a large set of observed events, using updated atmospheric characterizations, is recommended in order to quantify the improvements in travel-time and azimuth predictions that are achievable.

REFERENCES

Balachandran, N. and W. Donn (1971), Characteristics of infrasonic signals from rockets, *Geophys. J. R. Astr. Soc*., **26**, 135-148.

Gibson, R. and D. Norris (1999), Development of an Infrasound Propagation Modeling Tool Kit, DTRA-TR-99-47.

Harris, J. M. and C. J. Young (1996), MatSeis: A Seismic Toolbox for MATLAB, *Proceedings of the 18th Annual Seismic Research Symposium on Monitoring a Comprehensive Test Ban Treaty*, Phillips Laboratory (7/96).

Hedin, A. E, E. L. Fleming, A. H. Manson, F. J. Schmidlin, S. K. Avery, R. R. Clark, S. J. Franke, G. J. Fraser, T. Tsuda, F. Vial, and R. A. Vincent (1996), Empirical wind model for the upper, middle, and lower atmosphere, *J. Atmos. Terr. Phys*., **58**, 1421-1447.

McLaughlin, K. L., A. Gault, and D. Brown (2000), Infrasound detection of rocket launches, *Proceedings of the 22nd Annual DoD/DOE Seismic Research Symposium: Planning for Verification of and Compliance with the Comprehensive Nuclear-Test-Ban Treaty (CTBT)*, New Orleans.

Norris, D. E. and R. G. Gibson (2002), InfraMAP enhancements: environmental/propagation variability and localization accuracy of infrasonic networks, in this volume.

Picone, J. M., A. E. Hedin, S. L. Coffey, J. Lean, D. P. Drob, H. Neal, D. J. Melendez-Alvira, R. R. Meier, and J. T. Mariska (1997), The Naval Research Laboratory program on empirical models of the neutral upper atmosphere, in *Astrodynamics: Advances in the Astronautical Sciences*, Vol. 97, edited by F. R. Hoots, B. Kaufman, P. J. Cefola, and D. B. Spencer, American Astronautical Society, San Diego, Ca.

EXPERIMENTS WITH INFRASONIC NOISE-REDUCING SPATIAL FILTERS

Michael A.H. Hedlin and Jon Berger

Scripps Institution of Oceanography; University of California, San Diego

ABSTRACT

As development of the International Monitoring System (IMS) infrasound network progresses, there remains much to learn about reducing noise due to atmospheric turbulence while preserving signals from distant sources. The spatial filter currently preferred for use at new IMS infrasound array sites consists of an array of low-impedance inlets connected by solid tubes to a microbarometer. Acoustic signals and noise enter the "rosette" pipe system via the inlets and are summed in manifolds or at the sensor. Acoustic energy that is incoherent at wavelengths less than the aperture of the filter is attenuated, and the ratio of coherent signal to incoherent noise is increased. We have tested two designs of rosette filters that span 18 and 70 meters to estimate the signal-to-noise ratio (SNR) gain as a function of wind speed and to look for artifacts of the filtering process. Empirical observations compare well with theoretical predictions. The 70-m filter provides noise reduction of up to 20 dB over a band from 0.02 Hz to 0.7 Hz. The 18-m filter does not suppress noise below ~ 0.2 Hz. The corner frequency of both spatial filters scales directly with wind speed. Resonance is observed in data from both filters but is most pronounced in data from the 70-m filter. Modeling of data from both filters clearly indicates that the reflections occur at all points inside the filters at which the impedance changes. Although a large impedance change occurs at the low-impedance inlets, the resonance that is first observed at 0.7 Hz in data from the 70-m filter, and at 3 Hz in data from the 18-m filters occurs between the primary and secondary summing manifolds. Experiments show that this resonance can be largely, or entirely, removed by installing impedance matching capillaries adjacent to the secondary summing manifolds in the pipes leading to the primary summing manifold. Adding capillaries at the inlets is less effective as those points are linked with high-frequency resonance at the upper limit, or beyond, the passband of interest to the monitoring community.

Rosette filters are tuned to vertically incident energy. Energy arriving at other incidence angles is not summed in phase. The problem is acute at high frequencies, at near-horizontal arrival angles, and scales directly with the aperture of the filter. Total cancellation of the horizontally propagating signals recorded via the 70-m rosette filter is predicted to occur at 5 Hz. Recordings of a large bolide that exploded west of the infrasound test bed in southern California on April 23, 2001, were made by co-located reference systems and the large and small rosette filters. The data validate the phase and amplitude response predicted by a theory that takes into account the resonance of energy inside the filters and the phase delays of the energy entering the filters.

This paper will report these results and our experiments with noise reducing barriers.

OBJECTIVE

Our objective is to build, model and test infrasonic noise reduction systems to assess the utility of the different devices as a function of frequency and wind speed. Our goal is to test systems that are being deployed at International Monitoring System (IMS) array sites and to test new devices (such as the new fiber optic sensor under development at the University of California San Diego [UCSD], Zumberge et al., 2002) and spatially compact filters (such as the wind barrier, a sensor buried at a shallow depth in a porous medium) in our search for systems that are more economical, require less space, or have a better response than currently preferred designs. We identify shortcomings of filters (e.g. resonance in large pipe filters) and search for ways to improve the filters.

RESEARCH ACCOMPLISHED

Preliminary evaluation of rosette filters

We have conducted tests of rosette infrasonic noise-reducing spatial filters (Alcoverro, 1998) at the Pinon Flat Observatory in southern California (Figure 1; Hedlin et al., 2002). Data from 18- and 70-m-aperture rosette filters (Figure 2) and a reference port have been used to gauge the reduction in atmospheric wind-generated noise levels provided by the filters and to examine the effect of these spatial filters on spatially coherent acoustic signals in the 0.02- to 10-Hz band. At wind speeds up to 5.5 m/s, the 18-m rosette filter reduces wind noise levels above 0.2 Hz by 15 to 20 dB. Under the same conditions, the 70-m rosette filter provides noise reduction of up to 15 to 20 dB between 0.02 and 0.7 Hz. Standing wave resonance inside the 70-m filter degrades the reception of acoustic signals above 0.7 Hz. The fundamental mode of the resonance, 15 dB above background, is centered at 2.65 Hz and the first odd harmonic is observed at 7.95 Hz in data from the large filter (Alcoverro and LePichon, 2002; Hedlin et al., 2002). Synthetics accurately reproduce the noise reduction and resonance observed in the 70-m filter at all wind speeds above 1.25 m/s (Figures 3 and 4). Resonance theory indicates that internal reflections, which give rise to the resonance observed in the passband, are occurring at the summing manifolds, and not at the inlets. Rosette filters are tuned to acoustic arrivals with infinite phase velocity. Attenuation of signals by the 70-m rosette filter at frequencies above 3.5 Hz arriving at grazing angles of less than 15° from the horizontal are predicted to range upward from 10 dB to total cancellation at 5 Hz (Figure 5). Theoretical predictions of the phase and amplitude response of 18- and 70-m rosette filters that take into account internal resonance and time delays between the inlets compare favorably with observations derived from a cross-spectral analysis of signals from the explosion of a large bolide (Figure 6).

Experiments with impedance-matching capillaries

We have conducted three experiments with impedance-matching capillaries to remove the problem with resonance in the rosette spatial filters (Hedlin and Alcoverro, 2002). In the first test, we sought confirmation that the reflections that give rise to the resonance peaks observed at 2.65 and 7.95 Hz in the data from the 70-m rosette filters are occurring at the secondary summing manifolds, and not at the inlets. We constructed three filters that consist of 8- to 27-m-long pipes. We fitted the open ends of the pipes with different capillaries to assess the utility of acoustic resistance for removing the resonance problem. The test reproduced the resonance peaks and confirmed that the reflections that give rise to the spectral peak at 2.65 Hz occur at the primary and secondary summing manifolds. The test, and subsequent modeling, also confirmed that the resonance peaks could be completely removed by installing capillaries at the inlets of these simplified filters. The appropriate acoustic resistance of each capillary is the characteristic impedance of the pipe that connects the inlet with the primary summing manifold. Modeling also confirms that the same capillaries will remove the resonance problem in the complete rosette filters. Installing eight capillaries adjacent to the secondary summing manifolds in the pipes leading to the primary manifold will be far more effective than installing the capillaries at the 144 inlets (Figure 7). Data collected from a filter in the infrasound array I57US that was modified with capillaries, with acoustic resistance equal to the characteristic impedance of the 27-m pipes connecting the primary and secondary summing manifolds, revealed that the main resonance peak at 2.65 Hz is completely removed, as predicted by theory, and the first sign of resonance, due to resonance in the pipes between the secondary summing manifolds and the inlets, is observed at 5 Hz (Figure 8). A separate test of capillaries in the 18-m rosette filters produced similar results. All filters in the IMS infrasound array I57US have been modified with capillaries as a result of this research. Modeling indicates that a modest improvement of the response of the 70-m rosette filter can be achieved by installing capillaries at the inlets, but this

is not recommended because of the plane wave response, mentioned in the previous section, that degrades the response of these filters above 3 Hz.

Tests of noise-reducing wind barriers

This section reports empirical observations of wind speed and infrasonic noise reduction inside a wind barrier. The barrier has been compared with "rosette" spatial filters and with a reference site that uses no noise reduction system. The barrier is investigated for use at IMS infrasound array sites where spatially extensive noise-reducing systems cannot be used because of a shortage of suitable land. Wind speed inside a 2-m-high 50% porous hexagonal barrier coated with a fine wire mesh is reduced from ambient levels by 90%. If the infrasound wind noise level reductions are all plotted versus the reduced frequency given by $f*L/v$, where L is the characteristic size of the array or barrier, f is the frequency and v is the wind speed, the reductions at different wind speeds are observed to collapse into a single curve for each wind-noise-reduction method. The reductions are minimal below a scale size of 0.3 to 1, depending on the device; then spatial averaging over the turbulence structure leads to increased reduction. Above the corner frequency, the fence reduces infrasonic noise by up to 20 to 25 dB (Figure 9). Below the corner frequency the barrier displays a small reduction of about 4 dB. The rosettes display no reduction below the corner frequency. One other advantage of the wind barrier over rosette spatial filters is that the signal recorded inside the barrier enters the microbarometer from free air and is not integrated, possibly out of phase, after propagation through a system of narrow pipes.

CONCLUSIONS AND RECOMMENDATIONS

Rosette filters

We have found that modeling theory, which takes into account reflection and attenuation of acoustic energy in the rosette filters and includes the response of the microbarometer, accurately reproduces recorded data. We have also determined that impedance matching capillaries, installed at the secondary summing manifolds, will remove the resonance problem. We have noted that the rosette filters are tuned to vertically incident acoustic waves and the reception of signals that arrive within 15° of the horizontal is limited. The plane wave response is most significant in the large, 70-m-aperture rosette filter.

We recommend that all rosette filters used at IMS infrasound arrays are modified as described in the earlier section.

Future research with rosette filters

The theory that accounts for internal resonance and external phase delays can be applied to any rosette filter design and therefore, in principle, can be used to search for better designs. This could be accomplished by defining optimization criteria (e.g. lack of resonance peaks in the band below 10 Hz; flat plane wave response in the same band) and systematically searching for designs that optimally satisfy these criteria. It remains to be determined if the combined theory can be used to correct the amplitude and phase of signals filtered through rosette filters.

Real rosette filters do not adhere perfectly to the specified designs shown in Figure 2. Most sites present obstacles that require some modifications to the placement of the inlets in the rosette clusters. Most sites are not perfectly horizontal but are tilted. An important question that we can now begin to address is what the rosette filters do to the overall performance of an infrasound array. What asymmetries in the placement of the inlets and what tilts at the different elements can exist before unacceptable bias will be introduced into the back-azimuth derived from processing data from all elements. If these imperfections in the locations of the inlets and in the tilts of the filters are known, this work might lead to a means to remove this bias.

Arrivals from naturally occurring infrasound sources such as bolides can be used as signals of opportunity to calibrate *in situ* the amplitude and phase response of the IMS space filters. The derived "calibration" curves can be used to help remove the system response from the recorded data. These calibration curves are a function of arrival angle (apparent phase slowness) as well as frequency so that a collection of events in various directions is required to obtain a complete set of empirically derived curves. Alternatively, one or two events can be used to validate a theory of the spatial and frequency dependence of the rosette filter response, as is done in Hedlin, Alcoverro and D'Spain (2002), so that theoretically derived calibration curves then can be applied. Changes in conditions at the

recording site can result in changes in the filter response. For example, variations in atmospheric temperature result in changes in sound speed that, in turn, cause a shift in the frequencies of the resonances and in the location of the spatial response null associated with phase delays. Likewise, a change in the number, location, and effective impedance of individual ports in a rosette filters will affect the resonance and spatial nulling characteristics. The impact of such changes on the filter response can be evaluated using the methods described in Hedlin, Alcoverro and D'Spain (2002).

Theoretical tests of capillaries are needed to determine the effect of one or more of the capillary plugs becoming partially or fully blocked by water, insects, etc., on the response of the individual filters and of the entire array. The long-term maintenance of these systems might involve periodic inspection and clearing of the capillary plugs.

Wind barriers

Comparison of the scaled reductions in wind noise produced by the rosettes and wind barrier with the reductions afforded by a spherical wind screen hold promise for significant wind-noise reduction with a smaller footprint device (Hedlin and Raspet, 2002). The rosettes only produce reductions if the scale size of the turbulence is smaller than the size of the rosette since such devices rely on the incoherence of the turbulence at each port. The wind barrier displayed large reductions only when the scale size of the turbulence is smaller than the height of the barrier. However, a small reduction of about 4 dB was realized when the scale size was larger than the barrier. This reduction may correspond to the large reductions realized by foam windscreens. In the spherical windscreens, these reductions occur since the pressure measured at the center is the area average of the pressures generated at the surface of the sphere. For large turbules, the pressure generated by an increase in wind speed is positive at the front of the sphere and negative at the back, and the average is less than the pressure measured at a bare sensor. This result holds promise that a properly designed windscreen on or near the ground surface may achieve significant reductions even for turbulence scales greater than the size of the screen.

ACKNOWLEDGEMENTS

REFERENCES

Alcoverro, B. (1998) Acoustic filters design and experimental results, Proceedings: Workshop on Infrasound, Commissariat à l'Energie Atomique, Bruyères-le-Châtel, France, July 21-24, 1998.

Alcoverro, B. and A. Le Pichon (2002) Design & optimization of a noise reducer system for infrasound measurements using elements with low acoustic impedance, submitted to *J. Acoust. Soc. Am*.

Hedlin, M.A.H., B. Alcoverro, and G. D'Spain (2002) Evaluation of rosette infrasonic noise-reducing spatial filters, manuscript in review with the *J. Acoust. Soc. Am*.

Hedlin, M.A.H. and B. Alcoverro (2002) The use of impedance matching capillaries for reducing resonance in rosette spatial filters, manuscript in preparation for the *J. Acoust. Soc. Am*.

Hedlin, M.A.H. and R. Raspet (2002) Evaluation of an infrasonic noise-reducing barrier, in preparation for *J. Acoust. Soc Am.*, submitted June 14, 2002.

Zumberge, M.A., J. Berger, M.A.H. Hedlin, R. Hilt, S. Nooner, and R. Widmer-Schnidrig (2002) An optical fiber infrasound sensor: a new lower limit on atmospheric pressure noise between 1 Hz and 10 Hz, in preparation for *J. Acoust. Soc Am.*, submitted June 14, 2002.
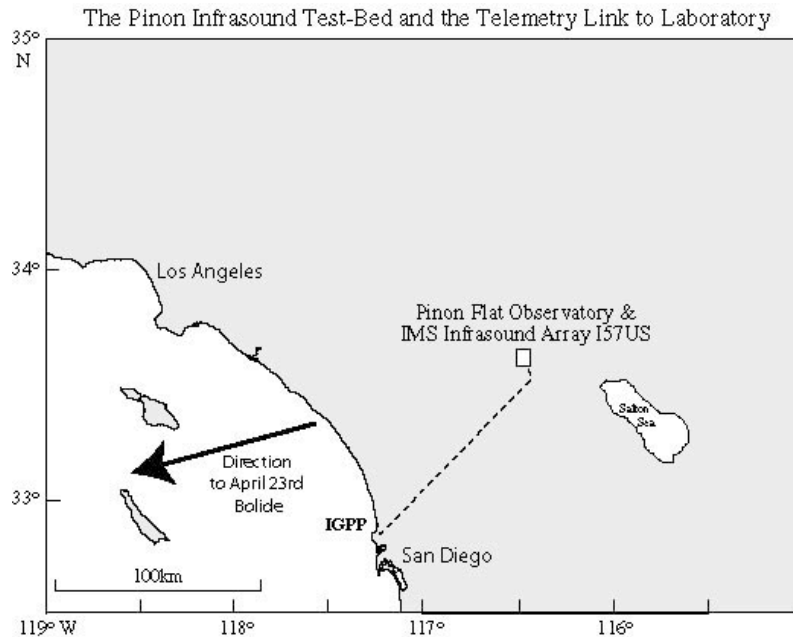

Figure 1. The IMS infrasound array, I57US, is located in the Anza Borrego desert at the Cecil H. and Ida M. Green Pinon Flat Observatory (PFO). The infrasound test-bed is located at PFO. The real-time radio-telemetry link to the laboratory (IGPP) is also shown. Signals from a large bolide that exploded to the SW of the observatory are used in this paper to calibrate the rosette filters.
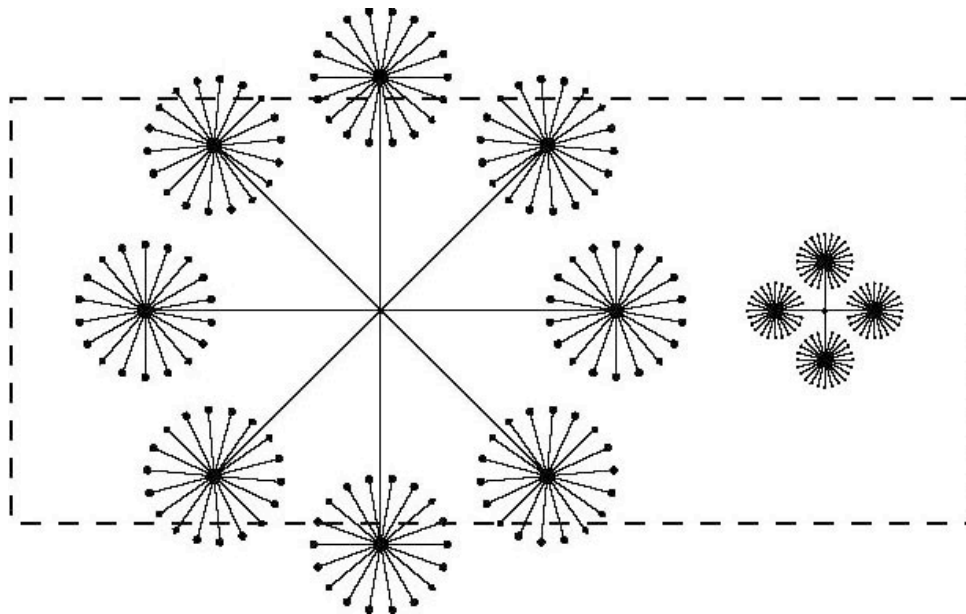
Figure 2: Two rosette filters considered in this paper are shown to scale with a National Football League playing surface. The 18-m filter comprises 92 low-impedance inlets in four rosettes. The 70-m filter comprises 144 inlets arranged in eight rosettes.
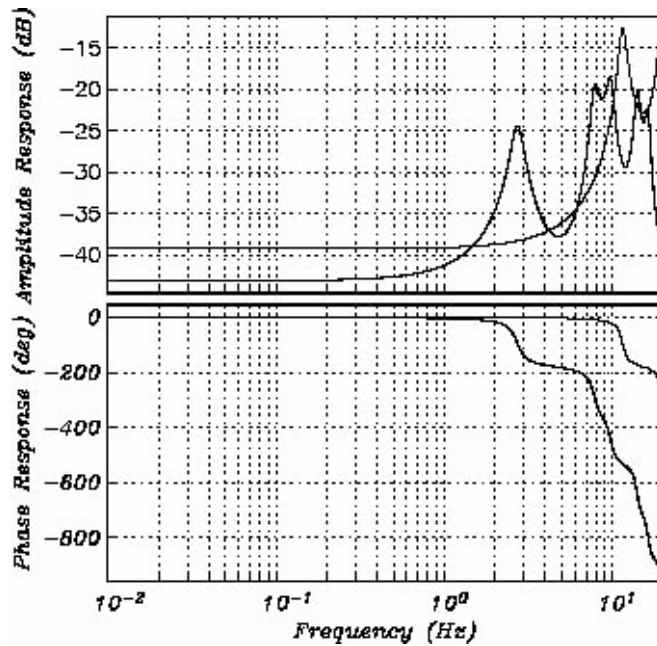
Figure 3: Predicted amplitude and phase response of the 18-m/92 rosette filter (light curve) and the 70-m/144 rosette filter (bold curve) for one inlet. The resonance peaks coincide with significant change in the phase response of the filter. The long-period response is given by -20 log10(N), where N is the number of inlets.

Figure 4: Simulated noise reduction of the 70-m/144-port rosette filter for various mean wind speeds is shown in the upper panel. Each curve represents the ratio between the noise spectrum observed at the reference port and the noise spectrum of the rosette system. The corner frequency of the 70-m rosette filter is predicted to increase with increasing wind speed. Observed noise reduction is shown in the lower panel.
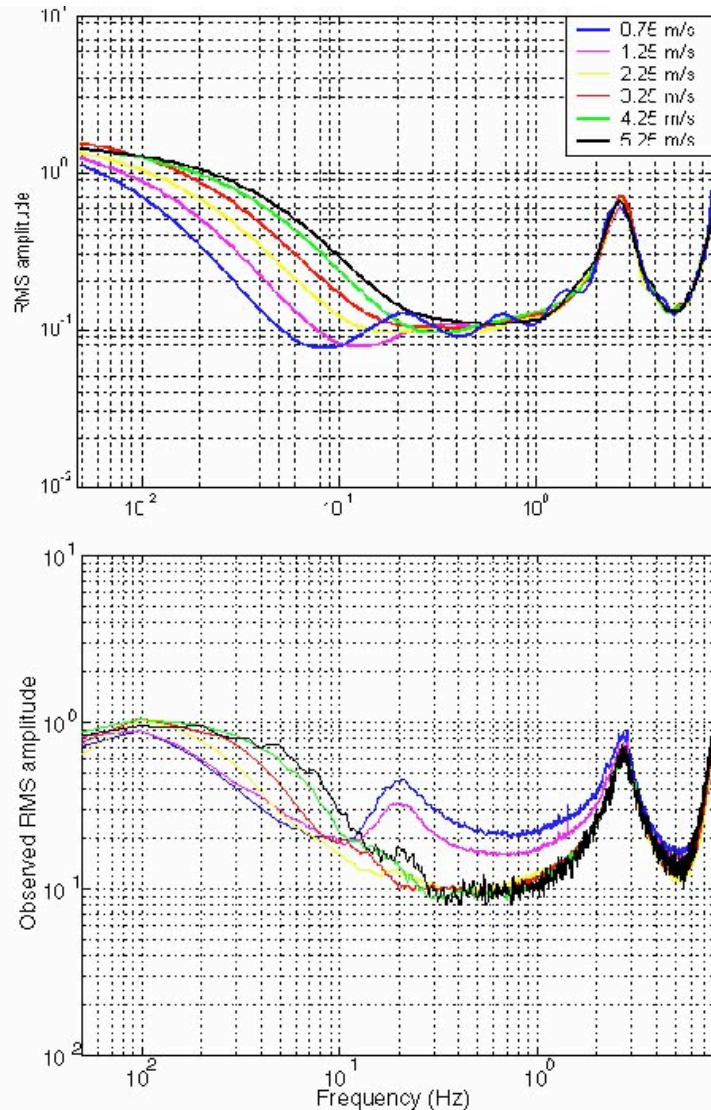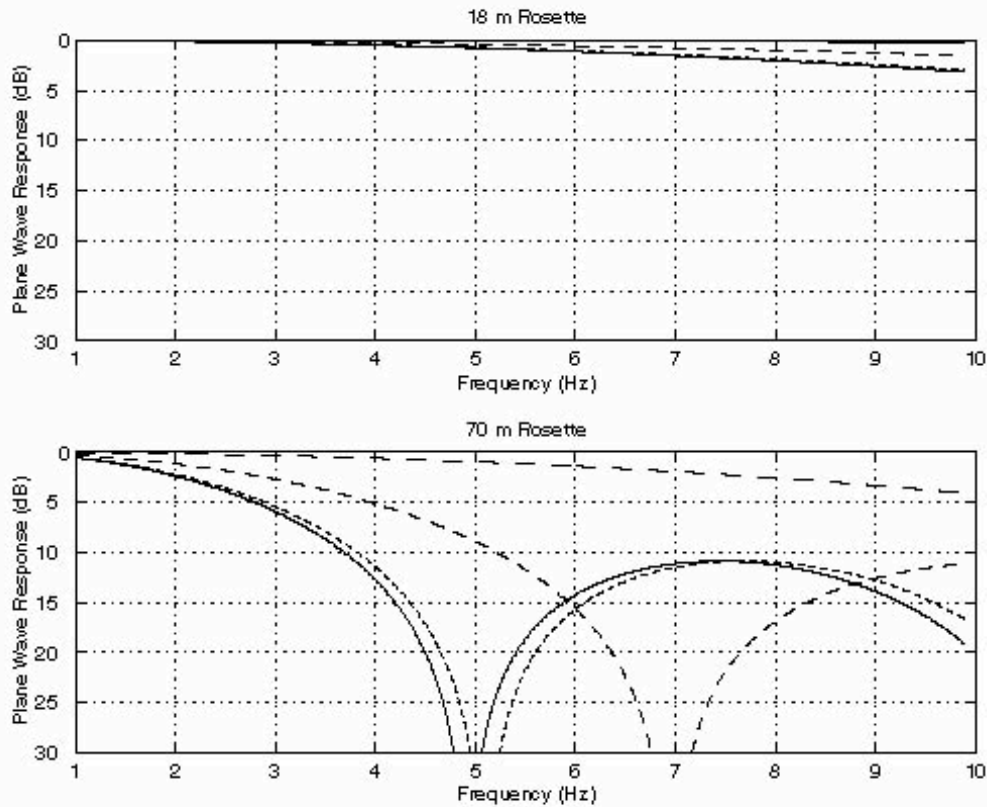
Figure 5: **The rosette filter integrates pressure variations from the inlets simultaneously regardless of the angle of incidence of the arriving energy. The rosette filter is tuned to vertically incident signals. Attenuation of signals increases with increasing arrival angle from the horizontal and with increasing frequency. The attenuation is strongly dependent on the aperture of the filter. For example, in the upper and lower panels we show the plane wave response for the 18- and 70-m rosette filters respectively at four arrival angles. The solid curves in each panel represent an arrival with an arrival angle of 0° above the horizontal. The finely to coarsely dashed curves represent signals propagating across the two filters at 15, 45 and 75° above the horizontal. The elevation angles, θ_e, are calculated assuming a sound speed, c, of 347 m/s. The phase velocity, c_p, is given by c/cos (θ_e). The phase velocities corresponding to the arrival angles at the four arrival angles are 347, 359, 491 and 1341 m/s. In both panels, the response for a vertically incident signal is 0 dB at all frequencies.**
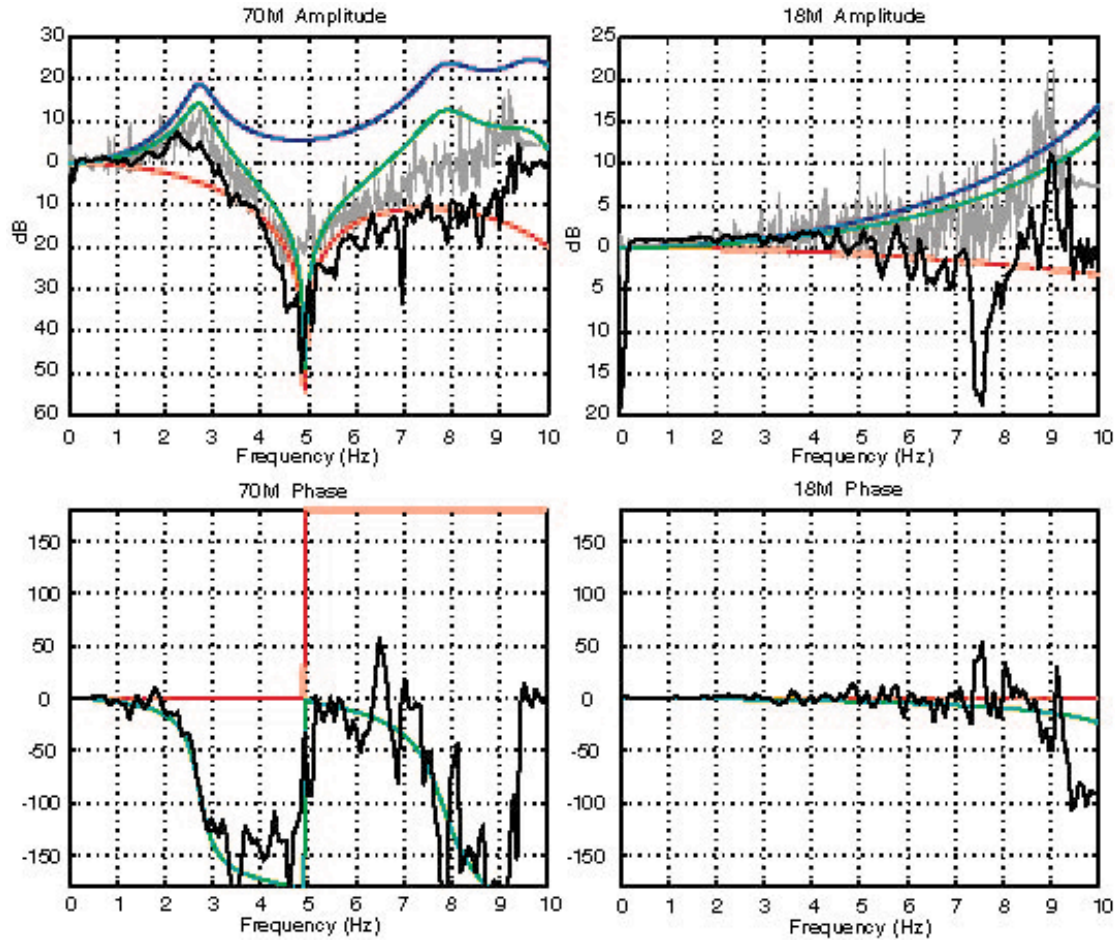
Figure 6: Amplitude and phase response of 18- and 70-m rosette filters are shown in this figure. The blue curves in all panels represent the response due to internal resonance inside the pipe systems. The red curves represent the plane wave response. The plane wave response of the filters, which is dependent on the phase velocity of the incoming energy, has been calculated at 330 m/s. This is the phase velocity of the energy from the April 23rd bolide as determined by processing data from the I57US array. The green curves represent the total response due to time delays between inlets and to resonance inside the filters. As shown in Figure 9, the 18-m filter attenuates the incident signal by less than 5 dB at all frequencies up to 10 Hz. The attenuation caused by the 70-m filter is strongly frequency dependent at this low phase velocity. A pronounced notch is predicted to exist at 5 Hz. Amplitude and phase from a phase-coherent cross-spectral analysis of data from the April 23rd bolide are shown in black. The theory accurately predicts the phase of the signal but under-predicts the amplitude at all frequencies. A spectral ratio of the filtered to unfiltered data (gray curves in the upper panels) closely match the theoretical predictions.
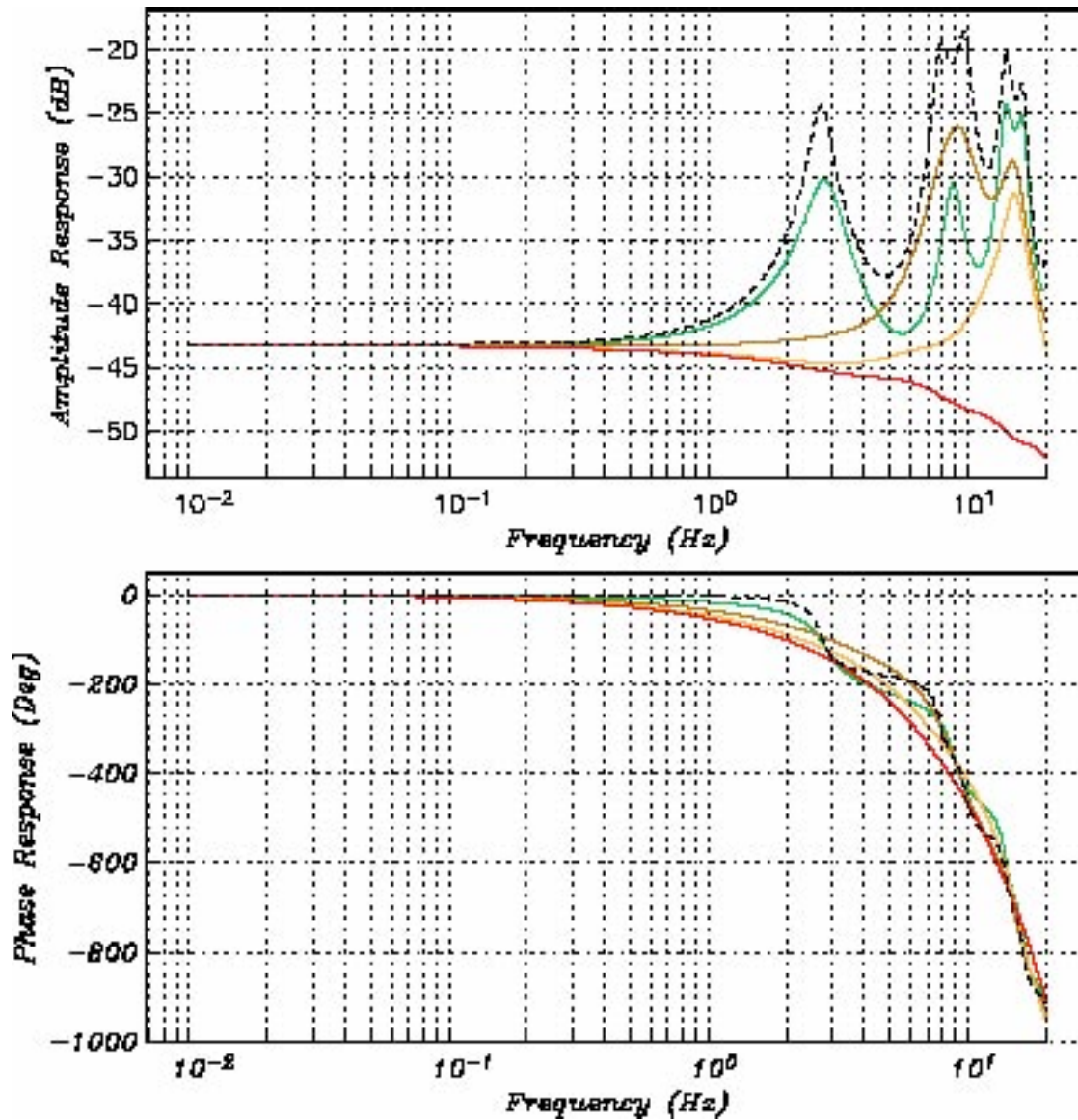
Figure 7: Simulations on the original and modified 70-m-aperture rosette filters are shown in this figure. The systems with capillaries at the inlets, secondary summing manifolds, both the inlets and the secondary summing manifolds, at the inlets and both summing manifolds are represented by the brown, green, gold and red curves. The unmodified system is represented by the dashed curves.
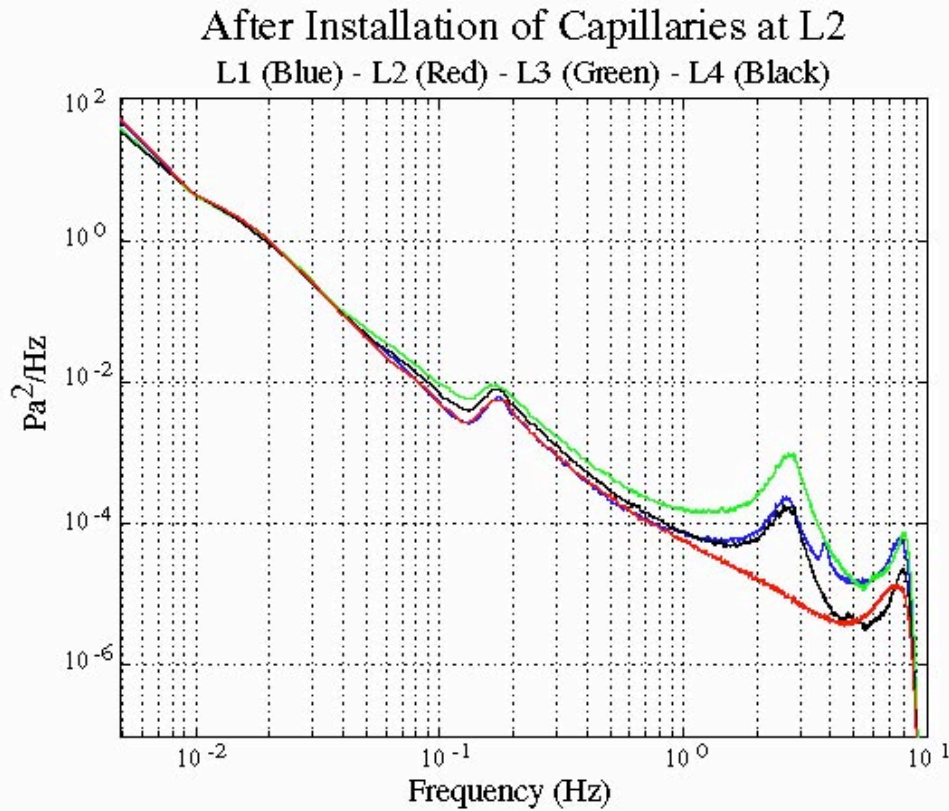
Figure 8: Spectral density estimates taken from data collected after the capillary plugs were installed at site "L2" (red curve). The capillaries have removed the resonance peak at 2.65 Hz.
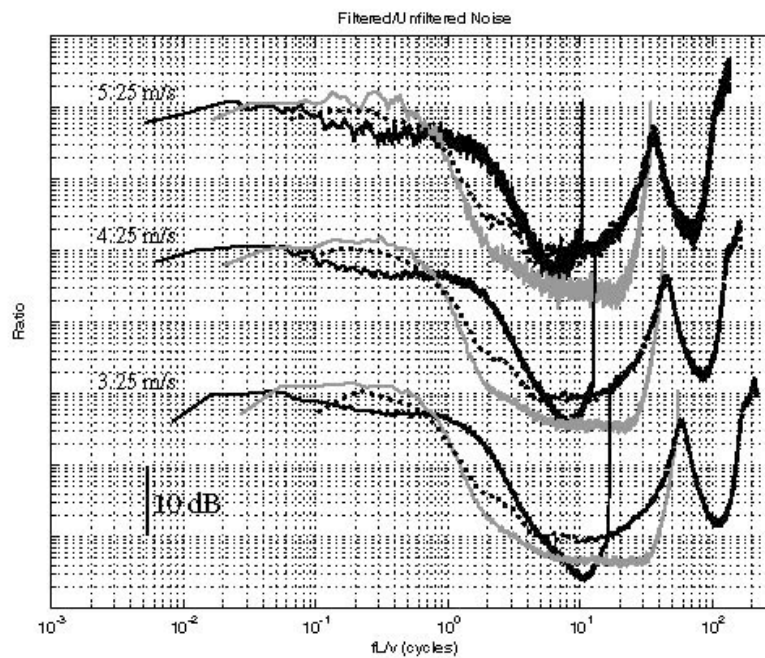

Figure 9. Wind-noise reduction versus scaled frequency at 3.25m/s, 4.25m/s, and 5.25m/s for the 70- rosette (bold dots), the 18-m rosette (bold gray) and the 5.5-m wind barrier (solid curves).

OPTIMUM FILTRATION OF ACOUSTIC PULSES CAUSED BY UNDERGROUND NUCLEAR AND ABOVE-GROUND CHEMICAL EXPLOSIONS

V. Krasnov and Ya. Drobzheva

Institute of the Ionosphere, Ministry of Science and Education, Republic of Kazakhstan

ABSTRACT

For identification of acoustic pulses from explosions, we devised a method using optimum filtration of signals. As a reference signal we use the calculated form of an acoustic pulse. To describe the propagation of an acoustic pulse through the inhomogeneous atmosphere, we developed a new equation and corresponding computer simulation code. The model takes into account nonlinear effects, inhomogeneities of the atmosphere, absorption, expansion of a wave acoustic front, etc. At present the model is developed for the ascending part of a trajectory of an acoustic ray: from a ground surface up to the height of a reflection point (ionospheric height). Data from parachute measurements of acoustic pulses, and measurement of acoustic pulses at different heights in the ionosphere along with Doppler radio soundings were used to test the model.

The program includes the following subroutines:
1. Subroutine of the vertical movement of the earth's surface during an underground nuclear explosion (we use an empirical model).
2. Subroutine of a calculation of atmospheric parameters (we use an MSIS model).
3. Subroutine of a calculation of wind profile along an acoustic ray trajectory (we use a HWM model).
4. Subroutine of an acoustic pulse generation by a spall zone.
5. Subroutine of acoustic pulse generation by an above-ground chemical explosion (we developed a new initial form of an acoustic pulse).
6. Subroutine of the propagation of an acoustic pulse from the earth's surface up to the ionospheric height.
7. Subroutine of the calculation of the ionospheric profile (we use an IRI model and data of an ionogram).
8. Subroutine of acoustic wave influence on the ionospheric plasma.
9. Subroutine of the trajectory of radio wave propagation in the ionosphere (we account for the geomagnetic field).
10. Subroutine of the ionospheric perturbation influence on the Doppler frequency of a radio wave.
11. Subroutine of the optimum filtration.

We used data from the Mill Race experiment (an above-ground chemical calibration explosion for which the yield was 500 ton TNT) to test the model calculations simultaneously at eight different locations in the low atmosphere and ionosphere. The correlation coefficient between the calculated and the experimental form of the acoustic pulse was in the range of 0.85 to 0.98. The average mean yield of the explosion was 531 ton TNT with a standard error of $\pm$ 34 ton. We also estimated the yield of the Flixborough explosion using the data from six independent measurements of acoustic pulses at ionospheric heights. The reconstructed oblique radio soundings agree remarkably well with experimental results when a ground source explosion yield of 283 $\pm$ 38 tons of TNT is utilized. We used the data from the Soviet – US experiment (underground nuclear calibration explosion at the Semipalatinsk test site in 1988, the yield of which was about 150 kiloton TNT) to test the model calculations simultaneously at three different locations in the ionosphere. The correlation coefficients between the calculated and experimental forms of the acoustic pulse were 0.83, 0.8 and 0.68. The probability of detection of a signal was equal to one with the threshold of acceptance of the cross-correlation set equal to 0.4.

OBJECTIVE

The manner in which infrasound monitoring can aid in remote detection and identification of underground nuclear explosions has been the subject of some exploration. We propose the theory of optimum filtration as a way for infrasound to be applied to this problem. The optimum analysis should include: a correlation device and a reference signal such that:

$$R(\tau) = \int_{0}^{T} f_s(t) f_p(t - \tau) dt \; ;$$

where $f_s(t)$ input is the infrasonic signal and $f_p(t)$ is the reference signal – the infrasonic "portrait" or analysis of an explosion.

To produce analyses of explosions, we can use theoretical calculations. Obviously, the correlation between physical and numerical models and experimental results should be sufficiently high. The model should take into account the following factors:

- Process of generation of an acoustic impulse by an explosion.
- Oblique propagation of acoustic impulses in the real atmosphere.
- Reflection of an acoustic wave from the atmosphere.
- Propagation of acoustic impulses back down to the receiver.

Each of the four parts of this model should be experimentally verified. For long distances, acoustic pulses (infrasound) are propagated from the earth's surface to an altitude about 100-120 km (ionospheric heights). Thus, it is possible to use experiments on radio sounding in the ionosphere (for example, Doppler radio sounding) for testing a model at these heights. As a result we have developed new theoretical models and corresponding computer simulation codes that account for the entire range of atmospheric and ionospheric phenomena involved in the technique, from the generation of acoustic pulses by surface ground motions during underground nuclear explosions to the synthesis of radio frequency signatures recorded by ionospheric radar systems (Drobzheva and Krasnov, 2002). The model accounts for non-linear effects, atmospheric and ionospheric vertical inhomogeneity, absorption, diffraction effects, geomagnetic field, horizontal wind, etc.

The purpose of our work: to show the efficiency of the optimum filtration method for detection of acoustic impulses from chemical and underground nuclear explosions from the ionosphere.

RESEARCH ACCOMPLISHED

The first and second parts of the model were tested with experimental data obtained during the Mill Race experiment (Banister and Hereford, 1991; Warshaw and Dubois, 1981) and the Soviet – US experiment (09/14/88). In the Mill Race experiment, data collected during the surface burst of a 500-ton TNT equivalent chemical explosion represented a unique opportunity to assess the credibility of calculations used to evaluate the yield of surface explosions from atmospheric and ionospheric measurements. The evaluation of the model used the results of atmospheric pressure variation measured by probes suspended by four parachutes at an altitude of about 10 km at horizontal distances of 1.9 to 16.3 km from a vertical line through the explosion point. Doppler shift records (f_d), made when radio waves were reflected from the altitudes of about 151, 222, 242 (vertical sounding) and 263 km (oblique sounding) were also used. It was therefore possible to test the model calculations simultaneously at eight different locations in the atmosphere and ionosphere. To estimate the yield of the explosion, the forms of the calculated and experimental acoustic and Doppler disturbances for a variety of explosion yields were compared. This comparison took the form of determining the correlation coefficient (K) between calculated and experimental values and choosing the value of the explosion yield when the correlation coefficient achieved its maximum value. Figure 1 and Table 1 indicate the results of these comparisons.
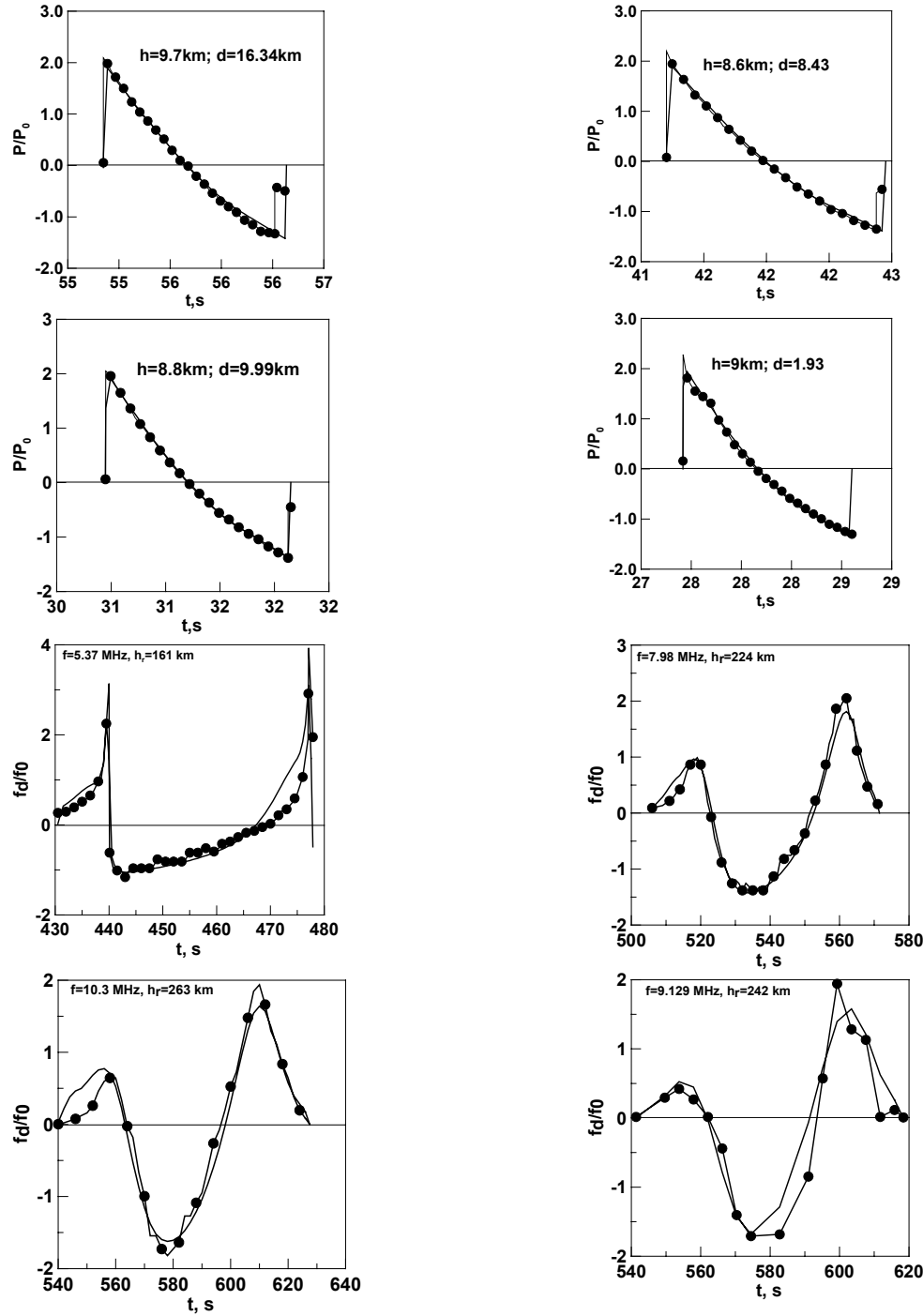
Figure 1. Comparison of calculation results of acoustic and ionospheric perturbations for the Mill Race experiment. Calculations are represented by solid lines and experimental results by dots; h – altitude of observation, d – horizontal distance from the site of explosion, f - frequency of radio sounding.

Table 1. Mill Race Explosion Yield; comparison of experiment to theory.

h (km)	K (correlation coefficient)	Q (ton TNT)	Error in Q (%)
8.6	0.95	450	10
8.8	0.973	550	10
9.0	0.964	550	10
9.7	0.943	450	10
161	0.85	700	40
224	0.989	600	20
242	0.952	400	20
263	0.982	550	10
mean	-	531	6.4

It is necessary to note that there are some differences between the experimental and calculated arrival times of the disturbances. However, to show the agreement between the experimental and calculated waveforms, these were matched by arrival time; any error in the calculation of the arrival time does not exceed 5%.

The average mean of the explosion determined in this manner is 531 ton TNT with a standard error of the mean of ±34 ton. The calculated result agrees well with the experimental value. It is important to note that in spite of using numerous input data (profiles of atmospheric pressure, density, sound speed, ionosphere, etc.), the calculation results show only a small spread in values of yield; ±6.4%. The reason for this is that the parameters of acoustic disturbances depend critically on explosion yield and the altitude profile of atmospheric density (Drobzheva and Krasnov, 2001; Drobzheva and Krasnov, 2002). In turn, any error in the determination of the model of atmospheric density is small – about a few per cent.

In the Soviet – US experiment, data collected during the calibrated underground nuclear explosion of 150 kiloton TNT equivalent represented a unique opportunity to assess the credibility of calculations from ionospheric measurements. Doppler shift records were recorded when radio waves were reflected from the altitudes of about 179, 210-213, 221 km (oblique sounding). It was therefore possible to test the model calculations simultaneously at three different locations in the ionosphere. Figure 2 indicates the results of the comparisons.
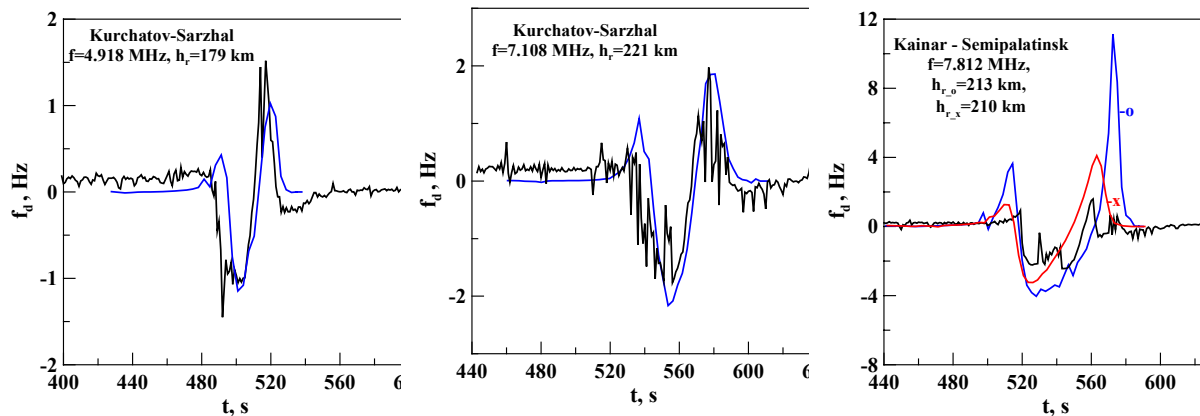

Figure 2. Comparison of calculation results of ionospheric perturbations for the Soviet - US experiment. Black line = experiment, dark blue line = calculation for an ordinary radio wave and red line = calculation for an extraordinary radio wave. h = altitude of observation, f = frequency of radio sounding.

A coefficient of cross-correlation between calculated and experimental curves produced the following results: 0.83 (for Fig. 2a), 0.8 (for Fig. 2b), 0.61 (for Fig.2c - for an ordinary radio wave), 0.68 (for Fig. 2c - for an extraordinary radio wave). The smaller coefficient of correlation for the case in Figure 2c is caused by the fact that the heights of a reflection of ordinary and extraordinary radio waves only differed slightly. As a result, perturbations on the Doppler

record were almost simultaneous for both types of waves. This caused an interference in the Doppler record. The model developed does not take into account interference effects.

During the Soviet-US experiment, the ratio of the signal to noise on Doppler records was more than one. Thus, it was not a problem to detect the signal. A more difficult task was encountered during an underground nuclear explosion on 12/27/87. Figure 3a, b represents initial Doppler records for two radio waves. Figure 3c, d represents the corresponding records after the optimum filtration; the signal considerably exceeds noise. If we determine the threshold of decision-making as a correlation coefficient of 0.4, then the probability of correct detection of the signal is equal to 100 %.
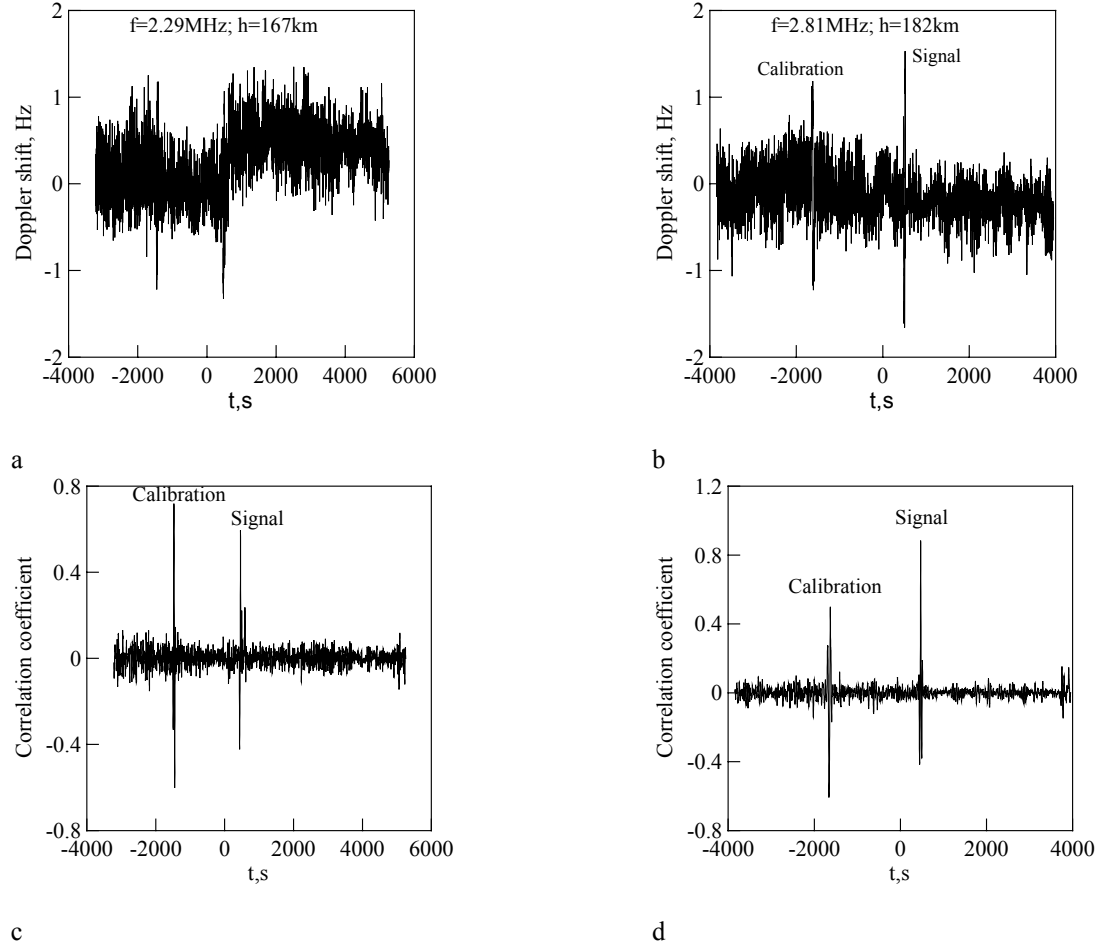
a

b

c

d

Figure 3. Doppler records before (a,b) and after (c,d) the optimum filtration for two radio trace.

Because the physical model agrees well with experimental results, it allows us to investigate the dependence of the form and magnitude of the Doppler response on the length of a radio trace during an underground nuclear explosion. The result of calculations for an approximately 210-km height of a radio sounding is represented in Figure 4 where it is shown that the form and magnitude of the Doppler response practically do not depend on the length of a radio trace. At the same time, these parameters are highly dependent on the height of radio wave reflection and horizontal distance between the radio wave reflection point and the explosion site. Because radio waves of short wave range can propagate all around the globe, the ionospheric method of detecting acoustic impulses due to explosions has no distance restrictions.
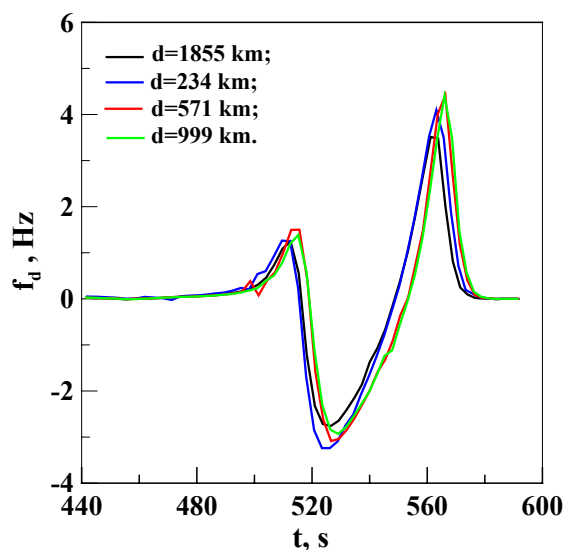
Figure 4. Dependence of Doppler response on length (d) of a radio sounding trace

CONCLUSIONS AND RECOMMENDATIONS

The method of optimum filtration can be effectively used for remote detection of "signals" due to explosions, at least, for detection of infrasound signals at ionospheric heights. It is interesting to test this method using ground-based infrasonic measurements. However, we need to develop the theory and corresponding computer simulation codes for acoustic wave reflection from an atmospheric layer and propagation of acoustic pulses from the point of reflection back to the earth's surface.

ACKNOWLEDGEMENTS

REFERENCES

Banister J.R. and W. V. Hereford (1991), Observed high altitude pressure waves from an underground and surface explosion. *J. Geophys. Res*., **96**, No.D3, p.5185-5193.

Drobzheva Ya.V. and V. M. Krasnov (2002), The acoustic field in the atmosphere and ionosphere caused by a point explosion on the ground. *J.Atmos.Solar-Terr. Phys*., in press.

Drobzheva Ya.V., and V. M. Krasnov (2001), The spatial structure of the acoustic wave field generated in the atmosphere by a point explosion. *Acoustical Physics*, **47**, No. 5, pp. 556-564.

Warshaw S. I. and P. F. Dubois (1981), Preliminary theoretical acoustic and RF sounding calculation for Mill Race. Report Lawrence Livermore National Laboratory, UCID-19231, USA, 20p.

THE BOLIVIAN ALTIPLANO INFRASOUND ARRAY IS08

Estela Minaya, Guido Avila, Cristina Condori, Alejandro Córdova, and Francisco Vega

Observatorio San Calixto

ABSTRACT

The main purpose of an infrasound station is to detect acoustic waves generated and transmitted in the atmosphere that are associated with nuclear explosions, volcanic eruptions, meteorological processes, and some large earthquakes such as the one that occurred on the Peruvian coast on June 23 of 2001 with magnitude Mw 8.4. That earthquake was recorded in the IS08 (International Monitoring System [IMS] designation) infrasound array located in the Bolivian Altiplano, 63 km from La Paz City, Bolivia. That array includes four microbarographs – three located at the vertices of a 1-km equilateral triangle and the fourth at the middle of the triangle. Transmission is via satellite communication to Departament Analyse Surveillance Environnement, France (DASE) and from there to the International Data Centre (IDC) in Vienna. Communication to the National Data Center (NDC) at the Bolivian Observatorio San Calixto is by a telemetric system with three relays.

Monitoring started in November 2001 and the first observations indicated some apparent anomalies. We compared to the infrasound data reported in the bulletin of CEA (Commissariat a l'Energie Atomique, France), and we found that 57 signals recorded by the array were not reported in that bulletin. To understand the discrepancy, we have analysed the monthly statistical data obtained by our transmission and the data received at CEA to see if the signal loss could be due to transmission gaps. The time at which the data losses occurred does not coincide with those recorded at the CEA, so we are trying to see what could be the cause of that difference. Our monitoring shows a signal that coincides with a small earthquake (magnitude 3) that occurred on March 23, 2002, and was located 84 km away from the array. This signal was recorded by only three elements of the array. We are still working to find the cause. We are applying software to determine the frequencies of that signal and other parameters that allow us to find some associations with any known source that generates acoustic infrasound waves.

OBJECTIVE

The objective of this research is to study all aspects related to the acoustic waves generated in the atmosphere and recorded by the infrasound array IS08 and to determine waveform, origin or cause of generation.

RESEARCH ACCOMPLISHED

Introduction

The installation of the infrasound array in the town of Peñas in the Bolivian Altiplano, approximately 63 km to the northwest of La Paz City, was completed in December 1999 and complements the other South America stations that form part of the International Monitoring System (IMS) of the Preparatory Commission for the Comprehensive Nuclear-Test-Ban Treaty Organization (CTBTO). Station IS08 began infrasound monitoring and transmitting data in December 2001. The monitoring consists of the routine analysis of the microbarographs, obtained by the four elements that comprise the infrasound array IS08. The monitoring allows us to determine any type of physical interruption to the equipment and the quality of transmissions to data analysis centres. This routine analysis has allowed us to do
1. statistical analysis of the telemetric transmission of the signals;
2. comparison of the telemetric transmission (to OSC - CND, La Paz - Bolivia) and VSAT (to DASE); and
3. signal discrimination that corresponds to an acoustic source or other types that are not yet defined.

The previous experience that we have consist of investigations with data recorded by an infrasound acoustic array installed in 1966 as an asymmetric array with seven microbarographs, with more than 2 km of separation between the elements (Table 1).

The major part of this previous analysis covers nuclear explosions, large earthquakes, volcanic eruptions and some signals generated on the surface area of the south Pacific (Fernández, 1969) that the infrasound array in the Bolivian Altiplano registered effectively, especially for waves from large distances. Escobar (1971) indicated that this effect was caused by a small attenuation factor due to large wavelength. These results are influenced by several factors that exist in the area, i.e., the altitude, 4000 m.a.s.l. and low air density, aspects that have a beneficial effect on the signal/noise ratio. Because of the meteorological conditions in the Bolivian Altiplano, the infrasound noise at night is 20 times lower than the noise during the day. The asymmetric distribution of the first array was a factor in the study of events with long periods and large distances between the focus of the events and the locations in the array.

Those studies did not consider local events because at short they distances do not generate long-period waves. But it is very important to know about the process of generation of that kind of infrasound wave. For example La Paz City, on February 19, 2002, suffered a sudden and very severe storm that lasted for 45 minutes (about 70 people dead and great structural damage). The distance from the city to the array is 63 km, but this natural phenomenon (severe storm) apparently was not recorded by the infrasound array IS08. On the other hand, a large earthquake that occurred in Peru on June 23 of 2002 was recorded very clearly due to the generation of long-period waves as shown by Le Pichon (2002).

Table 1. Former infrasound array located in Peñas

CODE	DATE	LATITUDE	LONGITUDE	ALTITUDE (mt)
A	1966-1975	16.2135°	68.4397°	4120
B	1966-1975	16.2885º	68.4186º	4005
C	1966-1975	16.2659º	68.4717º	3960
D	1966-1975	16.2397°	68.4735°	3970
E	1970-1975	16.1996°	68.3268°	4660
F	1970-1975	16.2944°	68.2585°	4680
G	1970-1975	16.3922°	68.3074°	4300
LP1B	1999-	16.2173º	68.4442º	4071
LP2B	1999-	16.2022º	68.4559º	4032
LP3B	1999-	16.2150º	68.4552º	4042
LP4B	1999-	16.2215º	68.4636º	4017
Relay				
Patamanta		-16.3182º	-68.2962º	4480
Cruce Chacaltaya		-16.3833º	-68.1666º	4628
El Alto		-16.4814º	-68.1677º	4020
OSC (Reception)		-16.4905º	-68.1325º	3658

IS08 infrasound array

The infrasound station IS08 is located in the Peñas region, specifically in the area of Isquillani and Tuquia, Department of La Paz, at about 63 km La Paz City. It was installed at the end of 1999. The array has a symmetric distribution. It is composed of four sensors (Figure 1) and has three at the vertices of an equilateral triangle and one at the center with a separation between them of 1 km. There are two modes of data transmission, one through telemetry to the Observatorio San Calixto, La Paz Bolivia, and the other by VSAT (Figure 2) to Champagne (east of Paris) then to DASE and finally to the International Data Centre in Vienna, Austria. The telemetry transmission is performed by relay (Figure 2).

Each station has a sensor and an acquisition system and transmission unit, with a 12-V power supply and the transmission antenna. The sensor, model MB2000, was built by DASE. The sensor measures small variations of atmospheric pressure and also those generated at large distances. The sensitivity of the output is 1 MV/Pa, the frequency response is 0.001 to 40 Hz, and, for filtered output, 100 s to 27 Hz, electronic noise is less than 2 mPa rms (0.02~4 Hz).

The weather sensor is located next to LPN1 (Figure 1). The wind direction, speed, air humidity and temperature are recorded by telemetry in the Bolivian NDC, Observatorio San Calixto.

The data are transmitted from the central station LPN4 (Figure 1) to OSC to check and to validate the digital signals. Remote monitoring is performed by CRISTAL software at DASE and OSC.

Array environment

It is necessary to have a clear picture of the topography in the array environment; i.e., the region of the array and the relays. We need to know if the variation in topography can be the cause of generated infrasound waves, and how much the infrasound variations can be attributed to small changes in temperature near the array.

Local Geology

Geomorphologically, the station array is located on glacial lacustrine to fluvio lacustrine deposits, constituted of blocks of sand, slime and clay. Microthermal ground covered with moss and straw can be found on these sediments that form the Altiplano. There are small mountainous areas with some rivers in different directions.

Topography and average altitude

The topography of the area of the stations is quite moderate and almost flat with an average elevation of 4000 m.a.s.l. The infrasound stations are surrounded by a series of peaks; to the North is the hill Huari Umaña with a height of 4484 m.a.s.l., to the Southwest the hill Allkamarini and the hill Pucuni Arc with an elevation of 4156 m.a.s.l., and to the South the hill Peñas consists of a pair of peaks, Chucecani and Peñas with a height of 4333 m.a.s.l.

To the east of the station is a plain with elevations that rise as we approach the mountain Huayna Potosí and the relay station Patamanta (Figure 3), which is located on the hill Cotan Kkollu with an altitude of 4400 m.a.s.l., and finally the relay station Cruce Chacaltaya that is located at an altitude of 4500 m.a.s.l.

Analysis of signals

The parameters observed on the microbarograms do not show great regularity in periodicity or amplitude, they appear as isolated events with a specific arrival time and direction. This was confirmed by routine analysis that detected 57 signals from December 2001 to February 2002. The signals acquired by the array were not reported by the Infrasound Bulletin of IS08 published by CEA. Two signals are shown in Figure 4.1 and 4.2 and Table 2. The first signal is impulsive; has SE direction and 6.8 second duration, but an amplitude of only a few Pa. The second signal has SW direction, four second duration and is less clear than the first, especially on the LP4B sensor.

Table 2. Signal recorded by infrasound array IS08

Date	Origin Time	Duration (s)	Azimuth	Speed	Filter (Hz)
10/02/2002	09:24:43	6,38	NO CEA		0,1-9
11/02/2002	20:26:10	4	NO CEA		0,1-9
23/03/2002	21:11:00	4	NO CEA		0,3-3,5
12/04/2002	09:54:40	1.31	118,8	0,639	0,1-9
14/04/2002	18:59:20	4.7	74,9	0,383	0,1-9

NO CEA: Signals not reported by CEA Bulletin.

The main cause of those differences between the local analysis and the CEA bulletin was attributed to data transmission. To confirm this situation and to determine its cause, we compared the transmission of the data sent through telemetry and the data sent through satellite communication for each element of IS08 array (Figure 2) Statistical analysis was conducted of data losses during transmission reported each month. Figure 5 shows the analysis for February and no correlations were found between the comparative statistical analyses. We can say that the signals discussed above are very small and probably are local.

In this analysis the topography was considered as a probable generator of infrasound waves at short distances. The topography near to the array is almost flat, but the surrounding area has elevation differences due to the presence of the Cordillera Oriental. More work is needed to verify this hypothesis .

The third signal in Table 2 corresponds to a local earthquake with magnitude Ml 3, and 84 km distance from the source to the array. A filter of 0.8 to 3.5 Hz was applied. Figure 6 shows the seismic and infrasound waves recorded by three barographs. On LP1B, the signal is unclear, the arrival is emergent, and the spectrum shows a frequency of 2 Hz, which confirms the presence of a long-period wave.

Two signals are shown in Figures 7 and 8 that could be generated by local effects. Both records are local and the arrival waves are impulsive; the difference between them is the duration. The spectrum does not show considerable variation between frequencies, and there is background noise.

CONCLUSIONS AND RECOMMENDATIONS

Many of the signals recorded up to now should be considered a consequence of small vibrations with displacements or very small variations of temperature and pressure in the atmosphere that usually accompany infrasound waves.

The analysis shows that signals could give enough information to conduct more precise research. It will be necessary as a second step of this research to use software such as the Progressive Multi-Channel Correlation (PMCC, Cansi, 1995) to determine parameters such as velocity, phase, and azimuth and provide a classification of infrasound waves (Bass, 2001).

REFERENCES

Bass, H.E., K. Gilbert, M. Garces, M. Hedlin, J. Berger, J.V. Olson, C.W. Wilson and D. Osborne. (2001), Studies of microbaroms using multiple infrasound arrays, 23rd Seismic Research Review: Worldwide Monitoring of Nuclear Explosions, Jackson Hole, Wyoming, p. 73-104.

Brown, D.J., C.N. Katz, R. LeBras, J. Wang and A. Gault. (1998), Infrasonic processing at the Prototype International Data Center. In Proceedings of 20th Annual Seismic Research Symposium On Monitoring A Comprehensive Test Ban Treaty (CTBT), Santa Fe, New Mexico, pp. 555-562.

Brown, D.J., C.N. Katz, R. LeBras, J. Wang and A. Gault. (1999), Infrasonic processing at the Prototype International Data Center. In Proceedings of 21st Annual Seismic Research Symposium On Monitoring A Comprehensive Test Ban Treaty (CTBT), Las Vegas, Nevada, II pp.86-95.

Brown, D.J., C.N. Katz, J. Wang and R.W. Whitaker. (2000), Tuning of automatic signal detection algorithms for IMS style infrasound arrays. In 'Proceedings of the 22nd Seismic Research Symposium: Planning for Verification of and Compliance with the Comprehensive Nuclear-Test-Ban Treaty', 12-15 September, New Orleans, Louisiana.

Cansi, Y.(1995), An automatic seismic event processing for detection and location: the P.M.C.C. method. *Geophys. Res. Lett*., **22**, 1021-1024.

Escobar, G. (1971), *Ondas Infrasónicas: Ruido y Señales Observadas en la Estación Geofísica de Peñas*. Thesis, Universidad Mayor de San Andrés, La Paz, Bolivia.

Fernández, L.M. (1968), Infrasonic Research – Peñas Acoustic Array. Final Report, Grant No. AFOSR-67-1177C, Observatorio San Calixto, La Paz, Bolivia.

Fernández, L.M. (1969). Spectral Characteristics of Infrasonic Acoustic Waves and Related Seismic Research. Interim Scientific Report, Publication, Observatorio San Calixto, La Paz, Bolivia.

LePichon, A., Y. Cansi and B. Alcoverro. (1999). International Monitoring System. Infrasound Technical Training Program. CEA – Bruyères-le-Châtel – Département Analyse Surveillance Environnement DASE/LDG – France.

LePichon, A., J. Guilbert and M. Van de Walle. (2002), Ground – Coupled air wave and diffracted Infrasound from the Arequipa, earthquake by June 23, 2001, CEA, Lavoratoire de Détection et de Géophisyque, France. Poster
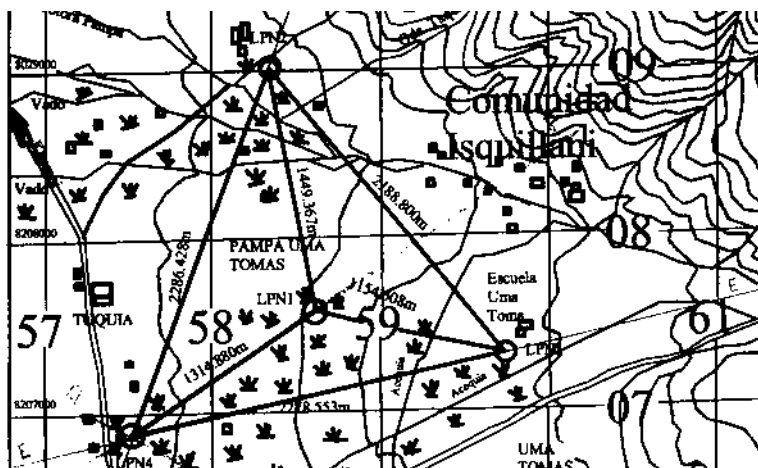
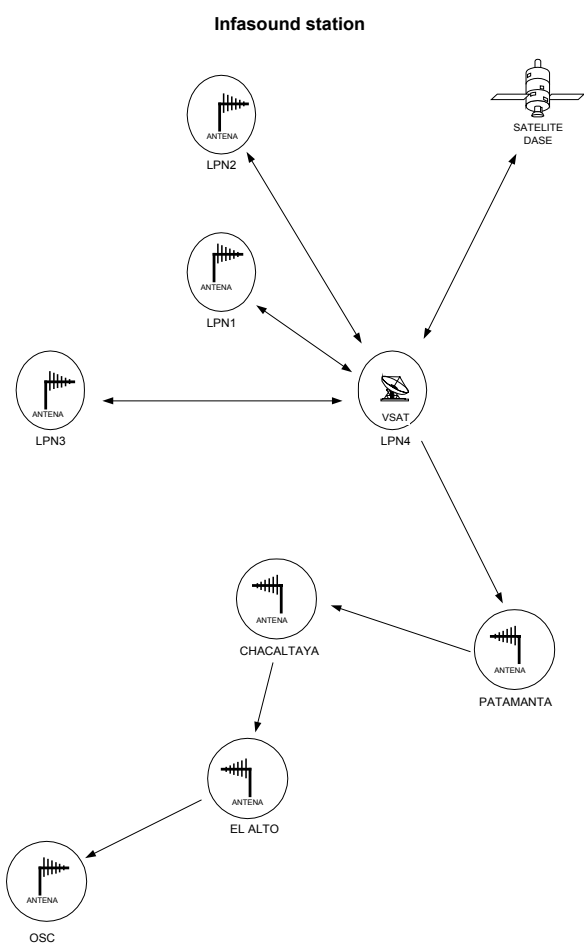**Figure 1:** Map that shows the location of the infrasound array

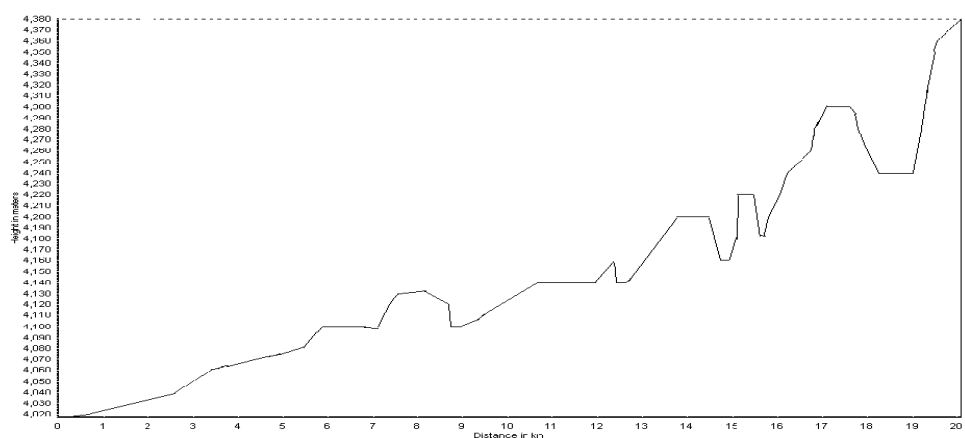**Figure 2:** Diagram of the communication network.

Figure 3: Topographical profile of the infrasound transmission from Peñas to Patamanta relay.
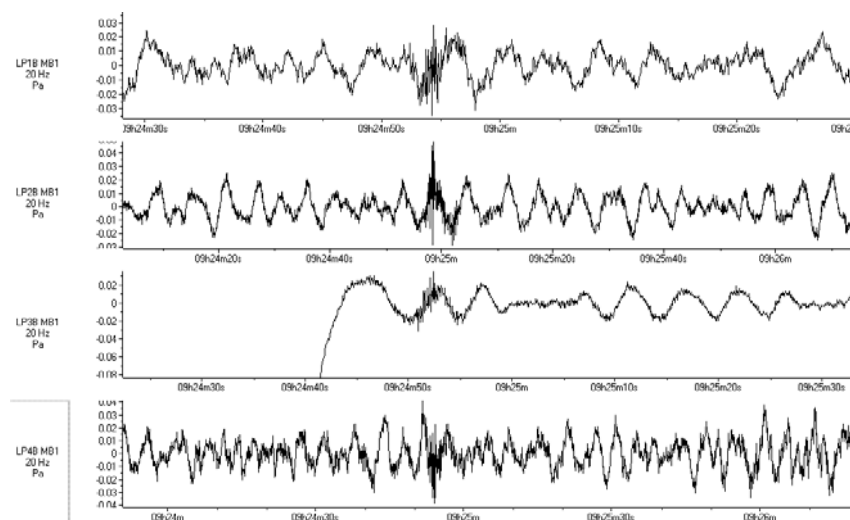

Figure 4.1: Signal of the 10/02/2002, 9:14 am, event, not reported by the CEA bulletin, with filter 0.1 to 9 Hz
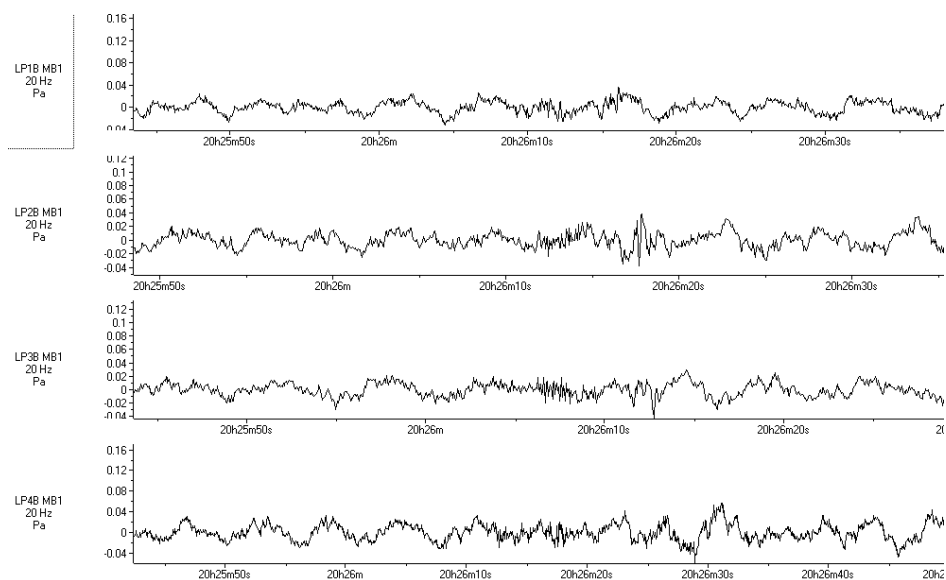
Figure 4.2: Signal of the 10/02/2002, 20:25 am event, not reported by the CEA
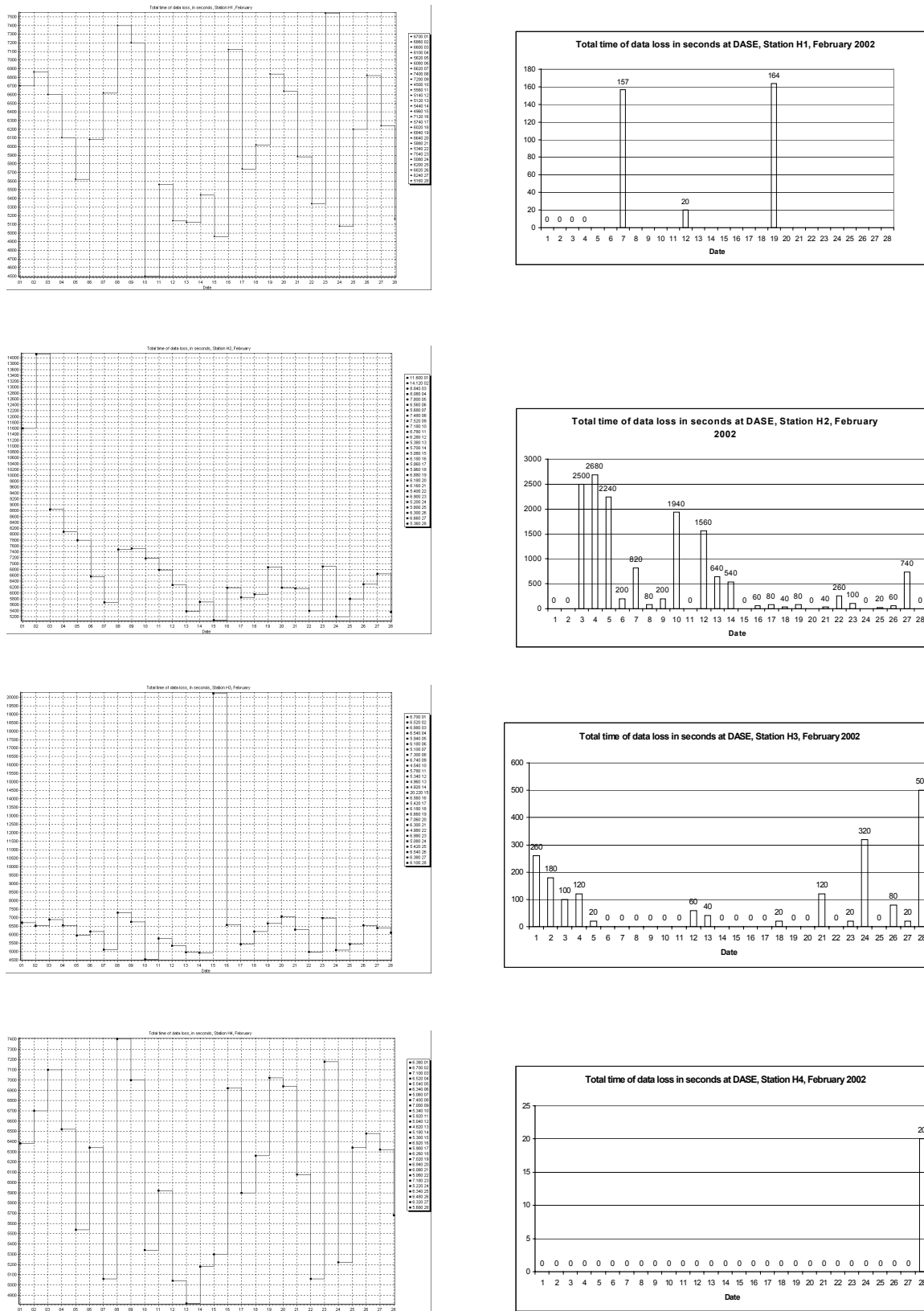bulletin, with filter 0.1 to 9 Hz

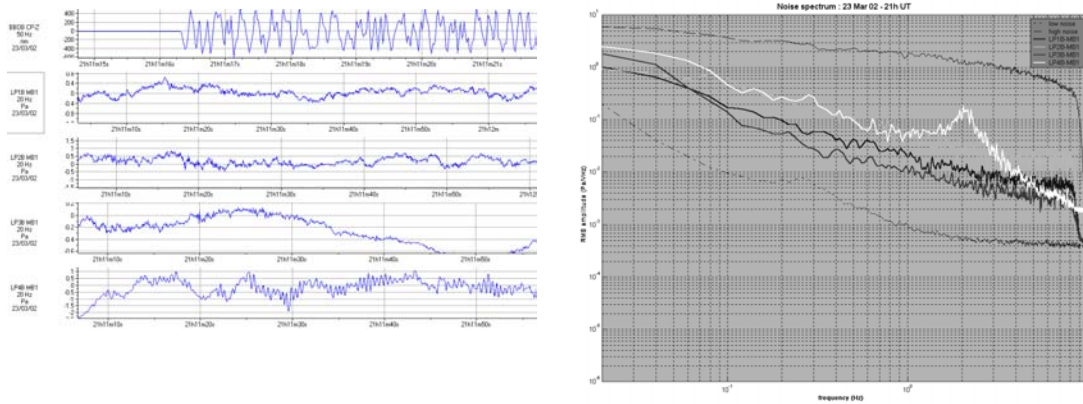**Figure 5:** Comparative statistical analysis of data loss at the OSC and at DASE

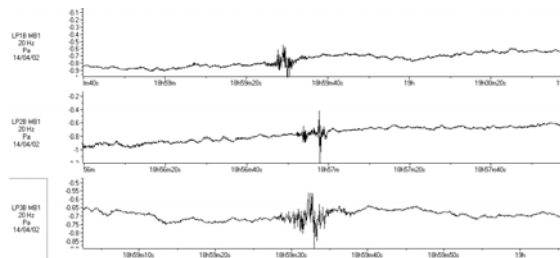**Figure 6:** Local earthquake of 23/03/02, detected by the infrasound array, and its corresponding spectrum.

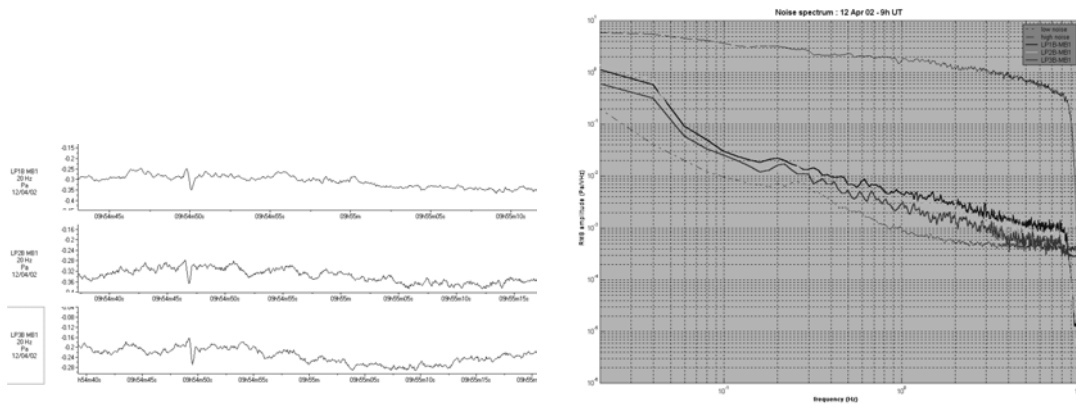**Figure 7:** Signal recorded 14/04/02, 18:59

Figure 8: Signal recorded 12/04/02, 9:54 am, direction SE, speed 0.639 m/sec

INFRAMAP ENHANCEMENTS: ENVIRONMENTAL/PROPAGATION VARIABILITY AND LOCALIZATION ACCURACY OF INFRASONIC NETWORKS

David E. Norris and Robert G. Gibson

BBN Technologies

ABSTRACT

Enhancements to the propagation modeling capabilities of the InfraMAP analysis tool kit are reported in three areas. InfraMAP (Infrasound Modeling of Atmospheric Propagation) consists of three infrasound propagation models (3-D ray trace, normal mode, and parabolic equation), two atmospheric characterizations (HWM and MSISE), a global topography database, and user interfaces for model execution and data visualization. InfraMAP has been delivered to the Defense Threat Reduction Agency's (DTRA's) research and development test bed and is currently being utilized by nuclear-explosion-monitoring researchers and analysts.

First, improvements have been made to the environmental variability analysis capabilities. Wind and temperature variability covers a wide spectrum, in both space and time. The dominant source of variability affecting infrasonic propagation is believed to result from gravity waves. A gravity wave spectral model based upon scale-independent diffusive filtering theory has been integrated into InfraMAP. The model is used to predict the horizontal wind perturbations as a function of height. As height increases, the spectral model amplitude increases, and there is an overall shift in energy towards lower wave numbers. Fourier inversion using random phase is applied to generate realizations of wind perturbation profiles. A dominant horizontal length scale and Gaussian weighting functions are used to generate range-dependent perturbation fields.

Second, the enhanced environmental modeling capabilities are used to evaluate the resulting variability in propagation. Multiple wind perturbation realizations are generated, and a Monte Carlo simulation is executed where multiple rays are traced through the sum of mean and perturbed environmental fields. Two ray parameters (travel time, azimuthal deviation) are calculated for each perturbation. The sensitivity of ray tracing calculations to variability in wind profiles is then quantified by computing the mean and variance of the predicted distributions.

Finally, prediction of propagation variability induced by the environment is used to evaluate the performance of infrasonic networks. Source localization is first computed from the measured station data. Then, modeled variance in travel time and azimuthal deviation, along with the uncertainty introduced by measurement error, are used to calculate the confidence bounds of the localization. These bounds are expressed as an area of uncertainty (AOU) for which there is a 90% probability that the actual source location is contained. For locations based upon travel time and azimuth, the AOU takes the shape of an ellipse. Network performance modeling is applied to data from the April 2001 Pacific bolide and compared to the satellite source localization.

OBJECTIVE

InfraMAP is a software tool kit designed for researchers and analysts who are interested in modeling infrasound in the atmosphere. Model output includes ray tracing, wind (HWM) and temperature (MSIS-E) mean atmospheric profiles, and wind perturbation profiles based upon power-law spectra. InfraMAP has been delivered to DTRA's research and development test bed, and enhancements that improve the model characterizations are under development. The ultimate goal is to accurately predict the achievable performance of infrasonic networks under various scenarios and environmental conditions.

Model enhancements and studies are reported in three areas. A gravity-wave spectral model has been integrated into the wind perturbation module; a propagation variability study has been completed using range-independent wind perturbation profiles; and, a network performance analysis of the April 23, 2001, bolide has been completed using both station measurements and propagation modeling.

RESEARCH ACCOMPLISHED

Environmental variability model

The baseline environmental variability model in InfraMAP is based on a power-law wind perturbation spectrum, and it provides realizations of wind perturbation profiles. This spectrum is applicable for small-scale turbulence, even though atmospheric turbulence covers a wide spectrum of spatial scales (Figure 1). The dominant source of variability affecting infrasonic propagation is believed to result from gravity waves. Gravity waves result from oscillations of air parcels displaced by buoyancy and restored by gravity. The oscillations have time scales ranging from minutes to tens of hours. Vertical length scales of gravity waves are in the range of 0.1 to 10 km, and horizontal scales can span from 100 to 10,000 km.
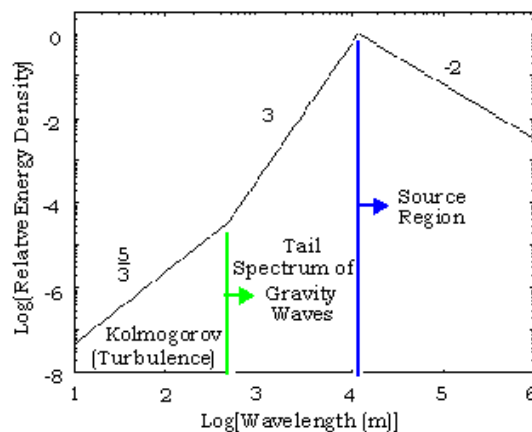

Figure 1. General form of horizontal wind spectrum versus vertical wavelength (from R. J. Sica, University of Western Ontario).

A significant body of research has been carried out to define the spectral character of gravity waves. The spectral model of Gardner (Gardner 1995, 1993) has been selected for integration into the environmental variability module. This model is based on scale-independent diffusive filtering theory. A source spectrum is defined near the ground. As the spectrum is propagated up in height, attenuation is modeled by introduction of diffusive damping. The key spectral properties are:
- an increase in energy with height
- a shift towards larger length scales with height
- an attenuation of smaller length scales with height

The Gardner Spectral model is evaluated at five discrete heights, as shown in Figure 2. These heights capture the dominant gravity wave variability from the troposphere up to the lower thermosphere. Below the troposphere, gravity waves are not fully developed. In the thermosphere, diffusion increases dramatically and gravity waves are damped out.
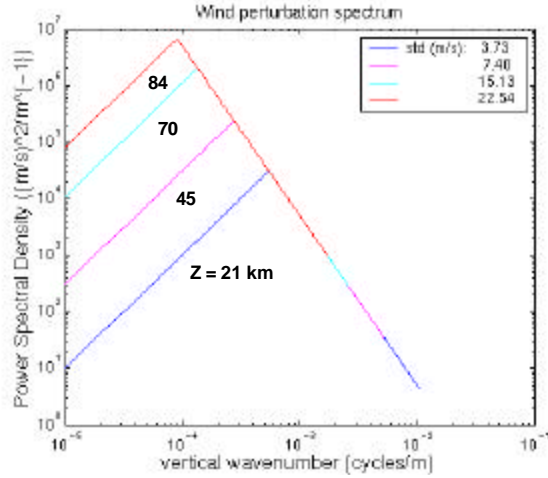

Figure 2. Gardner wind spectral model evaluated at five discrete heights.

Fourier inversion using random phase is applied to the spectra to generate realizations of wind perturbation profiles. A wind perturbation profile is generated for each of the five spectra. A composite profile is then computed by shading each profile spatially with a Gaussian filter and then summing them together, where Gaussian filter half-power points are set to the midpoint between each of the spectral heights. To model range-dependent variability, a dominant horizontal length scale is defined, and Gaussian weighting functions are used to combine the wind perturbation profiles. Figure 3 gives an example realization of a wind perturbation field generated from the gravity wave spectral model.
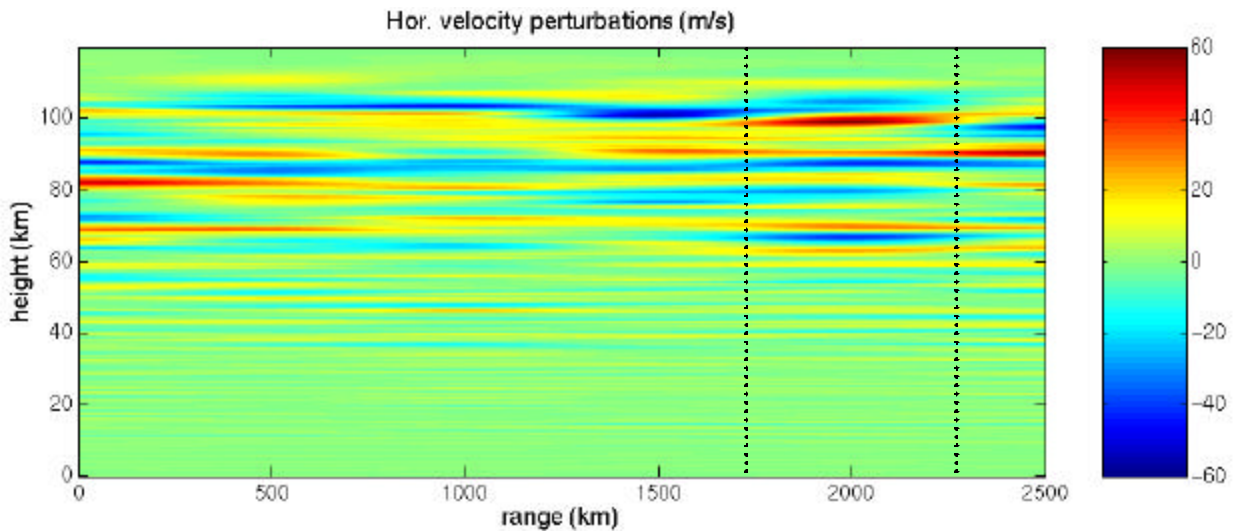

Figure 3. Range-dependent wind perturbations using horizontal correlation length of 500 km.

Propagation variability study

The goal of the propagation variability study is to quantify the bounds in travel time and azimuthal variability that can be expected. Different scenarios are evaluated over different diurnal and seasonal periods. The effects on both stratospheric and thermospheric rays are analyzed.

To perform the study, multiple wind perturbation realizations are generated, and a Monte Carlo simulation is executed where multiple rays are traced through the sum of mean and perturbed environmental fields. Two ray parameters (travel time, azimuthal deviation) are calculated for each perturbation. The sensitivity of ray tracing calculations to variability in wind profiles is then quantified by computing the mean and variance of the predicted distributions. Figure 4 gives an example of the predicted distribution of azimuth deviation of a thermospheric ray over a 500-km path. In this case, the deviation was under 0.2 degree.
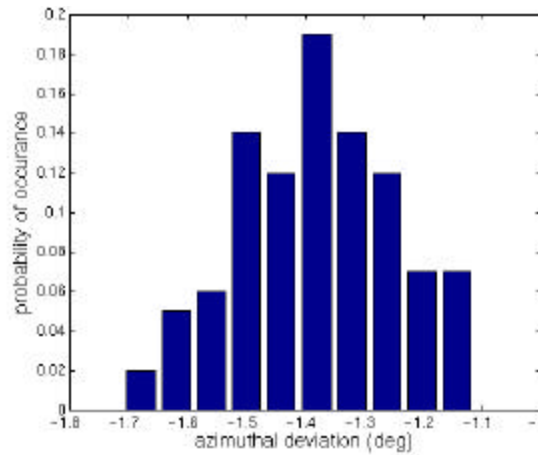

Figure 4. Example probability distribution of azimuthal deviation from Monte Carlo
analysis of thermospheric ray along 500-km path.

Network performance study

A network performance model is integrated into InfraMAP that includes the effects of environmentally driven propagation variability. For a selected network of sensors, source localization is computed from measured travel times and azimuths. Predicted uncertainty in ray azimuthal deviation and travel time is added to user-defined station measurement error, and confidence bounds for the localization are computed. These bounds are expressed as an area of uncertainty (AOU) for which there is a 90% probability that the actual source location is contained. For locations based upon travel time and azimuth, the AOU takes the shape of an ellipse. Network performance modeling is applied to data from the April 2001 Pacific bolide and compared to the satellite source localization. Figure 5 illustrates a sample localization and associated AOU ellipse.
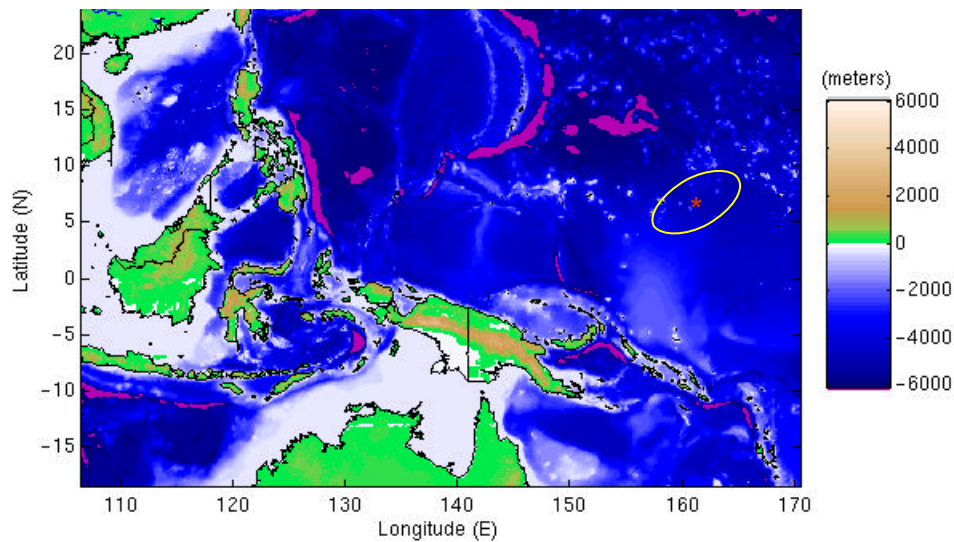
Figure 5. Sample network localization and AOU ellipse.

CONCLUSIONS AND RECOMMENDATIONS

Gravity waves are believed to be the dominant source of environmental variability that affects infrasonic propagation. A gravity wave spectral model has been integrated into InfraMAP based upon scale-independent diffusive filtering arguments. From the model, realizations of wind perturbation profiles are generated. The profiles are based upon five separate spectra in the vertical direction and one dominant Gaussian length scale in the horizontal direction.

Propagation variability is studied by propagating rays through the perturbed profiles, and Monte Carlo statistics are found for travel time and azimuthal deviation. These characterizations are applied to network performance, and AOU confidence bounds are calculated for source localizations.

Network performance studies need to be done over a variety of scenarios and environmental conditions. In areas of high station density, the localization AOU will be small, while in areas of sparse coverage they can become quite large. Defining these regions of best and worst localization accuracy is critical to evaluating the overall performance of an infrasound network.

REFERENCES

Gardner, C. (1995), Scale-Independent Diffusive Filtering Theory of Gravity Wave Spectra in the Atmosphere, The Upper Mesosphere and Lower Thermosphere: A Review of Experiment and Theory, Geophysical *Monograph* 87, AGU.

Gardner, C. (1993), Gravity Wave Models for the Horizontal Wave Number Spectra of Atmospheric Velocity and Density Fluctuations, *JGR*, 98, D1, 1035-1049.

ANALYSIS OF INFRASOUND SIGNALS FROM EKIBASTUZ MINING BLASTS AT KURCHATOV, KAZAKSTAN

Golam Sarker and Won-Young Kim

Lamont-Doherty Earth Observatory of Columbia University

ABSTRACT

Infrasound signals have been detected from large mining blasts in Kazakstan by the infrasound arrays at Kurchatov and Borovoye. For one month of data (March 1999) from the Kurchatov cross-array, we have recorded 163 events from the Ekibastuz mining region (Δ= 245 km, B-Az: 296°) in seismic channels, of which 63 (~43%) were detected in infrasound channels. For the same period of data, we have detected 122 events from the Kuzbass region (Δ= 740 km, B-Az: 58°) in seismic channels. Of these, 10 events have ground truth information. No corresponding infrasound detection is found. We also have detected four events in seismic channels at Kurchatov from a relatively less active mine in the Novotaubinka area (Δ= 197 km, B-Az: 123°). Infrasound signals from the Ekibastuz mining area at the Kurchatov array show two arrivals separated by about 60 s, though these arrivals can range between 40 and 90 s. The second arrival is observed in about 65% of the events (41 out of 63 infrasonically detected events). A simple ray tracing scheme through a suitable atmospheric model suggests that the first arrival that has a travel time of about 750 s propagates through the troposphere and is followed 60 s later by a stratospheric arrival. Best beams have been calculated for infrasound signals recorded at Kurchatov from the Ekibastuz and Novotaubinka regions. For Ekibastuz events, although the average best-beam azimuth from first arrivals varies within 3° to 7° from the seismically predicted azimuth, the phase velocity emerges slightly slower (about 280 m/s) than typical sound velocity of 330 m/s. The phase velocity for the second arrival, when present, is slightly higher, around 300 m/s.

For two months of data from Borovoye (December 1999 through January 2000), we have recorded 161 events from the Ekibastuz mining region (Δ= 381 km, B-Az: 113°) in seismic channels. The corresponding infrasound detection is very low (only 4). Infrasound detection is relatively high from nearby mines located NW of the array (Δ= 65 km, B-Az: 326°). From this period of data, we have recorded 36 events from the Kuzbass mining region (Δ= 1123 km, B-Az: 77°) in seismic channels. All of them have ground truth information. We were not able to detect positively any infrasound signals from the Kuzbass region at Borovoye. The infrasound signals that were recorded at Borovoye from the mines northwest and southeast of the array show one simple pulse with about 2- to 3-s duration. Best beams calculated from these infrasound signals show that predicted velocity is slightly slower than nominal sound speed, although predicted azimuth is similar to or slightly off from the seismically calculated azimuth. Best beam for signals from the Kuzbass region could not be resolved with confidence.

OBJECTIVE

The main objective of this project is to evaluate and characterize digital seismic and infrasound data from array sites in Kazakstan in order to improve event location and screening for nuclear explosion and Comprehensive Test-Ban-Treaty (CTBT) monitoring.

RESEARCH ACCOMPLISHED

Since spring of 1999, we have been acquiring infrasound signals from the Kurchatov and Borovoye arrays using available microphones. Several large mines in these areas routinely carry out large explosions that are detected seismically and with infrasound sensors. We have analyzed one month of data from the Kurchatov array and two months of data from the Borovoye array to better understand infrasound propagation in this region.

Station Deployment

We deployed infrasound arrays on the premises of Kurchatov and Borovoye Geophysical Observatories in Kazakstan (Figure 1). The Kurchatov Geophysical Observatory operates a 21-element short-period seismic borehole
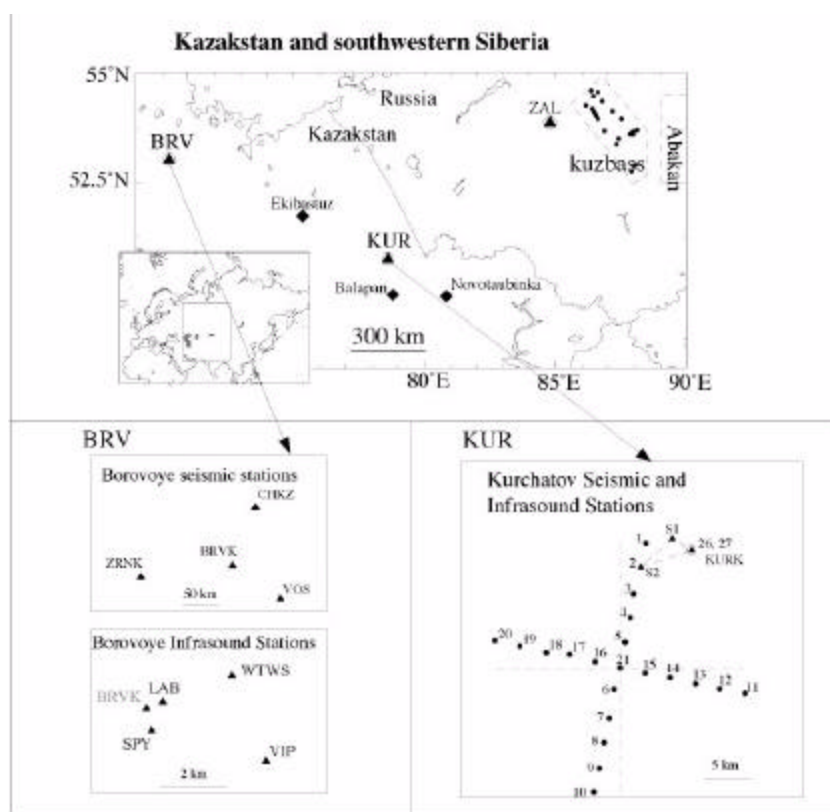

Figure 1. (top) map of Kazakstan and southwestern Siberia showing location of broadband seismic stations (solid triangle), active mining areas (diamond), Kuzbass and Abakan mining regions, and the Kurchatov (KUR) and Borovoye (BRV) Geophysical Observatories, where seismic and infrasound monitoring systems are deployed. (bottom) shows seismic and infrasound system configuration at both observatories (labelled). At KUR, 1 through 21 are short-period seismographic stations (spacing 2.25 km), KURK is a three-component broadband station, and S1, S2, 26, and 27 are infrasound stations.

array (cross-array) and a three-component broadband seismic station. A 4-component large aperture infrasound array (S1, S2, 26, and 27 in Figure 1) was constructed in the spring of 1999 at the Kurchatov Geophysical Observatory.

Each sensor is connected to six 70-m-long underground pipes extending radially from a central chamber that act to reduce wind noise. Sensor spacing varies between 2 and 4 km. Two types of capacitor microphones have been utilized with the pipe arrays configuration; Globe microphones at sites S1 and S2, and Soviet-built K301's at sites 26 and 27. The Globe microphone has a flat amplitude response between 0.1 and 300 Hz (ReVelle *et al*., 1997).

At the Borovoye Geophysical Observatory, we deployed a 4-element infrasound array (Figure 1). The spacing between infrasound stations is 2-3 km, and they are located within 2 km of central seismic station BRVK. The broadband seismic stations are recording signals in a continuous mode at 40 samples per second (sps), and have a flat response to velocity between 0.08 and 16 Hz. Globe microphones have been utilized to record infrasound signals. The microphones use a pipe array configuration to reduce local wind noise, similar to the Kurchatov infrasound system. The signals are recorded at 20 sps in a continuous mode. Infrasound signals in the frequency band of 0.8 - 3 Hz have been used for detection and array processing.

Seismic and Infrasound Observations at Kurchatov

Several large mines in Ekibastuz and surrounding areas generate explosions that are routinely detected seismically, and in many cases, are also detected with infrasound sensors. The Ekibastuz mine, 250 km northwest of the Kurchatov cross-array, regularly produces between four and six seismic detection per days. The location of these events are set to a central location of the Ekibastuz mine (51.61°N and 75.36°E) as determined by satellite photographs (Thurber et al., 1989), and their origin time is calculated from the IASPEI91 model.

For one month of data (March 1999) from the Kurchatov cross-array, we have detected 163 events in seismic channels from the Ekibastuz mine, of which 63 (~39%) were detected in infrasound channels. The infrasound signals of these events are visually examined for accurate picks and are bandpass filtered at 0.8-3 Hz for enhancing signal-to-noise ratio. For noisy data, signals are often Hilbert transformed to make them stand out from surrounding noise. The infrasound detection rate from this large aperture array is about four times larger than that detected from the small aperture array operated at Kurchatov between 1995-1997 (Hagerty *et al*., 2002).
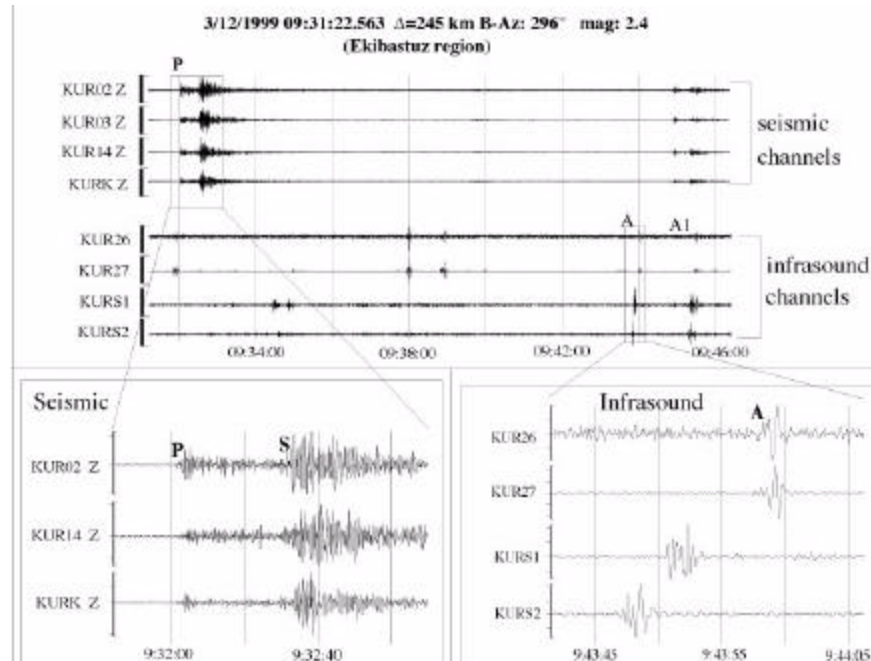

Figure 2. (top) showing a 15-min. time window of selected seismic and infrasound arrivals at the Kurchatov array. The event is located about 250 km NW of the network at the Ekibastuz mining area. Note two infrasound arrivals for this event (A and A1); the first arrival has a travel time of 756 s, and the second a travel time of 843 s. Simple ray tracing indicates this second arrival as wavetrains reflected back from the Stratospheric layer. (bottom) The figure displays close-up views of seismic and infrasound channels (labelled).

The infrasound wavetrain generated by Ekibastuz explosions exhibits two arrivals separated by about 60 s, though the separation time of arrivals can range between 40 and 90 s (Figure 2). The first arrivals show multiple pulses of 2- to 3-s duration, while the second arrivals show two pulses separated by 10 s. The travel time of the first arrival is about 750 s, corresponding to an apparent group velocity of 330 m/s. The second arrival is observed in about 65% of the events (41 out of 63 infrasonically detected events). The time difference between first and second arrivals exhibits great variation for Ekibastuz events, indicating that infrasound signals traverse through varying atmospheric conditions such as transient propagation ducts (Georges and Beasley, 1977).

For the same month of data, we also have detected four events in seismic channels from a relatively less active mine in the Novotaubinka region, of which, one was detected in infrasound channels (Figure 3). The region is 200 km
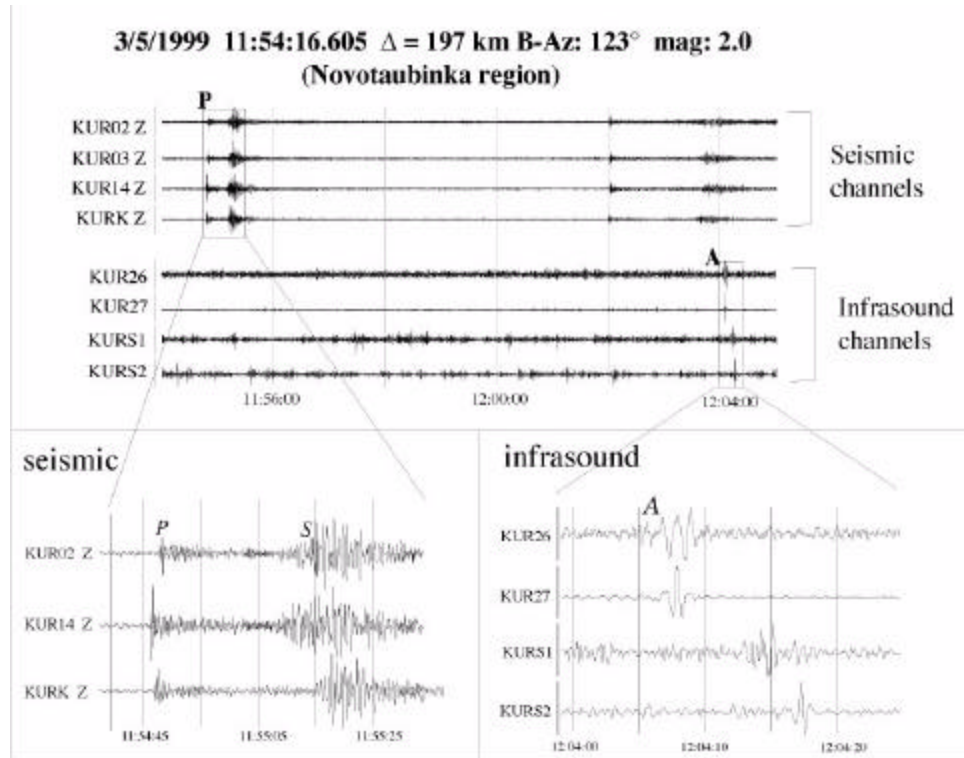

Figure 3. (top) Showing selected seismic and infrasound waveforms recorded at Kurchatov from an event at the Novotaubinka mining region (about 195 km SE of the network). P-wave travel time at KUR02 is 31.7 s, and infrasound (A) travel time at KUR26 is 629 s. This travel time corresponds to 330 m/s acoustic speed. No second infrasound arrival is detected at this distance and direction of propagation. (bottom) Close-up displays of selected seismic and infrasound channels (labelled) are shown.

southeast of the Kurchatov cross-array. The signals from the Novotaubinka region exhibit one single arrival at an apparent phase velocity of 330 m/s. For the same period of data, we have detected 122 events from the Kuzbass region in seismic channels at Kurchatov. The Altay-Sayan Experimental and Methodical Seismological Expedition (ASEMSE) collected ground truth information for 10 events from the Kuzbass and Abakan regions for this time period (Table 1). Signals from all those events are recorded in seismic channels at Kurchatov and the International Monitoring System (IMS) broadband station at Yeltsovka (ELT) (Figure 4). No corresponding infrasound detection is found. The Kuzbass mining area is about 700 km northeast of the Kurchatov cross-array, and about 120 km from the ELT station.

Best beams of infrasound arrivals calculated by slant stacking the traces for a given slowness grid show that the predicted azimuth is slightly off from the seismologically calculated azimuth (Figure 5). For a set of selected events

Table 1: Mining blasts in the Kuzbass and Abakan Regions with Ground Truth Data

| Date yr-mo-dd	Time hh:mm:ss	Lat (°N)	Lon (°E)	K	mb	Yield (ton)	name
99-03-03	08:21:38.9	53.85	88.10	9.2	3.59		Oldgerasky
99-03-05	10:45:22.60	53.60	91.37	9.3	3.64		Abakan-2
99-03-06	06:38:39.10	54.32	86.78	8.8	3.41	239.4	Karakansky
99-03-07	10:57:14.80	54.45	86.88	9.0	3.50		Kolmogovsky-2
99-03-10	09:48:52.00	53.71	87.86	9.4	3.68		Krasnogorsky
99-03-12	08:59:46.90	54.53	86.60	8.6	3.32		Kolmogorovsky-1
99-03-19	10:51:12.30	54.08	87.39	8.7	3.36	194.1	Badaevsky
99-03-24	09:11:57.70	53.71	87.83	9.3	3.64	209.4	Sibirginsky
99-03-30	06:55:31.80	53.85	88.15	8.9	3.45		Oldgerasky
99-03-31	09:03:11.60	54.54	86.62	8.9	3.45		Kolmogorovsky
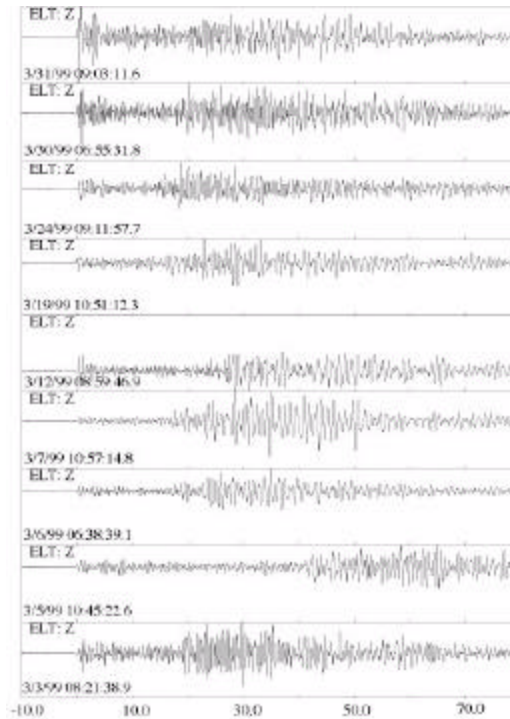
Figure 4. Waveforms of mining events listed in Table 1 recorded at ELT. Records are bandpass filtered at 1-5 Hz. Only vertical component data are shown. P-waves are aligned at 0.0. Origin times are shown in the box.

from one month of data from the Ekibastuz area, maximum power occurs when the traces for first infrasound arrivals are aligned with an average horizontal phase slowness of 3.76± 0.41 s/km (equivalent velocity of 266 m/s) and a back-azimuth of 303°± 5.5 (Figure 6). Although the average best-beam azimuth varies within 3° to 7° from the seismically predicted azimuth, the phase velocity emerges slightly slower than the nominal sound velocity of 330 m/s.

To ascertain whether the size of the mining blasts helps in detecting infrasound signals, we calculated the magnitude of the Ekibastuz events from seismic channels using a *Lg*-based regional magnitude formula (Nuttli, 1973). For Ekibastuz events, the magnitudes of all mining blasts detected range between 1.3 and 2.8, with a mean value of 2.0. The distribution resembles a Gaussian with a standard deviation of 0.30. The magnitude distribution of events that are only detected by infrasound channels also exhibits similar variations (mean 1.9 and standard deviation 0.26),
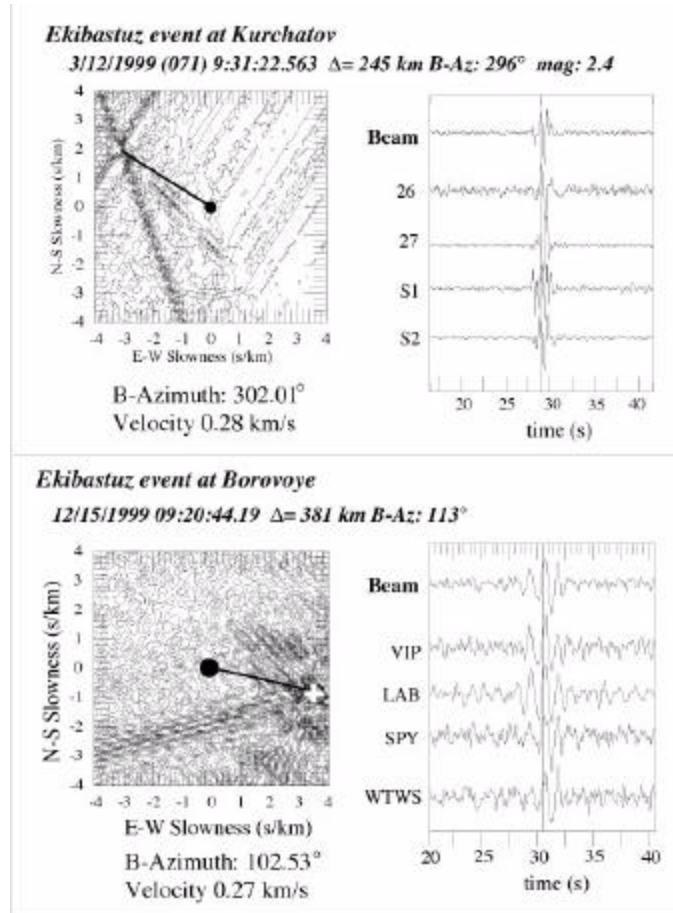

Figure 5. (top) Best beam (right) and contour plot of normalized maximum beam power (left) for an Ekibastuz event recorded at Kurchatov. The waveforms are that of Figure 2. Predicted azimuthal direction is about 7° off of seismologically calculated azimuth. (bottom) Same plot for another event from Ekibastuz recorded at Borovoye. The waveforms are that of Figure 6. In this case, the predicted azimuth is off by 5° from the seismological one. Solid circle is the location of the array, + is the predicted source, and thick solid line is the azimuthal direction. Times are relative to the beginning of the processed window length.

indicating that the magnitudes of seismic signals do not play a significant role in infrasound detection. Should magnitude contribute to infrasound detection, we would have seen a positively biased distribution of magnitude where the higher ends of distribution would only be coincident, not the lower ends.

Seismic and Infrasound Observations at Borovoye

For two months of data from the Borovoye seismic and infrasound array (December 1999 - January 2000), we have detected 161 coal mine events from the Ekibastuz area in seismic channels. The corresponding infrasound detection

is low -- only four. The Ekibastuz mining region is about 300 km southeast of the array. The infrasound wavetrains from Ekibastuz are simple, comprising a wave packet of 3-5 s long (Figure 7). The infrasound travel time is about 1150 s, which corresponds to an apparent group velocity of 300 m/s. For recordings at Borovoye, no second arrivals are seen in the infrasound channels for any events from Ekibastuz.

For the same months of data, we have positively identified six events from the Kokchetav mining region, located about 60 km northwest of the Borovoye array. The infrasound travel time is about 10.5 s, giving an apparent group
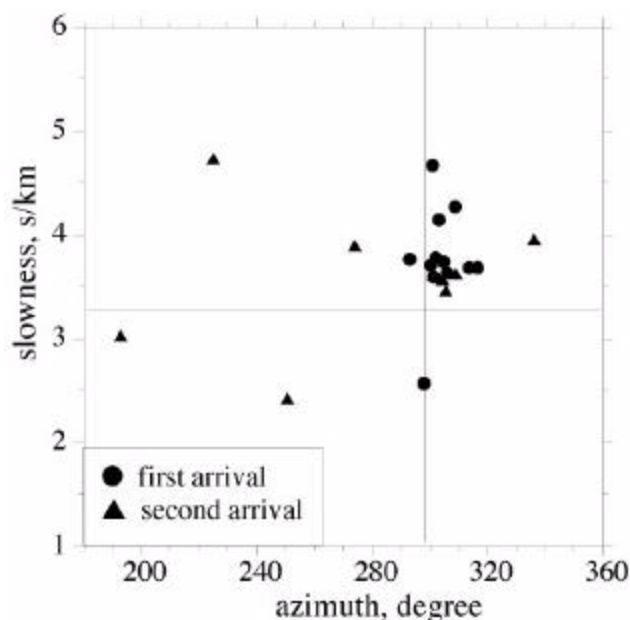

Figure 6. Plot showing predicted azimuth and slowness values from best beam analyses of infrasound arrivals from the Ekibastuz mining region. Circles depict measurements from first infrasound arrivals, and triangles from second arrivals, when present. The plot is made from 17 quality records where signal-to-noise ratio is greater than 3.The mean slowness of first arrivals is 3.76± 0.41 s/km (equivalent velocity 266 m/s) and azimuthal value is 303.2°± 5.5. The mean slowness and azimuth values for second arrivals are not determined because of large outliers in the data.

velocity of 310 m/s. Records from these events are seen in both seismic and infrasound channels. The infrasound waveforms comprise multiple pulses with about 2- to 3-s duration (Figure 8). ASEME collected the ground truth information for 49 events from the Kuzbass and Abakan regions for this time period. We have detected 36 events in seismic channels out of these 49 events. The Kuzbass mining region is about 1150 km east of the network. No corresponding infrasound signals have been positively identified.

Ground Truth Data From Large Mining Blasts in the Kuzbass and Abakan Regions

The Kuzbass and Abakan regions in southwestern Siberia conduct large mining operations. These mining regions are probably the largest that routinely conduct mining operations in Eurasia. The average size of the blasts is over 3 on the seismic magnitude scale. We obtained ground truth data for several mining blasts in the Kuzbass and Abakan regions for 1999-2000. ASEMSE located 367 blasts using data from regional seismic stations (Figure 9). The events located by ASEMSE have location errors ranging from about 5-10 km.

CONCLUSIONS AND RECOMMENDATIONS

Infrasound and seismic data recorded at the Kurchatov and Borovoye arrays from the Ekibastuz, Nobotuabinka, Kokchetav, Kuzbass, and Abakan mining regions have been analyzed. At Kurchatov, this data period covers March

of 1999, and at Borovoye, it covers December, 1999 - January, 2000. Results indicate high infrasound detection capability for large aperture arrays. The Ekibastuz mine produces 4-6 seismic detections per day, while there are 2-3 detections from the Kuzbass and Abakan mining region. For Ekibastuz events, about 65% of events that are detected by seismic channels are seen by infrasound channels at Kurchatov, while less than 1% of seismically
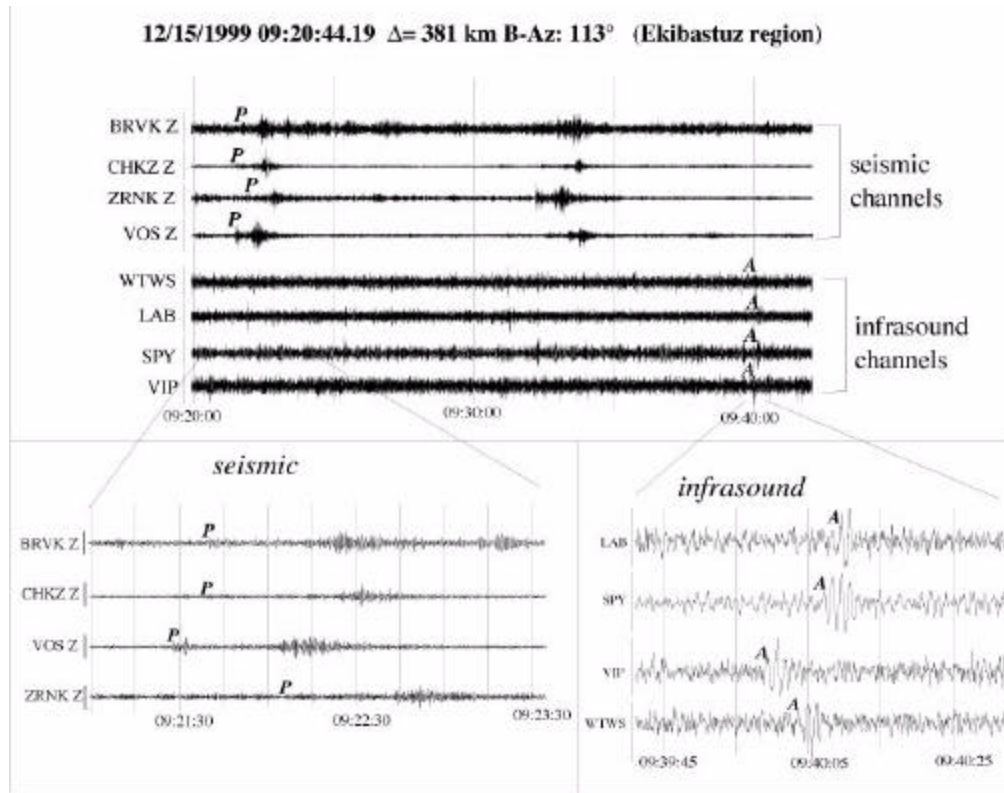

Figure 7. (top) showing selected seismic and infrasound recordings for an event from the Ekibastuz mining area recorded at Borovoye. The P-wave travel time at BRVK is 54.6 s, and the corresponding infrasound (A) travel time at LAB is 1163.8 s. This travel time corresponds to 300 m/s apparent acoustic speed. Bottom figure displays close-up views of selected seismic and infrasound arrivals (labelled).
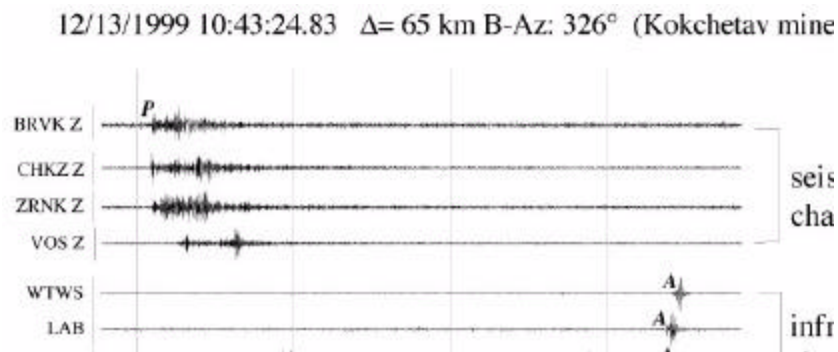

Figure 8. Plot showing selected seismic and infrasound waveforms recorded at Borovoye for an event from the Kokchetav mining region (65 km NW of the array). The P-wave travel time at BRVK is 10.7 s, and the corresponding infrasound (A) travel time at LAB is 208 s. This travel time gives an apparent acoustic velocity of 310 m/s.
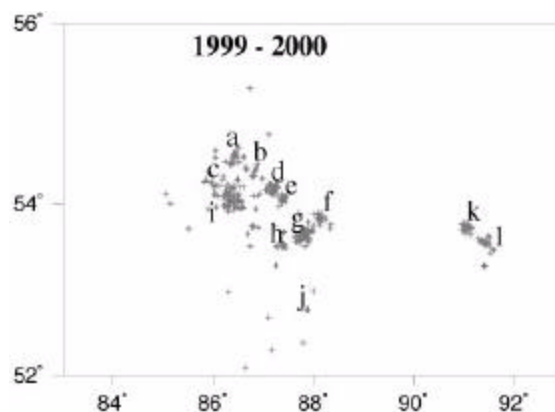
Figure 9. Mining events from the Kuzbass and Abakan regions during 1999-2000. Events were located by the ASEMSE group. Large mines are indicated by clusters of events. a: Kolmogorovsky-1, b: Kolmogorovsky-2, c: Kiselevsk, d: Taldinisky, e: Badaevsky, f: Oldgerasky, g: Mezhdurechensk, h: Kaltansky, i: Listvyansky, j: Tashtagol, k: Abakan-1, l: Abakan-2.

detected events from Ekibastuz are associated with infrasound channels at Borovoye. This may be related to wind direction and directivity of blasts. A simple ray tracing scheme using an appropriate atmospheric model for this region indicates that the first arrival propagates through the troposphere and is followed 60 s later by a stratospheric arrival. Such phenomenon of wave propagation is not seen in any channels that are located against the zonal wind direction. A second arrival appears in the infrasound sensor about 60s after the first arrival for Ekibastuz events that are recorded at Kurchatov. The second arrival, when present, also shows multiples pulses in the recordings, indicating strong positive sound speed gradients in the troposphere and, especially, in the upper stratosphere. Array analyses for data from the Ekibastuz, Novotaubinka, and Kokchetav regions show that predicted azimuthal direction is about 3°-7° off from the seismologically calculated azimuth.

<u>**REFERENCES**</u>

Donn, W.L. and E. Posmentier (1968), Infrasonic waves from natural and artificial sources. In *Acoustic-gravity Waves in the Atmosphere* (ed. T.M. Georges) (Boulder, CO.) 195-208.

Georges, T.M. and W.H. Beasley (1977), Infrasound refraction by upper-atmospheric winds, *J. Acoust. Soc. Am.*, **61**, 28-34.

Hagerty, M.T., W-Y Kim, P. Martysevich (2002) Infrasound Detection of Large Mining Blasts in Kazakstan, *Pure and Applied Geophysics*, **159**.

Kim, W-Y. and G.M. Sarker (2001), Infrasound Detection of Large Mining Blasts in Kazakstan, *Proceedings of the 23rd Seismic Research Review: Worldwide Monitoring of Nuclear Explosions*, October 2-5, 140-149.

Nuttli, O. (1973), Seismic wave attenuation and magnitude relations for eastern North America, *J. Geophys. Res.*, **78**, 876-885

ReVelle, D.O., R.W. Whitaker, and W.T. Armstrong (1997), Infrasonic observations of Bolides on October 4, 1996, Los Alamos National Laboratory Report: LA-UR-972481, 1-12.

Thurber, C., H. Given, and J. Berger (1989) Regional seismic event location with a sparse network: application to Eastern Kazakstan, USSR, *J. Geophys. Res.*, **94**, 17767 - 17780.

DETECTION AND LOCATION CAPABILITIES OF MULTIPLE INFRASOUND ARRAYS

Robert H Shumway

University of California, Davis

ABSTRACT

We have developed an integrated approach to locating an infrasound source that fuses local-array wave-number parameters and uncertainties into an overall location procedure. For local estimation of the velocity and azimuth, a small-array theory, based on maximum likelihood, has been given in earlier work that characterizes the large-sample uncertainty of the estimates and evaluates the theoretical missed-signal and false alarm probabilities. We have verified the theoretical uncertainties by computing empirical estimates using the frequency domain bootstrap on a gas-pipe explosion, a Titan IV B missile launch, and a Hawaii meteorite. Detection probabilities and wave-number uncertainties are then integrated into a Bayesian nonlinear regression procedure for evaluating the location capabilities of the particular global infrasound array that is proposed for the International Monitoring System (IMS).

We show contour maps for the average expected areas of the 90% confidence ellipses produced by the overall fusion procedure. The results indicate that for a single-array false alarm probability of 10^{-4}, the standard proposed IMS 4-element array will detect over 90% of the signals at signal-to-noise ratios as low as .6, with sufficient bandwidth. Location accuracies will require higher signal-to-noise ratios on the order of 2-4 and high single-array detection probabilities (>.90) to guarantee reasonable coverage (1000 km^2) for the 90% posterior probability ellipses. Eastern Hemisphere and Western Hemisphere 90% contour plots show almost complete coverage by expected uncertainty areas of 1000 km^2 or less.

OBJECTIVES

The objectives of this project have been to (1) develop the detection and estimation capabilities of small infrasound arrays and (2) to integrate these single-array directional estimation statistics into a procedure for assessing the predicted global performance of the infrasound component of the proposed International Monitoring System (IMS).

In support of (1), our sub-objectives were to develop local-array performance capabilities for estimating velocities and azimuths of propagation and to characterize single-array signal detection probabilities at low false alarm rates. In support of (2), our sub-objectives were to develop fusion posterior-probability ellipses for location and to incorporate single-array detection probabilities into a procedure for developing a global coverage map giving expected areas of 90% uncertainty regions.

RESEARCH ACCOMPLISHED

We have investigated a number of proposed procedures based on plane wave models for detecting infrasound signals at small arrays and for estimating velocities and azimuths, along with their predicted uncertainties. Velocities and azimuths are functionally related to the coordinates in the wave-number plot, say $\theta=(\theta_1,\theta_2)'$ and their predicted uncertainties. The estimated wave numbers and their covariance matrices for the detecting sub-arrays are fused into an overall location and its posterior probability ellipse. A large scale simulation using predicted detection probabilities and locations then is used to develop contour plots of the areas of the 90% error ellipses for the Eastern and Western Hemispheres.

Detection of Infrasound Signals

We have investigated three wave-number detectors from the literature, the Capon (1969) *high-resolution estimator*, the F-detector suggested by Shumway (1971), and the MUSIC estimator suggested by Schmidt (see Stoica, 1989).

The high-resolution estimator of Capon is the inverse of a Hermitian form in the probe vector, $\mathbf{x}(\theta)$, involving the inverse of the covariance matrix (see Shumway, 2001). Difficulties are in estimating the covariance matrix and in using the statistical distribution, which depends on the unknown theoretical covariance matrix. The multiple signal characteristic (MUSIC) estimator keeps the same form but replaces the inverse spectral matrix by the spectral matrix of the noise, approximated by an inner product of the residual eigen vectors (see Shumway, 2001). The difficulties with this detector relate to the intractability of its distribution under the *noise-alone* and the *signal-plus-noise* hypotheses.

The usual F-detector is defined as the ratio of the scaled beam power to the scaled error power, $F(\theta)$, where θ is the two-dimensional wave-number vector corresponding to a given velocity and azimuth (Shumway, 2001). In contrast to the high-resolution and MUSIC detectors, the performance is determined by observing that $F(\theta)$ is distributed as $(1+rN)F_{2L,2L(N-1)}$, i.e., as an F-statistic with 2L and 2L(N-1) degrees of freedom, where L=BT is half the bandwidth and N is the number of elements in the array. The parameter r is the signal to noise ratio on a single channel. Since the distribution under the noise-alone and signal-plus –noise hypotheses both involve the F, with r=0 under the noise-alone hypothesis, the preceding theory allows us to predict the detection probability as a function of any given false alarm probability. The result also allows unbiased estimation of the signal-to-noise ratio r by equating the value of the F-statistic to the expectation of $(1+rN)F_{2L,2L(N-1)}$.

Figure 1 shows the predicted detection probability for two hypothetical combinations of bandwidth (2L/n) and sub-array size, where L is the number of frequencies smoothed to obtain the test statistic and n is the total number of time points. Note that even with the smaller size array characteristic of those used in this paper, the signal detection is very high for relatively low signal-to-noise ratios and a false alarm probability of 10^{-4}. Extremely low false alarm probabilities are of interest in order to maintain an overall false alarm rate that is sufficiently low when there are many wave-numbers to test. For example, if 100 wave numbers are potentially of interest in this case, Bonferonni's inequality guarantees that the overall false alarm probability will be less than .01.

For illustration purposes, we show a contour plot in Figure 2 exhibiting the behavior of the three statistics given above and the beam power. Note that all statistics give comparable results for the Hawaiian bolide observed on April 23, 2001 from the Pinion Flat Array (shown in Table 1). This array was chosen because, with N=6 elements, it

represents a likely result from processing an event using an array that is close to the IMS configuration We simply note here that all processors detect the event and that F=172 is highly significant.   It should also be noted that the signal to noise ratio was extremely high here and the plots are unusually unambiguous. The apparently superior resolution of the Capon and MUSIC estimators does not lead to lower variances or to better resolution of multiple signals (Shumway, 2001) Comparable plots from the Los Alamos, Lac du Bonnet and Mina , Nevada showed multiple maxima that sometimes corresponded to velocities in the neighborhood of .3 km/sec and sometimes at unreasonable velocities. We note also that these arrays, for various reasons, only recorded on N=3 channels. To resolve some of these ambiguities, a general nonlinear optimization was employed that started in the neighborhood of a velocity and azimuth corresponding to the Hawaii location.

Estimation of Velocity and Azimuth Parameters

Figure 2 suggests that we simply read the wave-number coordinates corresponding to the maximizing value of the appropriate statistic and specify the velocity and azimuth corresponding to these wave-numbers as our estimated values. For the F-detector, the maximizers are equivalent to the maximum likelihood estimators, as was shown in Shumway *et al* (1998). Using the Cramer-Rao lower bound, they obtained variance-covariance matrices for the estimated wave-number parameters in Figure 2 and for the derived velocities and azimuths.

It was recognized early in the investigation that analytical computations for the variance-covariance matrices of the Capon and MUSIC estimators would be difficult and a version of the frequency domain bootstrap (see Shumway and Stoffer, 200, p244) was employed for these cases. This involves drawing a random sample from the frequencies determining the maximum likelihood estimator repeatedly and computing the mean and variance over a large number of bootstrap samples. This was not only done for the Capon and MUSIC estimators but was used to check the large-sample covariance matrices computed for the maximum likelihood estimators.

Table 1. Estimated azimuths and uncertainties (bootstrap std. dev.) for sample events.
LANL denotes value given by Los Alamos National Laboratories

Event	F	S/N	Capon	Music	LANL
Gas Pipe Explosion	256(1.3)	3.15	258(1.8)	257(1.3)	
Titan IV Missile	267(1.0)	.75	263(.4)	263(.4)	
4/23 Hawaiian Bolide					
Los Alamos	263(.3)	1.91	263(.4)	263(.4)	259
Lac du Bonnet	240(.1)	2.86	240(.2)	240(.1)	244
Pinion Flat	256(.8)	28.7	256(.8)	256(.8)	247
Hawaii	61(.6)	.83	59(1)	61(.6)	61
Mina, NV	237(.9)	3.79	238(1.3)	237(.9)	236
St. George, UT	278(2.3)	23.1	269(2.4)	276(2.3)	252

Preliminary results are shown in Table 1 for a 1998 gas pipe explosion and a Titan IV missile launch, both were recorded on four elements at the Los Alamos array. Additionally, we show results from a suite of arrays that recorded the April 23, 2001 Hawaii bolide. All events reside in the CMR R&D Test Bed Infrasound Waveform Library. As mentioned earlier, in order to handle severe aliasing that resulted in multiple maxima for the Los Alamos, Lac du Bonnet, and Mina arrays, non-linear optimization was used, starting in the vicinity of the assumed location. Because the asymptotic likelihood theory will not apply with multiple maxima, we used the frequency domain bootstrap to estimate the variances and covariances. The results for the bolide show estimated azimuths that are comparable with those obtained by Los Alamos National Laboratories with the exception of St. George Utah, where the angle should have been in the neighborhood of 246 degrees, LANL was close but we were off by 17-25 degrees

For the case where more than one array records a single event such as given by Table 1, one would be interested in the estimated location made by combining or fusing the results of the single-array wave-numbers and their covariance matrices into and overall location. The location theory is summarized in the next subsection.

Location Using Fused Array Wave-Number Parameters

Location results, given previously in Shumway (2000), require estimated wave-number coordinates $\theta_k(\mathbf{x})$ for $k=1,2,\ldots,n$ sub-arrays and their respective estimated covariance matrices, $\sum_k$, computed from one of the procedures in the previous section. The estimated wave-number coordinates are assumed to be a function of the location $\mathbf{x}=(x_1, x_2)$'. Linearizing $\theta_k(\mathbf{x})$ about an initial location $\mathbf{x}_0$, and performing the exact Bayesian analysis with a uniform diffuse prior on $\mathbf{x}$ and an inverted chi-square distribution for the location variance σ^2 in the location covariance matrix $\sigma^2 \sum$, we obtain the posterior probability distribution of the location vector $\mathbf{x}$ as a bivariate t-distribution. Then, using the fact that the posterior probability distribution of the quadratic form in $\mathbf{x}$ will have an F-distribution with 2 and 2(n-1)+m degrees of freedom, we obtain a posterior probability ellipse with a given posterior coverage area. Note that m degrees of freedom are associated with the chi-squared random variable defining the uncertainty in the scaling variance. The solution for independent errors ($\sum=\sigma^2 I$) was given by Jordan and Sverdrup (1981).

Global Array Performance of Proposed IMS Array

In order to develop a reasonable measure of global performance we considered incorporating the infrasound recording arrays proposed for the infrasound part of the IMS. For these plots, we used the asymptotic covariance matrix implied from maximum likelihood, as given by Shumway *et al* (1999) and in a previous SRS report (Shumway, 2000). For this simulation, we need the assumed signal-to-noise ratio (r=4) at a single station, the smoothing constant (L=51 frequencies), and the number of channels in a sub-array, assumed to be N=7, composed of 1km outer triangles with 1km sides and an inner inverted triangle with 2km sides. For location capability, we look at various simulated random configurations of detecting stations. For this initial simulation, we were lacking precise information on detection probabilities for single arrays although from Figure 1, we can infer that they will generally be high, with malfunctions excepted. Overall, we might optimistically expect an average of 9 out of 10 stations to detect and this was assumed for the simulation. We summarize the simulation procedure as:

1. Fix a hypothetical event location
2. Set input parameters as N=7 elements, signal to noise ratio r=4, and a bandwidth of .1 Hz.
3. Simulate a configuration of detecting stations (3<n<28, 3<n<32) for Western and Eastern Hemispheres respectively and P=.9, the probability for single sub-array detection. Assign the chi-squared distribution for the scaling variance as chi-squared with m=10 and expectation 1.
4. Compute the Bayesian posterior probability ellipse and area.
5. Repeat 3.and 4. 500 times, averaging the areas obtained.
6. Record average on grid and increment the hypothetical event location in 1. by 5 degrees.
7. Contour the results for the 90% posterior probability areas separately for the Eastern and Western Hemispheres.

Figure 3 shows the resulting contours in thousands of km^2 separately for the Western and Eastern Hemispheres. We note that doing the computation this way leaves out the possible detections between hemispheres and will distort the performance at the edges of both plots. We note that the 1000 km^2 contours include the majority of regions of interest (-80 degrees to 50 degrees for the Western Hemisphere and –80 degrees to 80 degrees for the Eastern Hemisphere). One could obtain a better index of performance for the western Pacific by folding in some of the Eastern Hemisphere sub-arrays and re-doing the computation. We tried relaxing the signal-to-noise ratio to r=2 or decreasing the detection probabilities to P=.5. Either strategy increases the 1000 km^2 to 3000 km^2.

CONCLUSIONS AND RECOMMENDATIONS

Theoretical computations have shown that the wave-number F-detector at a single array can be expected to perform very well for low signal-to-noise ratios and false alarm probabilities as low as 10^{-4}. We have not been able to collect enough historical detections from IMS stations to know that the empirical false alarm and signal detection probabilities will be equally impressive. Historical precedents set by seismic detections would imply that the empirical false alarm rates will be higher than the theoretical ones, implying that thresholds will need to be set high

to avoid significant numbers of false alarms. Every attempt should be made to develop empirical rates based on real events.

For the fused location estimators, theory suggests that we need higher signal-to-noise levels for the purposes of locating accurately with the seven element sub-arrays. The theoretical covariances for the conditions that guaranteed the good worldwide coverage for the 90% 1000 km^2 area contours were on the order of 10^{-4} km^2 whereas the bootstrap simulations using the Hawaiian bolide suggested that the covariance matrix would be on the order of 10^{-3} km^2. An indication of the overall scale variance that multiplies the covariance matrix can possibly be inferred by computing a location and a 90% posterior probability ellipse for the Hawaiian bolide. We intend to try this before the end of the contract.

<u>REFERENCES</u>

Capon, J. (1969). High-resolution frequency-wavenumber spectrum analysis. *Proc. IEEE*, **57**, 1408-1418.

Jordan, T.H. and K. A. Sverdrup (1981). Teleseismic location techniques and their application to earthquake clusters in the South-Central Pacific. *Bull. Seismolog. Soc. Amer.*, **71**, 1105-1130.

Shumway, R.H.(1971). On detecting a signal in N stationarily correlated noise series. *Technometrics*, **13**, 499-519.

Shumway, R.H. (2000). Detection and location capabilities of multiple infrasound arrays. *Proc. 22nd Seismic Research Symposium, 12-15 September*, New Orleans, Louisiana, Chapter 7, 7-12.

Shumway, R.H. (2001). Detection and location capabilities of multiple infrasound arrays. *Proc. 23rd Seismic Research Symposium, 2-5 October, Jackson Hole, Wyoming*, Chapter 7, 7-10.

Shumway, R.H., S.E. Kim and R.R. Blandford (1999). Nonlinear estimation for time series observed on arrays. Chapter 7, Ghosh ed. *Asymptotics, Nonparametrics and Time Series*, 227-258. New York: Marcel Dekker.

Shumway, R.H. and D.S. Stoffer (2000). *Time Series Analysis and Its Applications*. New York: Springer Verlag..

Stoica, P. and A Nehorai (1989). Music, maximum likelihood, and Cramer-Rao lower Bound. *IEEE Trans. Acoustics, Speech and Signal Processing*, **37**, 720-741.
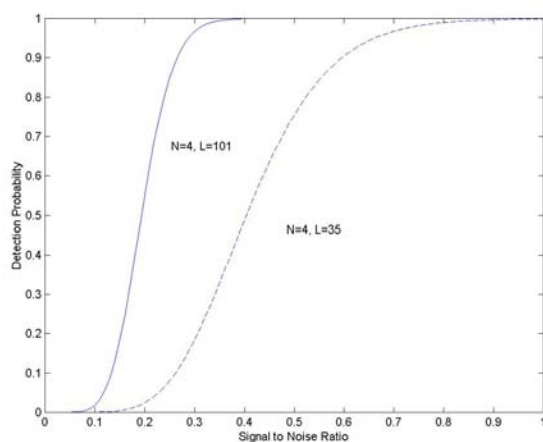
Figure 1. Detection probabilities for different signal-to-noise and smoothing options.
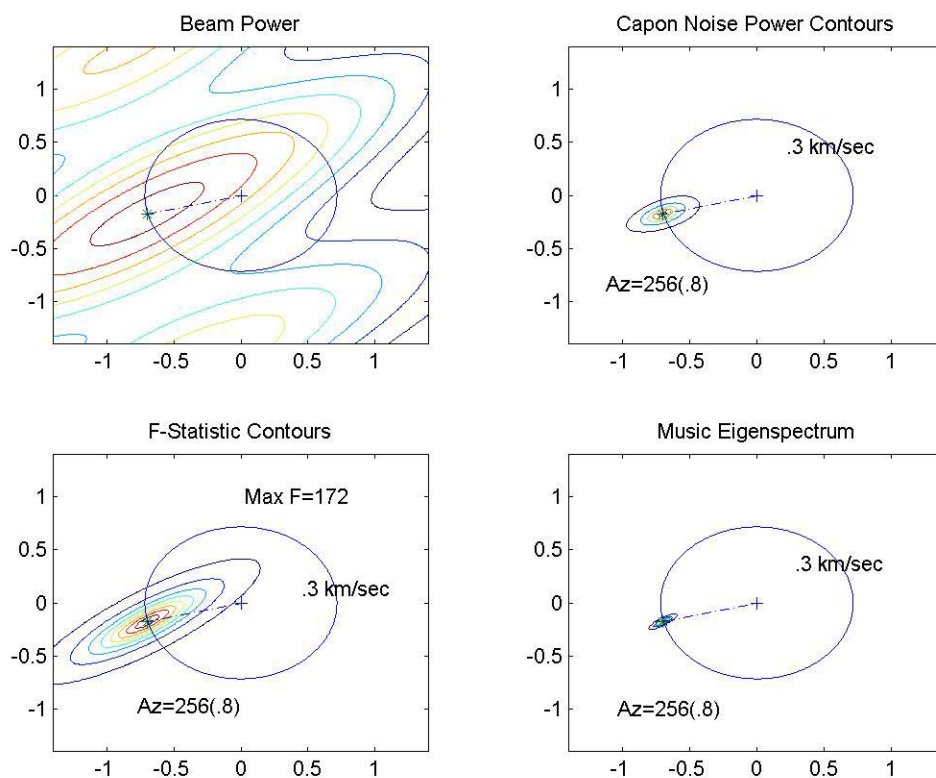

Figure 2. Wave-number analysis for the Hawaii bolide observed at Pinion Flat.
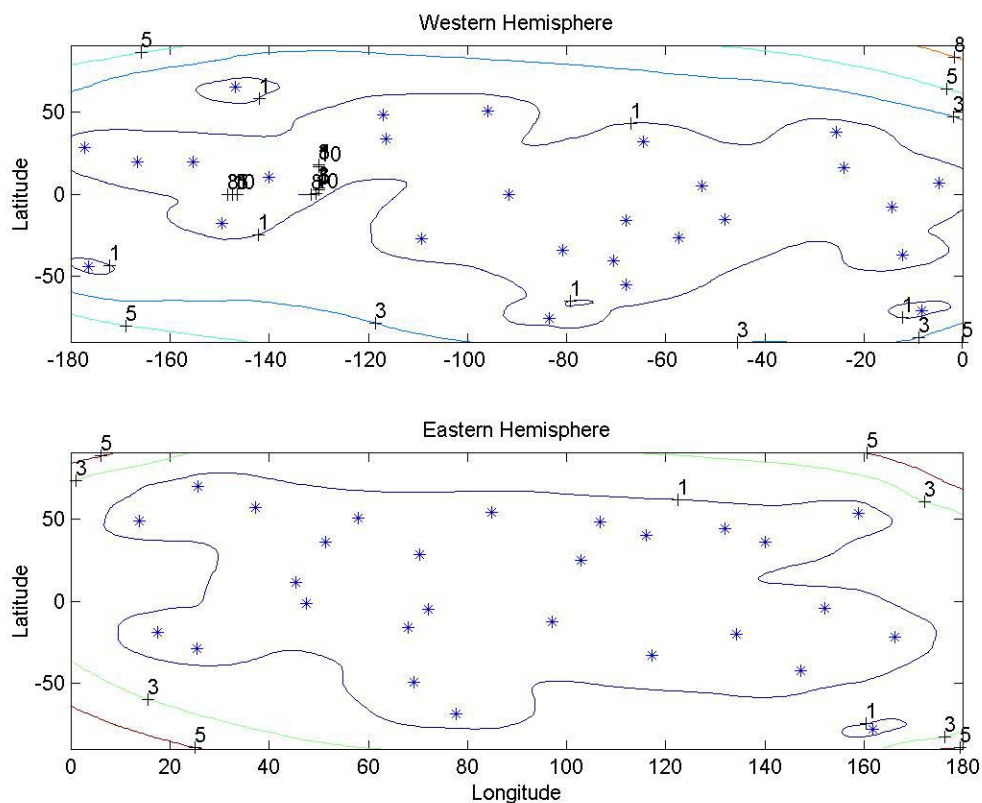
Figure 3. Contoured 90% posterior probability areas for a signal-to-noise ratio of 4 and a single array detection probability .9. Note that the 1000 square km contour includes most of both hemispheres. Array locations are shown as *.

ON INFRASOUND DETECTION AND LOCATION STRATEGIES

Rodney Whitaker, Douglas ReVelle, and Tom Sandoval

Los Alamos National Laboratory

ABSTRACT

Routine processing of infrasound array data has been ongoing at relatively few locations during the recent past, and at these locations there has been little to no processing of data from large infrasound networks. As more infrasound monitoring stations become operational, data from them will take on more importance, especially with regard to automated processing routines. We discuss various ideas on detection and location strategies based on our operational experience and input from infrasound researchers. This presentation is directed toward stimulating the discussion about the best approaches to the infrasound data-processing task. This discussion applies to the monitoring task, and it should be noted that this is not the same as the research task. A good research program improves the monitoring function.

Aspects of existing automated processing, other approaches that can aid in the identification of interesting events, and simple criteria that can screen out uninteresting events are considered. The value of wide band processing for sparse arrays is discussed. Implementation of standard location techniques for infrasound monitoring is considered using simple travel-time data. Guidelines for comparison of different approaches are discussed and illustrated with data from bolides and earthquakes.

OBJECTIVE

The last US infrasound network was almost entirely closed out by about 1974 after 20 years of service detecting atmospheric nuclear explosions. In the mid 1970s, digital signal processing was just beginning to be used in a variety of disciplines, and infrasound benefitted only a little from this new processing. Routine processing of infrasound data, prior to 1998, was or had been done at only a few locations, including: Los Alamos National Laboratory (LANL); the National Oceanographic and Atmospheric Administration in Boulder CO; University of Alaska, Fairbanks AK; and Columbia University NY. Our objective here is to stimulate thought and discussion about signal processing applicable for analysis of the developing infrasound network of the International Monitoring System. The presentation will draw on our experience and will be an overview rather than an exhaustive analysis.

RESEARCH ACCOMPLISHED

As a waveform technology, infrasound can benefit from some of the existing processing infrastructure developed during the long monitoring period of seismic research. After all, there is similarity in frequency content and sampling rates; many concepts apply straightaway. But there are differences as well. In traditional infrasound work, little use is made of power detectors because, in part, the wind backgrounds can be quite variable. Rather, because the signals from distant sources are usually well correlated, cross-correlation detectors are far more common in infrasound and acoustic processing. LANL found that the algorithm developed by Young and Hoyle (1975) to be highly valuable in their work from 1983 to the present. Of course one might work with an F detector, rather than cross-correlation, where, for ideal conditions, the F statistic is related to the correlation coefficient, C, as, $F = n C /(1-C) + 1$, where n is the number of sensors. Normalized cross-correlation is bounded, 0 to 1, while the F statistic is unbounded.

The processor discussed by Young and Hoyle (1975) has some differences from traditional FK processing, and they describe their approach as frequency slowness $S(\omega)$. One point they present is that for wide-band non-dispersive signals, the $S(\omega)$ processor mitigates against side lobe alignment in different frequency planes and reduces their importance. Ferguson (1999) and Katz (2001) also discuss this point from a different perspective but show the value of wide-band processing in many cases. Below we show traditional FK results for some data from the four-element LANL array at the Nevada Test Site for a correlated signal. The strongest values are deep red with the peak at (x=8, y=23). Other strong cells are apparent over the 40 x 40 FK plane.
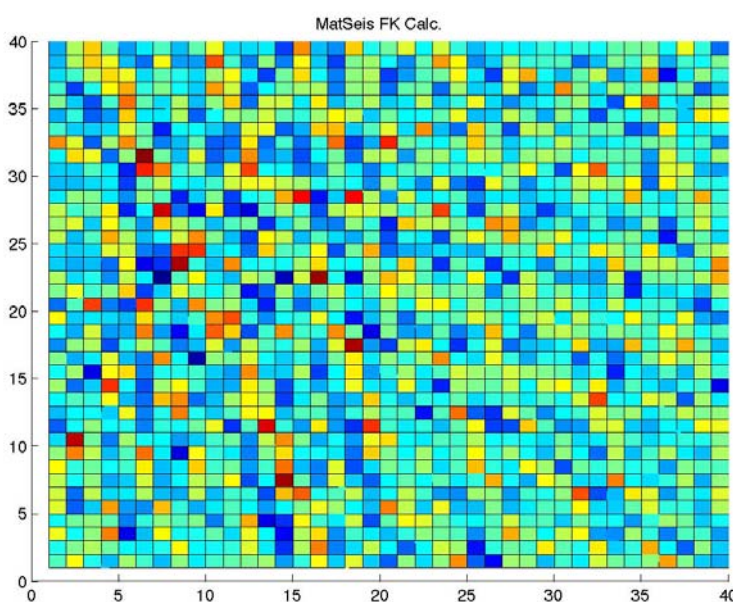

Figure 1. Traditional FK results for some data from the four-element LANL array at the Nevada Test Site for a correlated signal

Figure 2 gives the equivalent result for the same data segment computed with the S(ω) correlation processor. Here the peak is well defined at (8,24) and is clearly the peak value with no competition from other cells. The same window size and passband were used in both cases, and the processing was done with MatSeis.
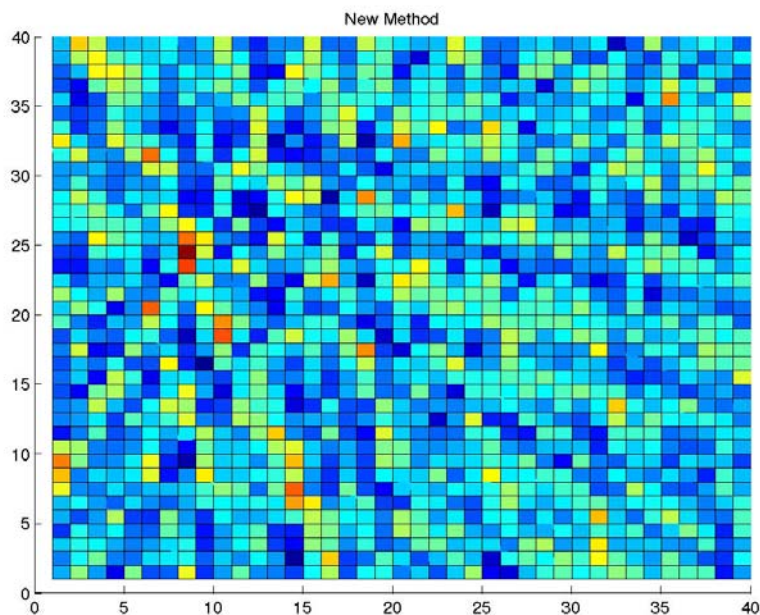

Figure 2. Equivalent result (to that in Fig. 1) for the same data segment computed with the S(ω) correlation processor.

The FK results use the FK tool in MatSeis, and the correlation slowness processing was done with Infra_tool. The results above for $S(\omega)$ processing with four elements indicate that the alias problem, with four elements, may not be as serious as first thought. However, there are still good reasons that added elements are needed for improved performance. Added elements provide better array gain as well as redundancy against sensor loss. They will enable better broadband response. In recent work we found another example of how added elements can aid the detection capability.

We recently processed data from DLIAR and LSAR for the shuttle launch of 5 June 2002, expected at around 23:50 UT. LSAR is a smaller baseline array sitting inside the prototype DLIAR array. Spring and summer shuttle launches have been detected by DLIAR, but in this case, as displayed in the figure to the right, DLIAR got very weak correlation, albeit with localization of azimuth and trace velocities. The data were processed with MatSeis and Infra_Tool, and the figure is part of the Infra_Tool Graphical User Interface (GUI) display. From the top, the panels display correlation, trace velocity, azimuth and one channel of data. Twenty-second windows were used with a band pass of 1.0 to 4.0 Hz. The LSAR results show much better correlation, azimuth and trace velocity trends, as is obvious in the next panel. This is an extreme case of the loss of correlation over the larger baseline of the DLIAR (~1.2 km) array as compared to the small baseline (~0.2 km) of the LSAR array. In looking at numerous cases of the same signal on both arrays, we often find a loss of 0.15 to 0.20 units in normalized cross-correlation values due to larger
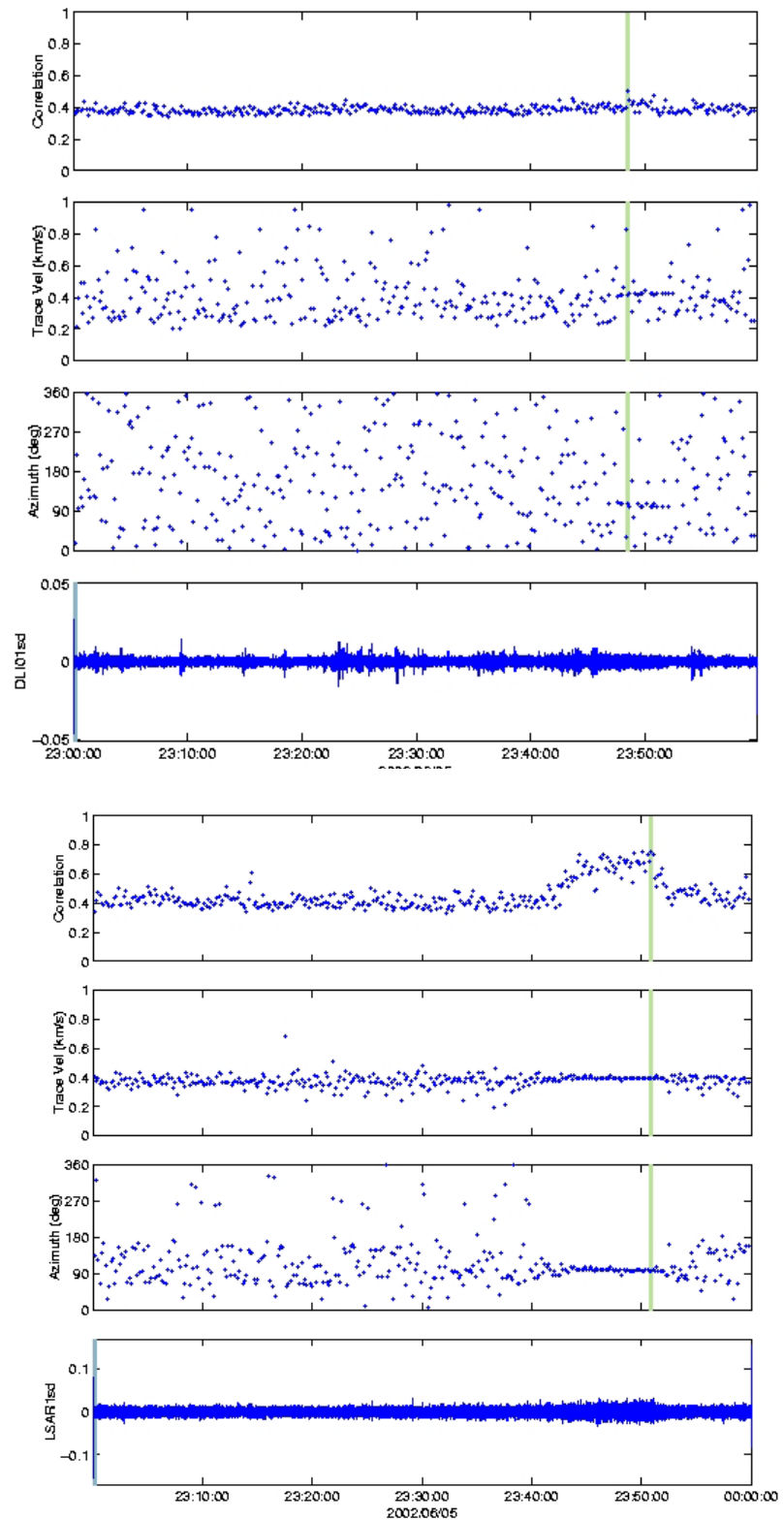

Figure 3. Data from DLIAR (top) and LSAR (bottom) for the shuttle launch of 5 June 2002

833

baseline. Another example of the correlation loss is given by the DLIAR and LSAR results for a California earthquake on 22 February 2002. Both arrays had good results with the azimuth for DLIAR coming out at 245.9 degrees and that for LSAR at 244.5 degrees. The peak cross-correlation for DLIAR was 0.718 and that for LSAR was 0.944. We are beginning to look again at common DLIAR and LSAR signals now that LSAR has been restored after the Cerro Grande fire.

One could envision a detector based upon the type of processing used in Infra_Tool wherein one would look for constant azimuth signals having some correlation above a threshold and duration longer than some minimum. These results could then be passed onto a global association scheme combining other infrasound stations as well as seismic and hydroacoustic stations.

One of the biggest differences between seismic and infrasound analysis occurs because the atmosphere is dynamic on a variety of time scales, and the solid earth is relatively static. Thus concepts such as travel times with really small variations, on teleseismic distances, are not possible in the atmospheric domain. Location uncertainty in atmospheric acoustics will be larger than in seismic because the travel times will have larger variation, due to the influence of winds. Nevertheless, some average properties of propagation are quite reliable. In the older monitoring period, the main acoustic arrival was associated with energy that arrived with an average travel velocity of 0.290 km/s $\pm$ 0.015 km/s for favorable propagation conditions. In a ray-acoustic picture, this condition represented energy refracted from altitudes of around 50 km and was referred to as a stratospheric return. Higher altitude refractions would, often, show lower average travel velocities of approximatey 0.25 km/s. With atmospheric travel-time variations, locations using only timing would have rather large areas of uncertainty. But because infrasound signals are well correlated, quite good bearings, back azimuths, can be derived, and for two stations, intersecting back azimuths give an estimate of location and distance. With these in hand, one can begin to identify parts of the waveform associated with specific atmospheric phases. Then, among two or more stations, one could examine the results for consistency. Ray-mode theory can aid in location by confirming, if some atmospheric data are available from models or observations, and by showing if signals from the intersection of two or more bearings really can get signals to the stations.

Another difference between infrasound and seismic monitoring is that infrasound uses timings from peak correlation whereas seismic uses first arrival (or onset) time for location. Some infrasound signals emerge slowly out of the background, making onset difficult to determine. Peak correlation can easily be found and the timing can be taken as the time of the middle of the processing window in which correlation peaks. At LANL we have determined this to be an effective approach.

The roles of research and monitoring need to be kept in mind and their differences understood. Analysis for research purposes will be different from that for monitoring. For example, very short impulsive signals are of research interest but can probably be ignored in monitoring as being due to small local events. Events with varying azimuth may be of research value but are not signals from point explosions and thus of little monitoring interest. Over time, results from the research arena will improve the monitoring capability making it more effective. Indeed, it will be the targets of opportunity, cultural and natural, that will provide the events around which the processing can be tested and improved. Both aspects need to be pursued to ensure that the processing is of the highest quality and that signals of interest are not missed.

In comparing results from different tools, one must be careful to be sure that processing parameters are, to the extent possible, the same, or as similar as they can be. A difference in azimuth of five or six degrees may or may not be a real difference. As the processing of infrasound data in the network matures, various schemes will be compared and discussed. We need to be careful to make the comparisons as meaningful as possible.

CONCLUSION

This short contribution has discussed some aspects of infrasound processing based largely on the operational experience at LANL. It has been our desire to stimulate thought and discussion

REFERENCES

Ferguson, Brian G., 1999, Time-delay estimation techniques applied to the acoustic detection of jet arrival transits, JASA**, 106,** 255.

Ham, Fredric M., 2001, Neural Network Classification of Infrasound Events Using Multiple Array Data, Infrasound Technology Workshop, Kona, HI.

Katz, Charles N., 2001, private communication.

Young, Jessie M., and Wayne A. Hoyle, 1975, Computer Programs for Multidimensional Spectra Array Processing, NOAA Technical Report ERL 345-WPL 43.